

INTEGRATED DESIGN OF ROTOR ASSEMBLY
FOR RADIAL FLUX SMPMSM

AN INTEGRATED DESIGN APPROACH OF ROTOR ASSEMBLY
FOR RADIAL FLUX SURFACE-MOUNTED PERMANENT
MAGNET SYNCHRONOUS MOTORS

By AKSHAY MANIKANDAN,

A Thesis Submitted to the School of Graduate Studies in Partial
Fulfillment of the Requirements for
the Degree Master of Applied Science

McMaster University © Copyright by Akshay Manikandan, August

2023

McMaster University

MASTER OF APPLIED SCIENCE (2023)

Hamilton, Ontario, Canada (Mechanical Engineering)

TITLE: An Integrated Design Approach of Rotor Assembly for
Radial Flux Surface-Mounted Permanent Magnet Syn-
chronous Motors

AUTHOR: Akshay Manikandan
B.tech (Automobile Engineering),
Hindustan University, Tamil Nadu, India

SUPERVISOR: Ali Emadi, Professor
Ph.D. (Texas A&M University)
IEEE Fellow
Canada Excellence Research Chair Laureate

NUMBER OF PAGES: xvi, 145

Lay Abstract

This thesis aims to increase the reliability and power density of a surface-mounted permanent magnet synchronous machine (SPMSMs), a commonly used traction motor in the automotive and aerospace industries. One of these machines' main challenges is designing their components to withstand the high mechanical loads caused by their fast rotational speeds. The studies performed in this thesis use a computer modeling technique called Finite Element Modeling (FEM) to strategize and design an integrated rotor hub/shaft by maximizing the durability of a 150kW radial flux SPMSMs rotating at 20,000 rpm. Upon evaluating the integrated design using a variety of physics-based simulations, the design was found to save 1.84kg in weight, reducing centrifugal forces and improving the overall stiffness of the motor assembly. This research could lead to more efficient and durable electric SPMSMs for various applications.

Abstract

Enhancing the dependability and power density of a SPMSMs is crucial for its extensive utilization in the automotive and aerospace sectors. One major concern regarding these machines is the significant thermo-mechanical loads experienced by the overall rotating assembly due to high rotational speeds and a wide operational temperature range from $50^{\circ}C$ to $150^{\circ}C$. This poses a considerable challenge in maintaining structural integrity among the components. Redesigning components to reduce assembly complexity and weight necessitates careful consideration of boundary conditions and contact modeling to prevent catastrophic failures like magnet fly-by conditions. To reduce model complexity, a simplified approach involves integrating the hub and shaft; both machined from AISI 4340. Additionally, the application of a carbon fiber sleeve is investigated through 3-dimensional composite modeling to enhance structural integrity. The primary objective of this thesis is to scientifically justify the design and validation of an integrated rotor hub and shaft using efficient FEM and integration strategies, with the aim of maximizing the durability of a $150kW$ radial flux SPMSMs spinning at $20,000rpm$. The integrated topology optimization is evaluated using a multiphysics platform alongside studies on motor assembly eigenfrequency. By employing the integrated approach and utilizing AISI 4340 for both the shaft and rotor

hub, a weight reduction of $1.84kg$ is achieved, eliminating the need for standard components such as balancing end clamp plates, locknuts, and washers. Furthermore, introducing a carbon fiber sleeve enhances structural integrity, thereby reducing adhesive stress. The design and optimization of the rotating components ensure that the maximum von Mises stress is 50% lower than the material's yield strength. Reduced masses lead to lower centrifugal forces, thereby diminishing radial stress and promoting component and assembly stiffness.

*Dedicated to my beloved family
friends and colleagues*

Acknowledgements

I express my gratitude to Dr. Ali Emadi, my supervisor, for giving me the opportunity to be a part of the exceptional team of world-class researchers at MARC. His unwavering support and encouragement have been highly valuable throughout my graduate studies.

I extend my heartfelt appreciation to Mikhail Goykhman and Sathyan Anand from Eaton for their constant encouragement, valuable advice, and the permissions they granted for my research, publications, and this thesis. Their exceptional leadership has been a great source of inspiration, and I feel privileged to have had the opportunity to collaborate with them during my time at McMaster.

I want to express my sincere gratitude to the members of the Aero RTA3 group, namely Mohamed Abdelmagid, Pietrini Georio, Kenneth Noronha, Islam Zaher, Maaz Khalid, Srikanth Vasudevan Pillai, Alexander Forsyth, and Dikhsita Choudhary, with whom I had the privilege of working closely on a daily basis. Additionally, I am thankful to all my peers and colleagues from Dr. Emadi's research group at MARC. Special thanks go to Dorathy Babu, Aathira Karuvaril Vijayan, Rachit Pradhan, Shreyas Shah, and Sreejith Chakalakkal for their love, friendship, and unwavering support during my graduate studies at MARC. It was truly an honor to be part of such an incredible group of individuals.

List of Publications

Conference Papers:

- **Manikandan, A.**, Abdalmagid, M., Pietrini, G., Goykhman, M. et al., "Rotor Durability Optimization by Means of Finite Element Multiphysics Analysis for High-Speed Surface Permanent Magnet Electric Machines," SAE Technical Paper 2023-01-0529, 2023, <https://doi.org/10.4271/2023-01-0529>.
- **A. Manikandan**, M. Abdalmagid, G. Pietrini, M. Goykhman and A. Emadi, "Structural Design Evaluation of Integrated Rotor Hub and Shaft for a High-Speed Surface Mounted Radial Flux Permanent Magnet Synchronous Motor," 2023 IEEE Transportation Electrification Conference & Expo (ITEC), Detroit, MI, USA, 2023, pp. 1-6, doi: 10.1109/ITEC55900.2023.10186954.I.
- Zaher, **A. Manikandan**, M. Abdalmagid, G. Pietrini, M. Goykhman and A. Emadi, "Multiphysics Thermo-Structural Design of the Rotor in High-Speed Permanent Magnet Machines for Aerospace Propulsion Applications," 2023 IEEE Transportation Electrification Conference & Expo (ITEC), Detroit, MI, USA, 2023, pp. 1-6, doi: 10.1109/ITEC55900.2023.10187099.

Table of Contents

Lay Abstract	iii
Abstract	iv
Acknowledgements	vii
List of Publications	viii
List of Abbreviations	xvi
1 Introduction	1
1.1 Background	6
1.2 Motivation	8
1.3 Thesis Contribution	9
1.4 Thesis Outline	11
2 SPMSMs for More Electric Aircraft	15
3 Electromagnetic Construction of a Radial-Flux SPMSMs	19
3.1 Electromagnetic Assembly of the Stator	20
3.1.1 Stator Copper Windings	21

3.1.2	Stator Core	24
3.1.3	Encapsulation and Stator Casing	27
3.2	Electromagnetic Assembly of the Rotor	28
3.2.1	Permanent Magnets	29
3.2.2	Rotor Core	31
4	Contemporary Design of Rotor Assembly of Radial Flux SPMSMs	33
4.1	Design of Shaft and Rotor Hub	34
4.2	Design of Permanent Magnet	39
4.3	Design of Axial and Radial Rotor Assembly Retention Systems	41
4.4	Issues with Contemporary Design of Rotor Assembly	44
5	Impact of AISI4340 vs Non-oriented Electrical Steel	48
6	Design Considerations for Integrated Design	52
7	Simulation Framework for Static and Dynamic Analysis	60
8	Static Performance of Integrated Shaft-Hub Design	68
8.1	Finite Element Pre-Processing	69
8.1.1	Stress-Strain Curve Extraction	71
8.1.2	Finite Element Modelling	73
8.1.3	Finite Element Integration	77
8.1.4	Constrained Boundary and Optimal Loading Conditions	81
8.2	Finite Element Post-Processing	87
8.2.1	Displacement Pattern	88
8.2.2	Thermal Stress Risers	91

8.2.3	Optimization of Integrated Design	99
8.3	Analytical Fatigue Estimation of AISI 4340	101
9	Dynamic Performance of Integrated Shaft-Hub Design	106
9.1	Eigen Frequency Analysis of Integrated Design	107
9.2	Analytical Critical Speed Estimation	113
10	Manufacturing Processes Involved in Integrated Design	117
11	Ideal Configuration of Strain Gauges – Test Setup	123
12	Conclusions and Future Work	130
12.1	Thesis Summary	130
12.2	Future Work	134

List of Figures

1.1	Electric machines in eVTOL market	3
1.2	(a) Axial-flux SPMSMs (b) Radial-flux SPMSMs	6
1.3	Mechanical design cycle	10
2.1	Advanced motor drive - EMA (left); Electric brake - Boeing aircraft (right) using PMSMs [1]	16
2.2	GT traction hub motor designed for aircraft taxiing [2]	17
3.1	Simplified cross-sectional view of the stator assembly of a Radial-flux SPMSMs [3]	20
3.2	Overlapped winding - (a) distributed, (b) concentrated; Non-overlapped winding - (c) all teeth wound (d) alternate teeth wound [4]	22
3.3	(a) Encapsulation of stator core and windings [5] (b) Stator casing design [6]	27
3.4	Rotor assembly mainly showcasing the electromagnetic components .	29
4.1	SContemporary FE design of a Radial-flux SPMSMs[7]	34
4.2	One-piece shaft design	37
4.3	Different types of optimized laminated hub design	38
4.4	(a) Location of balancing end plates in motor assembly (b) Side and (c) Isometric view of end plates with dimensions	42

5.1	Magnetic field strength of Normal PM's (left) and Halbach-array PM's (right) [8]	49
5.2	A 1/3 electromagnetic model of the rotor with 4-segment Halbach array /pole configuration	50
6.1	An FE representation of the integrated design	53
6.2	Layout of integrated design	59
7.1	Framework for CAD design	61
7.2	Framework for FEA design - Static analysis	63
7.3	Framework for FEA design - Dynamic analysis	65
7.4	Framework for FEA slot optimization	66
8.1	True stress-strain curve for AISI 4340 using modified power-law hardening	72
8.2	A Varying mesh density based on feature and component of study . .	74
8.3	(a) Abrupt von-mises stress concentration due to insufficient capture of feature (b) Two rows of washer layers to enhance stress distribution along load/boundary path	75
8.4	N2S and S2S discretization with CGAP elements (purple) [9]	77
8.5	RBE2 and RBE3 coupling in Optistruct/Nastran/Abaqus [9]	78
8.6	Contact definition and adhesive modeling	80
8.7	(a) Sectional side view of boundary components for integrated design analysis (b) Location of constraints applied on Dyno adapter plate . .	82
8.8	Corrected 3D bolt modelling for preload application	84
8.9	A subcase process flow setup for multiphysics simulation	86

8.10	Clipped axial displacement of integrated design in both no-load and full-load condition	90
8.11	Sectional view of maximum stress in bearing base region of the integrated design	93
8.12	Sectional view of maximum strain and strain tensor in bearing base region of the integrated design	94
8.13	Sectional view of maximum strain and strain tensor in bearing base region of the integrated design	95
8.14	Strain tensor in major principal (normal) axis of a single PM	97
8.15	Max hoop stress on Carbon fiber sleeve	98
8.16	4 of the best chosen parametric optimization of slots for the integrated design	99
8.17	Wohler curve denoting HCF and LCF with ascending loads [10]	102
8.18	Possible location of HCF in integrated design on bearing base	103
9.1	Comparison of eigen frequencies of constrained and unconstrained analysis setup of integrated design	110
9.2	Critical eigen frequencies and their mode shapes	112
9.3	Free body diagram of the integrated design	114
10.1	Various machining processes involved in the integrated design	120
11.1	(a)uniaxial strain (meets criteria) (b) triaxial strain gauge setup	126
11.2	Induction based telemetric setup [11]	128
12.1	Conventional vs integrated design approach	131
12.2	Max von mises stress from FEA vs yield strength of materia	132
12.3	Frequency array of all dominant frequencies in the system	133

List of Tables

4.1	Comparison of electrical and mechanical properties of NdFeB and SmCo permanent magnets [12]	40
5.1	The machine's electromagnetic performance with the different rotor hub material	50
6.1	Machining processes involved in the contemporary vs integrated design	56
6.2	Mass savings between contemporary and integrated design	58
8.1	Suitable mesh size and element type - Mesh sensitivity	75
8.2	Axial and radial displacement pattern of integrated design and PMs .	89
8.3	Summary of thermal stress in the integrated design	92
8.4	Summary of thermal stress in the optimized integrated designs	100
9.1	Critical eigen frequencies for the first 10 modes for the integrated design assembly	111

List of Abbreviations

2D	2-Dimensional
3D	3-Dimensional
EMF	Electromotive Force
RPM	Rotations Per Minute
CFD	Computational Fluid Dynamics
CTE	Coefficient of Thermal Expansion
SPC	Single Point Constraint
RFORCE	Rotational Force
CGAP	Nastran Contact Gap elements
DOFs	Degree of Freedom
CNTNLSUB	Continue Subcase
STATSUB	Subcase static loading for pretension
TEMPLOAD	Temperature Loading

Chapter 1

Introduction

Escalating concerns about climate change and the complications related to fossil fuel energy have underscored the public's demand for environmentally friendly and sustainable modes of transportation. In 2021, approximately 6.5 million electric vehicles, encompassing both fully electric vehicles (EVs) and plug-in hybrid electric vehicles (PHEVs), were sold globally, marking a 109% increase from the previous year's sales [13]. Forecasts suggest that one out of every four cars sold may soon be electric. Prominent automakers like Ford, Cadillac, Bentley, Chrysler, Volvo, Subaru, GM, Lexus, and Kia will be completely carbon neutral by 2035 [14]. As for the Vertical Take-off and Landing (VTOLs) market, it's expected to witness significant growth, with the market size projected to surge from USD 8.2 billion in 2022 to USD 12.9 billion by 2027, indicating a 57% increase at a compound annual growth rate (CAGR) of 9.4%. This growth is attributed to numerous issues tied to VTOLs powered by internal combustion engines (ICE), including the need for aircraft renewal, increased aircraft mass, and high operational costs [15].

The transition from hybrid to fully electric vehicles in the traction motor segment has placed significant demands on the industry to manufacture high-power, compact motors. Figure 1.1 illustrates the compilation of multiple surveys conducted to demonstrate the impact of electric motors in the VTOL segment. According to a survey conducted by Custom Market Insights [16], the primary utilization of electric traction motors was observed in railways and urban metros, with electric vehicles following closely behind in terms of usage.

The two primary categories of electric traction motors are responsible for converting electrical energy, whether alternating current (AC) or direct current (DC), into mechanical energy for generating rotational motion. These motor types are classified as AC motors and DC motors. AC motors operate by supplying alternating current to the stator, generating a magnetic field. The frequency of this magnetic field corresponds to the AC current flow. As a result, the magnetic field in the stator induces a current in the rotor and develops its own magnetic field. The interaction between these two magnetic fields leads to the production of torque and rotational motion. On the other hand, in a brushed DC motor, the armature coil of the rotor receives a direct current from the brushes through the commutator. The commutator plays a role in changing the current's polarity by making contact breaks with the brushes. As a result of the current flow, the armature acts like a magnet and generates a magnetic field proportional to the current. The stator of a brushed DC motor consists of a permanent magnet or an electromagnet with a field winding. The flow of current through the field winding of the stator generates a magnetic field, which then interacts with the armature's magnetic field, resulting in rotor motion [17, 18].

When the stator windings are activated, they generate a rotating magnetic field

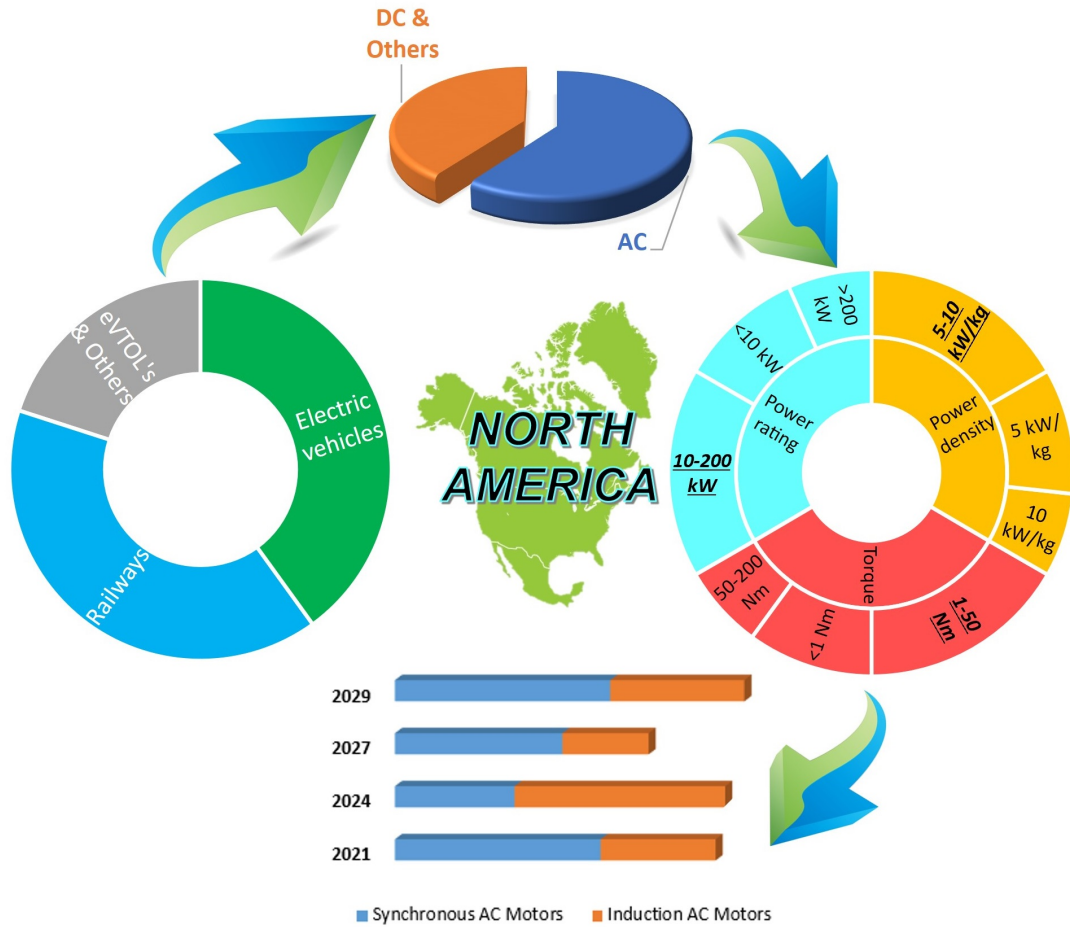


Figure 1.1: Electric machines in eVTOL market

and induce an electromotive force (emf). The rotor, which contains permanent magnets in the case of a PMSMs (a type of AC motor), is influenced by this force and rotates nearing synchronous speed. This mechanism differs from a brushless DC motor (BLDC), where the stator is wound with coils in a sinusoidal pattern. As a result, an AC power supply is necessary to operate the motor. Consequently, the motor generates a sinusoidal back emf and produces a low torque repulsion. This characteristic of low torque repulsion in a PMSMs enables it to deliver higher and smoother torque with greater efficiency and reduced noise compared to a BLDC motor [19]. One key

distinction between AC and DC motors is their speed control capabilities.

While an AC motor operates at the frequency of the AC power source, it exhibits limited responsiveness to speed changes, even when the load fluctuates [20]. The synchronous speed of AC motors is determined by the number of poles it possesses and the frequency of the power supply rather than being influenced by its voltage or load. As this thesis aims to develop a motor suitable for eVTOL (electric vertical takeoff and landing) applications, achieving a higher power density and maintaining a consistent power output range unaffected by varying loads, using an AC motor would be highly advantageous. Figure 1.1 demonstrates an industrial trend that aligns with a similar ideology, indicating a 20% greater utilization of AC motors when compared to DC motors in eVTOL applications.

When selecting an appropriate motor type, crucial factors to consider include torque, power rating, and power density [21]. These three aspects collectively encompass various aspects, such as speed, mass, efficiency, and cost, spanning across multiple segments. Figure 1.1 illustrates that the $10 - 200kW$ category is the most prevalent segment within the power rating and $5 - 10kW/kg$ for the power density segment [15]. The prevalence of these segments in eVTOL motors is primarily due to the emphasis on achieving higher power density by carefully optimizing the motor geometry and incorporating better cooling strategies. This focus on compactness and reduced mass allows for the utilization of power-dense motors and facilitates axial stacking, resulting in higher power outputs within confined spaces.

When discussing AC motors with higher power density, a gradual global shift is occurring in the traction motors industry, moving away from AC induction motors towards AC synchronous machines with permanent magnets. AC induction machines

(asynchronous machines) works based on a "slip" that occurs because of a difference in the speed of the rotating magnetic field (synchronous speed) and the rotor speed (always lesser). The slip also known as the catching-up phase of the rotor, is necessary for the induction motor to produce torque. The slip relies on various factors such as rotor resistance, stator voltage frequency, and load torque. On the contrary, synchronous motors operate at synchronous speeds, meaning that the rotational speed of both the stator's magnetic field and the rotor is identical. Consequently, with permanent magnet synchronous motors, there is no slip, allowing the rotor to rotate faster as the input frequency from the drive increases [22]. In the case of PMSMs, a PMSM-compatible drive is necessary. This drive replaces the typical trapezoidal waveform with a sinusoidal waveform that aligns with the back EMF, resulting in a more seamless and smoother output of torque.

Expanding on the previous statement, Permanent Magnet Synchronous Motors (PMSMs) exhibit high power density primarily due to two factors. Firstly, PMSMs do not possess a squirrel cage rotor winding, which leads to a reduction in rotational inertia. The absence of the winding allows for improved air ventilation, thereby enhancing thermal efficiency by providing more surface interaction for heat exchange. Secondly, the reduced rotational mass in PMSMs leads to a significant decrease in the centrifugal force experienced by the rotor. This reduction in force helps alleviate overall stress and central deflection, creating additional room for topology optimization and mass reduction. In the aerospace industry, it is known that reducing drag results in an inverse increase in thrust. Hence, the high power density advantage of PMSMs makes them a suitable choice for eVTOL applications and justifies the reason for increased usage of PMSMs over the next 6 years, showcased in Figure 1.1.

1.1 Background

PMSMs can be classified into two distinct subcategories based on the direction of the flux travel vector: Axial-flux PMSMs and Radial-flux PMSMs. In an Axial-flux motor, the flux travels in the longitudinal direction (in reference to the shaft axis) and the back iron is placed perpendicularly facing the longitudinal axis of shaft. The back iron acts as the flux deviating components and routes it back completing a closed flux loop as shown in Figure 1.2 (a). Depending on the arrangement of the permanent magnets on the rotor, there are two classifications: Surface Permanent Magnet Synchronous Motors (SPMSMs) and Internal Permanent Magnet Synchronous Motors (IPMSMs). In SPMSMs, the magnets are mounted on the surface of the back iron, while in IPMSMs, the magnets are embedded inside the rotor core.

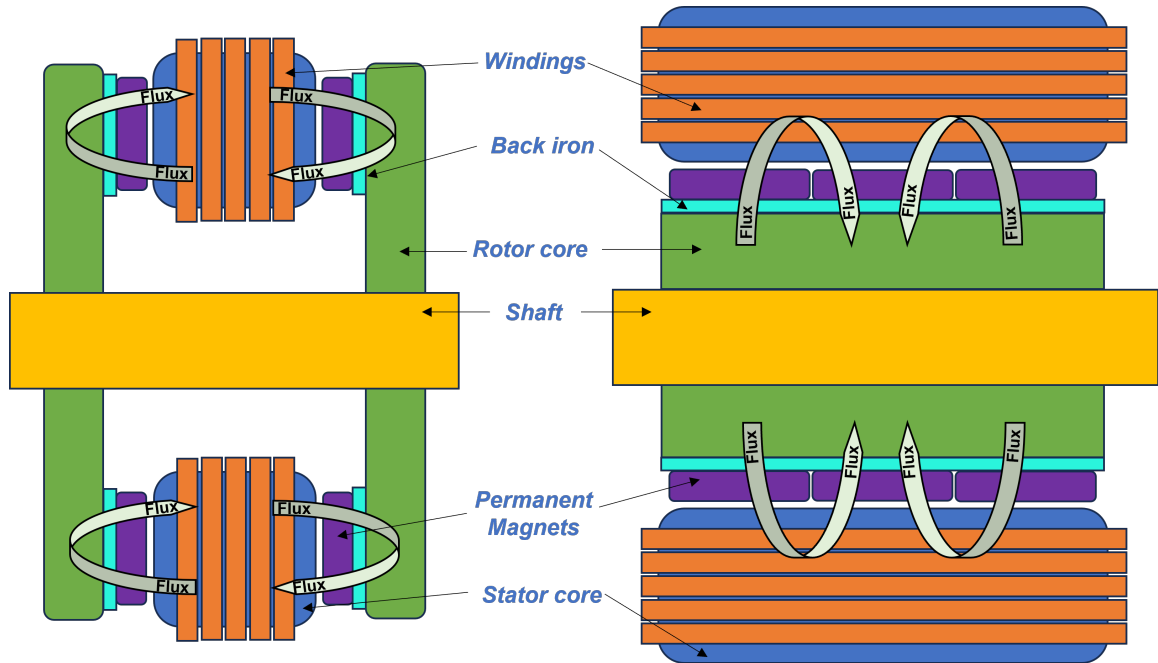


Figure 1.2: (a) Axial-flux SPMSMs (b) Radial-flux SPMSMs

Considering the electromagnetic performance, the SPMSMs have the highest air

gap flux density due to a relatively lower distance between the magnets. Adding on, the SPMSMs are selected to maximize torque at the rated speed point as there is no necessity to introduce negative d-axis current for flux weakening and the q-axis current can be varied to increase torque. A slight increase in air gap brings in small d and q-axis inductances. This results in smaller values of d-axis current, henceforth giving rise to a control strategy for flux weakening [23]. In the case of IPMSMs, specifically designed for operation in the flux-weakened region, a negative d-axis and a positive q-axis current is necessary to weaken flux and increase torque at a rated speed.

The major concern with Axial-flux SPMSMs is relating to the mechanical integrity of the rotating assembly [24, 25]. In Axial-flux SPMSMs, the permanent magnets experience centrifugal forces in the radial direction and magnetic forces in the axial direction. At the maximum torque-rated RPM, the axial magnetic forces exert a significant pulling force, leading to adhesive failure (excessive shear) between the magnets and the rotor carrier. This can result in catastrophic motor failure as the magnets are excessively deflected, potentially leading to contact with the stator poles. To prevent the magnets from detaching from the rotor carrier due to the high torque at high rotational speeds, a retention mechanism is required. However, the axial stacked construction of the motor poses challenges for the implementation of lightweight materials such as carbon fiber wrap for retention purposes. Fitment and manufacturability issues arise, thereby restricting the usage of such materials in high-speed applications.

In contrast, within a Radial-flux PMSMs, the flux path extends from the rotor to the stator core in a radial direction and then returns back to the rotor [25] as seen in

Figure 1.2 (b). When considering the direction of both centrifugal and magnetic forces which are radially preponderant, it is important to note that the influence of either force predominating will solely impact the structural performance of the rotor. In this case, with a rotating rotor mass of approximately $5kg$ and a radius of $65mm$, spinning at a rate of $20,000rpm$, the centrifugal force generated amounts to approximately 1.5 meganewtons. At the maximum torque-rated RPM, the centrifugal forces decrease to approximately $400kN$. Even at this level, the centrifugal forces remain higher than the magnetic forces at any operational point of the motor. The usage of carbon fiber, known for its superior strength-to-weight ratio, can be utilized in Radial-Flux SPMSMs as it can be wound on a mandrel and press-fitted onto the rotor easily due to the radial stack-up arrangement of the rotor assembly. The maximized retention makes the radial flux SPMSMs an ideal candidate for high-speed operations.

1.2 Motivation

Numerous efforts and advancements have been made to enhance the electromagnetic performance of Radial-flux Surface Permanent Magnet Synchronous Motors (SPMSMs). However, the research focus on extensively utilizing Finite Element Analysis (FEA) techniques to optimize the structural integrity of these motors has been relatively limited. The rationale behind this can be attributed to the limited adoption of Radial-flux SPMSMs compared to Radial-flux IPMSMs across various applications. As a result, SPMSMs have been relatively overlooked, finding their presence confined within research laboratories, academic literature, and patent filings, despite being in existence for nearly two decades. Regarding the research papers, while many of them delve into conducting comprehensive electromagnetic analyses to determine the

optimal sizing of magnets for achieving superior performance in motors, the focus on assessing the durability of these motors appears to be relatively limited.

For instance, the authors of [26, 3] have laid out magnet sizing and mechanical construction of a Radial-flux SPMSMs. The authors primarily focus on mechanical integrity, but considering an incorrect boundary definition by applying constraints on the shaft or simplifying the problem by applying "slipped boundary constraints" on the permanent magnets leads to instilling additional stiffness in the model. Applying additional assembly stiffness (which happens with incorrect boundary conditions) in finite element analysis (FEA) changes the model behavior to either an increase in the stress at bearing shoulder locations (load transfer intersections) or an incorrect displacement contour. Concluding the design process without generating a frequency array encompassing eigen, critical, electrical, and operational frequencies can potentially result in resonance issues. These resonance effects can lead to excessive shaft whirling [27] or fatigue development in supporting boundary components, such as motor casing and bearing shims. Therefore, it is crucial to include a thorough analysis of the frequency spectrum to mitigate the risk of resonance-related problems. Chapter 4 clearly outlines the common structural design-associated problems and their possible countermeasure that will be explained in this thesis.

1.3 Thesis Contribution

Radial-flux Surface Permanent Magnet Synchronous Motors (SPMSMs) have been extensively studied in the literature for the past two decades. However, a design is considered complete only when these motors are successfully implemented in practical applications. The aim of this thesis is to start from where most of the literature

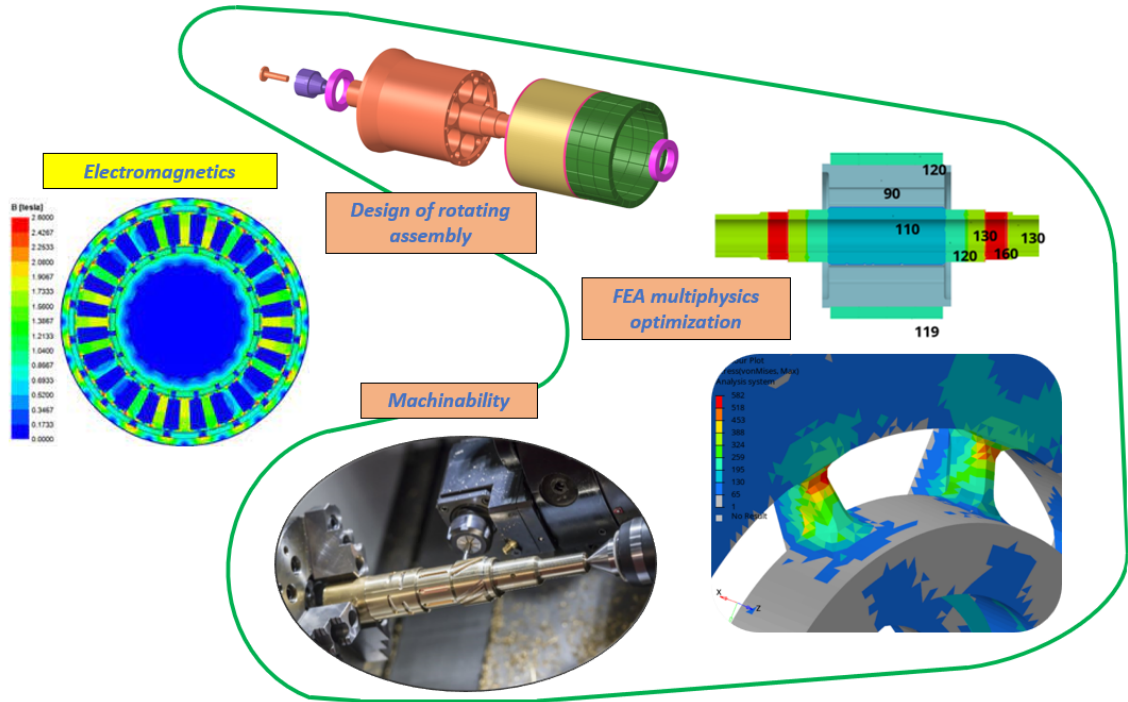


Figure 1.3: Mechanical design cycle

papers conclude, i.e., to propose generic mechanical solutions by utilizing comprehensive non-linear FEA to address the challenges outlined in the previous section. These solutions are intended to be applicable to any Radial-flux SPMSMs, regardless of the motor’s specifications. Figure 1.3 shows a simplified life cycle process for the design of a Radial- flux SPMSMs. The electromagnetic design phase is briefly discussed with determining the appropriate sizing of magnets and back iron for optimal performance. This is because there exist numerous intricate literature sources that focus on enhancing the electromagnetic performance of Radial-flux SPMSMs [24, 26, 3, 28].

Once the dimensions of the magnets and back iron are finalized, the thesis continues by addressing the design process of the complete assembly of both the rotating and stationary components of the motor. Throughout this stage, careful attention

was given to factors such as ease of manufacturability, durability, and lower rotational inertia. The manufacturability checks were conducted at every design stage with machining experts, and necessary suggestions were applied and reiterated to study structural impact. The durability was ensured using a physical test-like scenario in FEA combined with rigorous use of finite element multiphysics setup. A secure and stable base design was established, serving as the foundation for further development. Subsequently, optimization techniques were employed to enhance the mass and topology of the integrated design, aiming to achieve reduced rotational inertia. By reducing the rotational inertia, the centrifugal forces experienced by the rotor assembly were consequently diminished. This not only resulted in more uniform loading on the bearing but also contributed to reduced component stress caused by radial forces.

1.4 Thesis Outline

The main objective of this thesis outline is to highlight the crucial role of FEA in optimizing the durability of the integrated design to enhance power density, particularly in the context of aerospace applications. Additionally, it aims to emphasize the significance of carefully selecting appropriate boundary conditions to ensure accurate and reliable analysis results. The thesis will commence with a concise introduction, outlining the rationale behind selecting Radial-flux SPMSMs and highlighting their advantages, such as their simpler and structurally integral construction, which makes them suitable for high-speed operations compared to Axial-flux SPMSMs.

Chapter 2 primarily centers around two key subjects: the aerospace applications and construction of Radial-flux SPMSMs. SPMSMs are widely utilized in diverse

aerospace applications, with a notable prevalence as thrust sources for eVTOL vehicles. This preference is primarily attributed to their high power-density characteristics and the capability to achieve maximum torque during high-speed operations. This section will provide a general examination of the electromechanical components and their working comprising a Radial-flux SPMSMs.

Chapter 3 presents a comprehensive exploration of the rotating mechanical components of a contemporary Radial-flux PMSMs, encompassing aspects of design, manufacturing, and assembly. The subsections also address the limitations and drawbacks associated with the existing rotating assembly, intending to compare them with the integrated design of shaft and hub proposed in the new few chapters.

Chapter 4 embarks on the initial phase of the integrated design by examining the implications of substituting the conventional non-oriented electrical steel with a low-alloy steel like AISI 4340. This latter material is highly regarded for its remarkable core strength, wear resistance, and toughness, rendering it a favored option for a wide range of high-speed applications. Within this chapter, a succinct assessment of the electromagnetic performance of both materials is conducted, revealing promising indications favoring the utilization of AISI 4340 for the rotor core. Chapter 5 showcases the design procedure adopted towards the integrated design, such as considerations on shaft and core dimensions, core air ventilation layout, cooling fan integration with tension ring, assumptions of FOS for the preload force on bearings, carbon fiber sleeve retention calculation and several other considerations crucial towards a reliable design. In addition, this chapter reinforces the notion of enhancing ease of manufacturability by focusing on design features aimed at reducing the manufacturing costs associated with the component.

Chapter 6 presents a comprehensive overview of the static multiphysics simulation, incorporating the integration of thermal plots from CFD analysis with structural loading to examine the thermal stress experienced by various components. Additionally, the chapter delves into the dynamic framework, discussing the extraction of detailed eigenmodes and exploring their impact on the overall design process. Chapter 7 and Chapter 8 are interdependent and crucial chapters in the thesis, as they collectively contribute to preparing the rotating assembly for the manufacturing phase.

Chapter 7 illustrates the pre-processing methodologies employed for finite element modeling and integration, encompassing aspects such as meshing analogies, efficient convergence of contact analysis, modeling of boundary conditions including stator bolts and constraints, carbon fiber complex-composite modeling, and the application of interference methodologies. An optimal consideration of boundary constraints and loading are further discussed in this chapter. In this chapter, the post-processing of results entails an extensive examination of strains, thermal stress risers, and displacement patterns. The objective is to verify the stability of the model and assess whether all components remain within the elastic deformation region of the material's stress-strain curve. Furthermore, the analysis involves studying the strain energy densities alongside previously obtained results and through meticulous parametric optimization, ensuring the development of a reliable design.

Chapter 8 focuses on the vibrational characteristics of the motor by analyzing its eigen frequencies through specific eigen-mode analysis (free-free and constrained). Additionally, the chapter includes the analytical estimation of the critical speed using

modified Dunkerley and Rayleigh’s method. Furthermore, a frequency array is tabulated, encompassing the eigen, critical, electrical, and operating frequencies of the motor, enabling the evaluation of potential resonances within the analyzed model. Chapter 9 provides a concise overview of the machining and assembly processes required for manufacturing the complete rotating assembly, including the integrated design. This section will also highlight common manufacturing challenges and demonstrate how these issues can be effectively addressed by implementing minor design modifications. Chapter 10 will encompass several testing procedures aimed at measuring strain and temperature. Specifically, half-bridge strain gauges will be employed to obtain data that can be used to establish a correlation between the test results and FEA data. In Chapter 11, the thesis will conclude with a summary, highlighting the key findings and conclusions. Additionally, this chapter will touch upon potential areas for further optimization in the design, serving as a basis for future work and research.

Chapter 2

SPMSMs for More Electric Aircraft

The utilization of Radial-flux SPMSMs in aerospace propulsion applications is attributed to various advantages, including a simplified machine design, enhanced rotational integrity, increased torque at rated speed, and higher power/torque density. The Clean Sky initiative is making significant investments in exploring and implementing strategies to promote environmentally responsible operations throughout all stages of aircraft utilization. Among the prominent initiatives garnering considerable attention is the concept of utilizing electrical machines for traction during the taxi phase of an aircraft, known as Green Taxiing (GT) [29]. This innovative scheme aims to enable aircraft to maneuver on the ground without relying on the main engines or traditional airport tow trucks. This effectively establishes the dominance of synchronous machines as the preferred choice for numerous electro-mechanical actuators in wheel applications. The utilization of electrically powered equipment is generally on the rise in the aerospace industry. Typically, this movement is referred

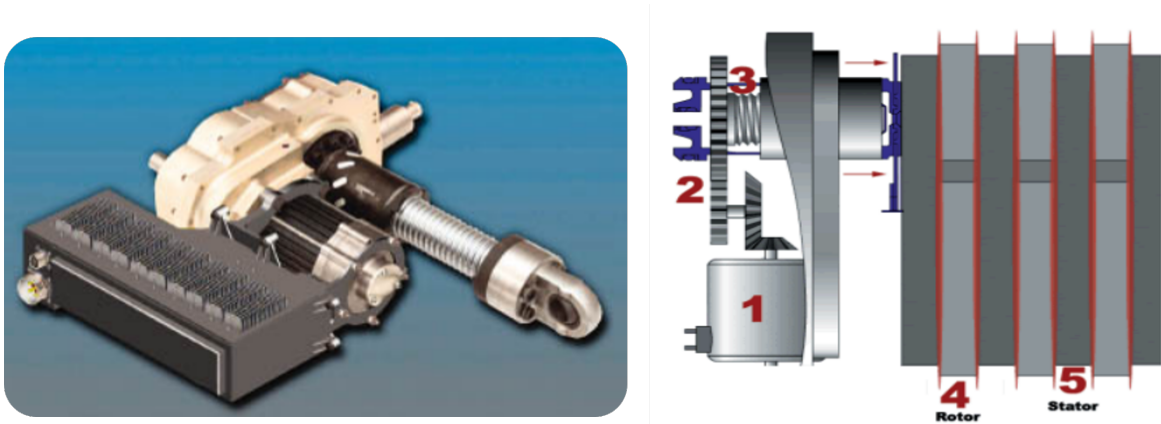


Figure 2.1: Advanced motor drive - EMA (left); Electric brake - Boeing aircraft (right) using PMSMs [1]

to as "Power-by-Wire" or "More Electric Aircraft" (MEA). In addition to providing considerable technological and financial advantages over traditional mechanical, hydraulic, or pneumatic systems, new electric-powered systems can satisfy these objectives. In his article, Wenping [30] proposed analytical techniques to evaluate the relative benefits of caged induction, reluctance, and PM motor technologies for MEA applications. Figure 2.1 in the referenced source highlights various applications of Radial-flux PMSMs, as mentioned by the authors. According to the research, the dual (or triple) three-phase PMAC motor drive could be a good option for general aerospace applications since it strikes an equilibrium between redundancy and complexity, ensuring a balanced functioning in the event of a breakdown.

The application of Radial-flux PMSMs in More Electric Aircraft (MEA) has been implemented since the early 2000s. In 2002, Mitcham [31] proposed the concept of using PMSMs as generators for the low-pressure (LP) shaft in gas turbine engines. This LP generator would provide power to the aircraft when the engine is shut down during flight. The authors argue that, considering a reasonable level of fault tolerance,

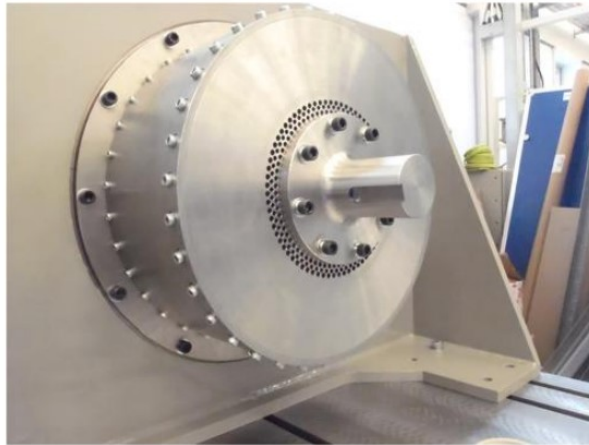


Figure 2.2: GT traction hub motor designed for aircraft taxiing [2]

the PM generator is preferred due to its high specific weight, efficient performance across different speeds, ease of cooling, robustness, and potential for greater reliability than conventional wound field generators.

In recent years, there has been an increasing focus on adopting traction hub motors for aerospace applications in line with advancements in green taxiing. In a publication by Galea [2], the use of an outer rotor Radial-flux SPMSMs for a wheel actuator traction motor (WATM) was designed and tested as shown in Figure 2.2. The selection of the appropriate motor type for such applications poses common challenges, including the need to achieve high torque density and meet fault tolerance requirements. To address these challenges, the authors opted for a Radial-flux SPMSM with a Halbach array configuration and concentrated windings. A Halbach array encourages more substantial sinusoidal air gap flux density, which increases the ratio of the fundamental air gap flux (which generates torque) to the overall air gap flux. This setup influences the stator core's saturation, thereby increasing the machine's maximum peak torque capability [32]. Companies like Amazon, Joby Aviation, Volocopter, and others are investing significantly in the eVTOL (electric Vertical Takeoff

and Landing) market. These companies recognize the potential of these lightweight aircraft for a range of applications, including unmanned military missions, grocery deliveries, and short-distance travel. While there have been numerous advancements focused on enhancing the electromagnetic performance of Radial-flux SPMSMs [33], the significance of mechanical construction has often been overlooked. This thesis seeks to address this gap by emphasizing the importance of mechanical design and how a well-simulated design approach can contribute to increasing power density and improving motor reliability.

Chapter 3

Electromagnetic Construction of a Radial-Flux SPMSMs

Radial-flux SPMSMs have specific dimensions for each component. They are determined by the overall output of the machine and the optimization strategies are framed to obtain the desired performance. A generic layout and explanation will be provided for the three main divisions of Radial-flux SPMSMs, namely the electromagnetic, structural, and thermal design. The design process begins by determining the stack length of the laminated electrical steel and the dimensions of the permanent magnets. The electromagnetic analysis is then conducted to verify the virtual performance, and subsequent optimization is performed to achieve a balance between high power output, minimal losses, and a lighter overall design. The entire structure and thermal aspects of the motor are developed around the established electromagnetic components, with the aim of achieving a high level of structural integrity. Several authors have extensively studied the electromagnetic performance of an electric motor

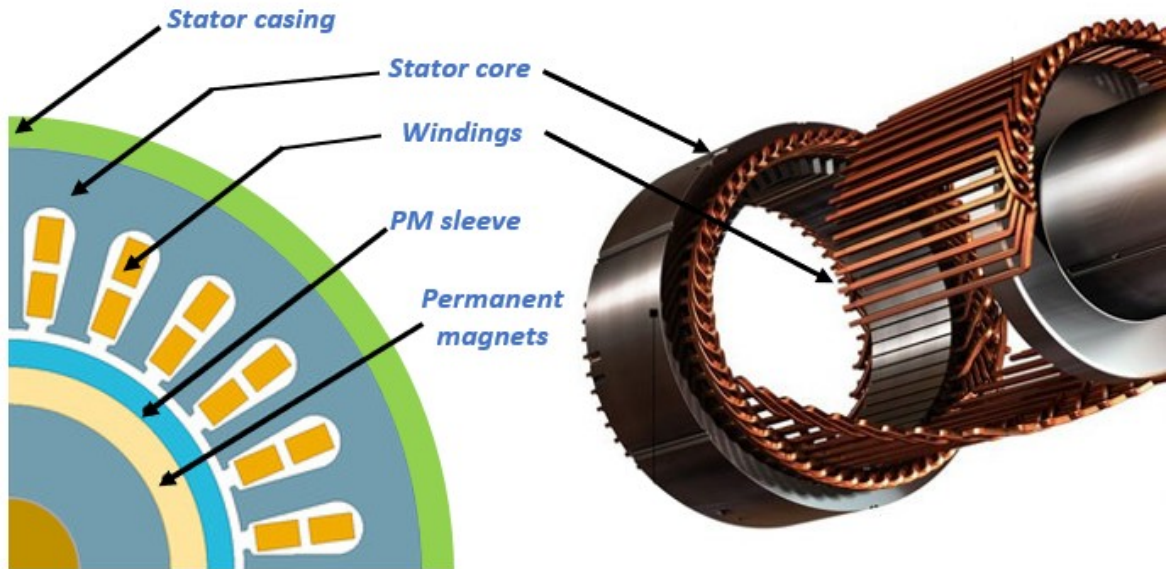


Figure 3.1: Simplified cross-sectional view of the stator assembly of a Radial-flux SPMSMs [3]

[24, 26, 3, 28], with numerous literature sources focusing on optimizing its performance. However, for a brief overview, the electromagnetic components of an electric motor can be categorized into two main assemblies: the stator and the rotor.

3.1 Electromagnetic Assembly of the Stator

Figure 3.1 illustrates the stator assembly, primarily comprising the laminated slotted stator core, stator windings, and the supporting casing. Examining the functionality of each component, the stator core is composed of stacked and laminated electrical steel sheets, forming a cylindrical shape with slots to accommodate the stator windings. These windings consist of insulated copper coils that are inserted into the slots of the stator core. The stator assembly is enclosed and safeguarded by the stator housing.

3.1.1 Stator Copper Windings

As per Ampere’s law [34], the flow of current in a conductor gives rise to generating a magnetic field. This magnetic field forms circular patterns around the conductor, following the right-hand rule. Applying these principles, the copper stator windings have specific PMSMs functions.

Generation of Magnetic Fields: The stator windings are responsible for carrying an electric current, resulting in the creation of a rotating magnetic field. This rotating magnetic field interacts with the rotor’s permanent magnet’s magnetic field, leading to torque generation and motor rotation.

Electromagnetic Conversion: The stator windings perform the crucial task of converting electrical energy into a rotating magnetic field. When energized with alternating current (AC), the magnetic field produced by the windings undergoes changes in direction and strength, causing the rotor to rotate.

Control and Regulation: The stator windings of a PMSMs are usually supplied with AC current. The stator windings offer control and regulation capabilities for the motor. By adjusting the amplitude and frequency of the current supplied to the windings, the speed, torque, and direction of the motor can be controlled. This allows for customization of the motor’s performance based on specific operating requirements.

Two main classifications of windings used for PMSMs are overlapped and non-overlapped windings [4]. The overlapped windings are further divided into concentrated and distributed winding shown in Figure 3.2. Distributed windings in Permanent Magnet Synchronous Motors (PMSMs) involve the uniform distribution of numerous windings across the stator core. Each winding is divided into multiple coil sections and placed in various slots around the stator core. This arrangement ensures

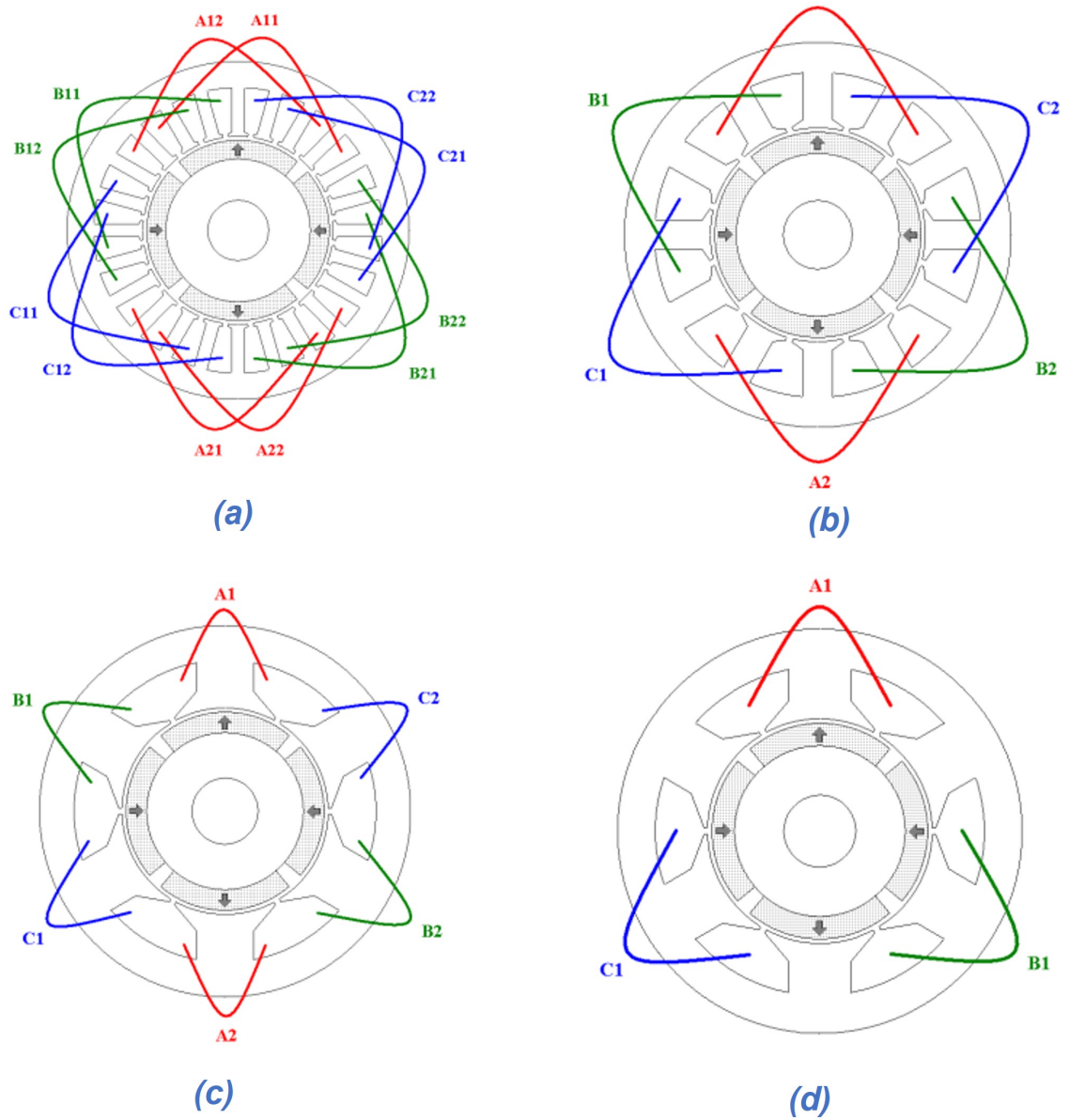


Figure 3.2: Overlapped winding - (a) distributed, (b) concentrated; Non-overlapped winding - (c) all teeth wound (d) alternate teeth wound [4]

a balanced and even distribution of the magnetic field, minimizing the presence of harmonics and their associated effects (lowered rotor and magnet eddy current losses). Distributed windings in PMSMs offer advantages such as reduced torque ripple and improved motor efficiency. However, there are also some limitations associated with distributed windings. These include longer end turn lengths, as a result of their complex overlapped configuration over different poles, lower copper fill factor, and a higher difference in d-axis and q-axis inductances, which are more favorable for IPMSMs rather than SPMSMs.

Conversely, concentrated windings consist of a single winding placed in a single slot of the stator core. This winding typically comprises multiple coil sections connected in either series or parallel but results in higher harmonic content in motor magnetic field, resulting in a higher torque ripple and lower power factor. But concentrated windings are known for significantly simplifying the manufacturing process and reducing winding complexity, lower-end turn length and lower reluctance torque, which are more favorable for SPMSMs than IPMSMs. Fractional slot concentrated windings in PMSMs are characterized by having fewer slots per pole and phase, where each coil spans multiple slots. This arrangement creates a concentrated winding layout with a reduced number of slots utilized compared to the total number available in the stator core. The benefits of this configuration include improved distribution of the magnetic flux, minimized harmonic effects, and increased utilization of the available space for the winding, resulting in enhanced motor performance [4].

The number of turns in the stator core of a PMSMs indicates the count of wire loops or windings wrapped around the stator teeth. These windings form coils, and the combination of these coils, connected either in series or parallel, constitutes the

stator winding. The number of turns plays a significant role in determining the electrical characteristics and overall performance of the motor. The number of turns are dependent on various factors such as magnetic flux density, operating frequency, voltage, area of core and wire dimensions (based on AWG standards). When the motor operates at higher voltages, the number of turns in the motor's windings increases, leading to a corresponding rise in the back electromotive force (EMF). The back EMF acts in opposition to the applied voltage and is directly related to the number of turns. As the back EMF strengthens, it diminishes the current drawn by the motor by counteracting the applied voltage. Consequently, the reduction in current results in a decrease in torque production since torque is directly proportional to the current ($T=KI$). Increasing the number of turns also increases the end turn length, thereby increasing the machine size.

3.1.2 Stator Core

The stator core is another useful component of the electric motor that completes the flux path from the stator field windings to the rotor. The stator core has the below-mentioned functionalities.

Support for stator windings: The stator core is crucial in providing structural support to the stator windings, ensuring their proper positioning within the motor and alignment with the rotor magnets. This support is essential for efficient power transfer and optimal performance.

Flux conduction: The stator core serves as a conduit for the magnetic flux generated by the stator windings. It helps guide and direct the magnetic field lines, allowing them to interact effectively with the rotor magnets. This interaction is necessary to

produce the desired torque in the motor.

Magnetic circuit: The stator core, along with the rotor and the air gap between them, forms a closed magnetic circuit. This circuit enables the flow of magnetic flux from the stator to the rotor and back, facilitating the transfer of energy between the electrical and mechanical domains. The stator core ensures the completion of this magnetic circuit, supporting the overall operation of the motor.

As the functioning of the stator was discussed earlier, the determination of the number of salient poles in the stator of an electric machine is influenced by various factors, including design considerations, performance requirements, and manufacturing constraints. Several key factors that impact the selection process are listed below.

Electrical frequency: The number of poles is typically chosen to achieve the desired electrical frequency of the machine. The relationship between frequency (f) and rotational speed (N) is given by $f = p \cdot N / 120$, where p represents the number of poles. The number of poles can be determined based on the desired frequency and speed of operation.

Mechanical limitations: The physical size and spatial constraints of the machine may impose restrictions on the number of poles. More poles generally require a larger stator diameter, which can affect the overall size, weight, and cost of the machine.

Torque and power requirements: The number of poles influences the torque output and power characteristics of the machine. Higher pole numbers can provide higher torque density but may result in lower power density. The desired torque and power requirements of the application are considered when determining the number of poles.

Harmonics and efficiency: The number of poles affects the harmonic content of the magnetic field, which can impact the efficiency and performance of the machine. Best

practice is to minimize harmonics and achieve a balanced magnetic field distribution by selecting an appropriate number of poles.

Manufacturing factors: The manufacturing process and capabilities also play a role in determining the number of poles. Some manufacturing methods may be better suited for specific pole configurations, and considerations of manufacturability and cost-effectiveness are important.

A variety of materials are available for use as the stator core in electric machines. These materials include silicon steel (also known as electrical steel), cold-rolled grain-oriented steel, nickel-iron alloys, and amorphous metal alloys such as metallic glasses. Among these options, silicon steel is the most commonly used material due to its favorable combination of high magnetic permeability and low core losses. Nickel-iron alloys are gaining popularity in high-performance motors, and a study conducted by Jasim [35] compared various parameters such as stator and rotor losses, torque, efficiency, power output, and flux density for different stator and rotor core materials. The study concluded that nickel-iron alloy performs exceptionally well in terms of efficiency, torque, rotor losses, and iron losses, making it a promising choice for high-performance motor applications.

According to Joule’s law [36], the heat produced in a conductor is directly proportional to the square of the current, the resistance, and the duration of the current flow. As a result, the flow of current in the stator windings leads to resistance and the subsequent generation of heat. Utilizing hollow conductors in certain motors has demonstrated their effectiveness in enhancing coil cooling. However, this comes at the cost of increased motor size and added complexity in coil manufacturing [37].

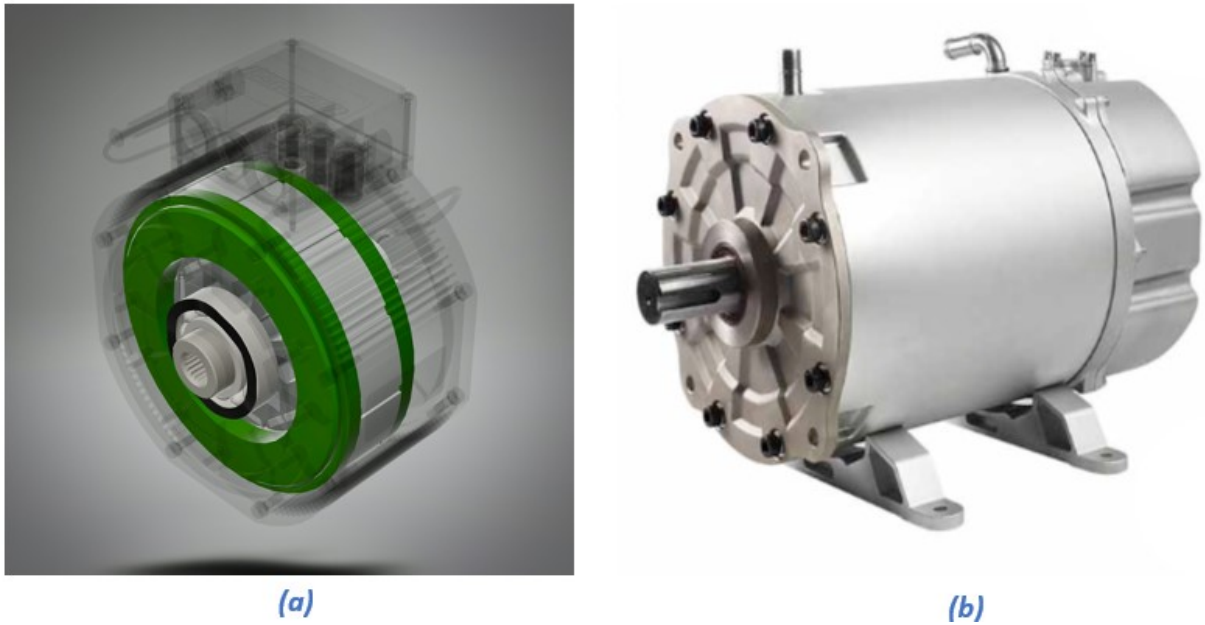


Figure 3.3: (a) Encapsulation of stator core and windings [5] (b) Stator casing design [6]

3.1.3 Encapsulation and Stator Casing

The encapsulation of the stator assembly shown in Figure 3.3 serves multiple important functions in PMSMs. Firstly, it acts as a protective barrier, safeguarding the stator windings and internal components from environmental elements like moisture, dust, and contaminants. This protective measure ensures the durability and reliability of the motor assembly over its operational lifespan. Additionally, during sudden accelerations that induce torque in the shaft, the encapsulation plays a role as a transfer path mechanism, effectively transmitting the torque to the stator casing. This improves the overall stiffness and stability of the stator assembly, enhancing its structural integrity. Furthermore, the encapsulation material functions as an electrical insulator, creating insulation between the stator windings and the motor housing or other conductive parts. This insulation is crucial in preventing electrical short

circuits and ensuring the safe and efficient operation of the motor. Moreover, the encapsulation material has the ability to dampen vibrations and minimize the transmission of mechanical vibrations from the stator to the motor housing and external components. By reducing noise and vibration, it enhances the overall performance and smoothness of motor operation. Lastly, the encapsulation material assists in thermal management by facilitating heat dissipation and providing insulation properties. It helps maintain the optimal operating temperature of the stator windings and other internal components by incorporating cooling jackets within the stator casing. This prevents overheating and ensures the motor operates efficiently.

The encapsulation is effectively fastened and positioned with metal clamping rings or axial interlocks to ensure stability and prevent any axial displacement or circumferential rotation during sudden motor torque conditions. The stator casing serves as a platform that brings together all the stator and rotor elements while accommodating features like cooling channels and additional components such as the inverter setup. The design of the stator casing is meticulously crafted to enhance assembly rigidity, including raising the eigen frequency, to prevent the occurrence of resonance with critical, electrical, or operational frequencies of the shaft.

3.2 Electromagnetic Assembly of the Rotor

The rotor assembly of a motor plays a significant role in generating structural loads, unlike the stator, which is primarily responsible for cooling and vibration absorption. The electromagnetic components within the rotor assembly include the permanent magnets and the rotor laminations, as shown in Figure 3.4. The primary purpose of permanent magnets is to establish a steady magnetic field when energized. On the

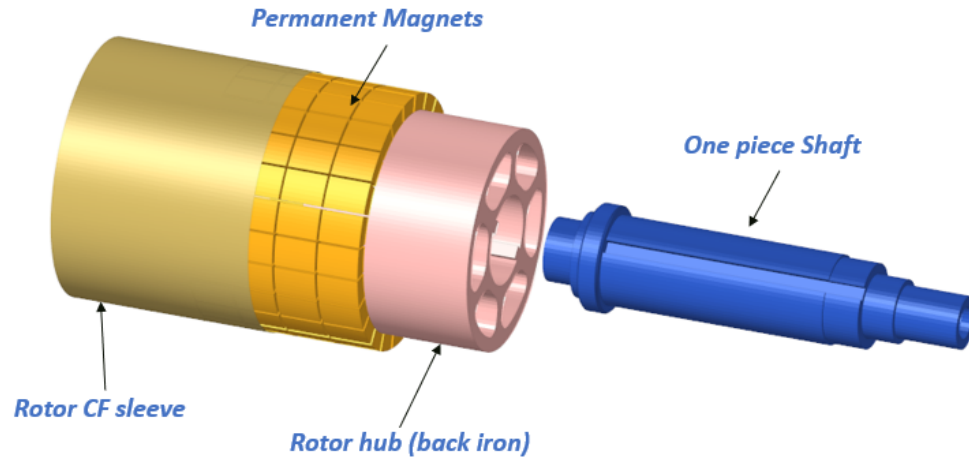


Figure 3.4: Rotor assembly mainly showcasing the electromagnetic components

other hand, the rotor core serves as a conduit for the magnetic flux and provides support to the magnets. Further details regarding the functionality of these components will be elaborated in the subsequent sections.

3.2.1 Permanent Magnets

Permanent magnets (PMs) are composed of ferromagnetic materials, including iron, nickel, cobalt, and their alloys. However, there is a growing trend of using rare-earth materials such as neodymium, samarium, terbium, and dysprosium in PMs due to their exceptional performance characteristics. Before delving into a detailed exploration of the materials used in PMs, it is essential to understand the fundamental working principles of permanent magnets.

When permanent magnets are magnetized, they generate a magnetic field by aligning the atomic or molecular magnetic dipoles within the material. These dipoles arise from the alignment of electron spins in the atomic or molecular structure of the material. Magnetization occurs by subjecting the material to a strong magnetic field

or a specific temperature gradient, which aligns the magnetic dipoles in a particular orientation, leading to the creation of a powerful magnetic field within the material. Magnetization are classified into two types of process namely the static and pulse magnetization. In static magnetization, the magnetic material is exposed to steady magnetic field that charges the magnetic domains based on the field direction. Whereas in pulse magnetization, a large pulse of current is passed through a coil surrounding that produces a powerful magnetic field, thereby magnetizing the permanent magnet and is commonly preferred for high-performance magnets.

The coercivity of the magnetic material and, to a smaller extent, the physical properties of the magnet and any potential fixture assembly affect the magnetising force necessary for saturating a magnet. According to the general rule, a peak field that is 1.5 to 2.5 times its inherent coercivity must be applied in order to saturate a magnet [38]. This magnetic field extends from the magnet's north pole to its south pole, forming magnetic field lines. These field lines generate a magnetic flux that can interact with other magnetic fields, such as those produced by stator windings in a motor. The strength of the magnetic field produced by a permanent magnet is influenced by factors such as the material composition, magnetization process, and physical dimensions of the magnet. Permanent magnets, such as neodymium iron boron (NdFeB) or samarium cobalt (SmCo), are chosen for their high magnetic coercivity, which means they are resistant to demagnetization and can retain their magnetization over an extended period which is an important characteristic feature for high-speed traction motors [39].

A Halbach array is a specialized configuration of permanent magnets that generates a concentrated magnetic field on one side while minimizing the field on the

opposite side. By arranging the magnets in a pattern where their magnetization vectors alternate in direction, a unique magnetic field distribution is achieved. This arrangement boosts the magnetic field strength on one side while effectively reducing the field (stray field is generated) on the other side. This asymmetrical magnetic field distribution offers several benefits in traction applications, including improved torque production, enhanced efficiency, higher power density, and optimal utilization of magnetic materials.

3.2.2 Rotor Core

The rotor core serves a similar purpose and is constructed in a similar manner to the stator core, but it does not contain any coils. However, unlike the stator core, the rotor core is subjected to significant mechanical loads that are directly influenced by the speed of the machine. The rotor core performs several critical functions, which are outlined below.

Magnetic circuit and field conduction: The rotor core plays a crucial role in establishing a closed magnetic circuit in conjunction with the stator and the air gap between them. This circuit facilitates the smooth flow of magnetic flux from the stator to the rotor and back (closed flux loop), ensuring efficient energy transfer between the electrical and mechanical domains. Additionally, the rotor core acts as a conduit for the magnetic field generated by the stator windings, guiding and directing the field lines to interact effectively with the permanent magnets, thus facilitating efficient torque generation.

Mechanical and thermal support: The rotor core provides essential structural support for the permanent magnets, ensuring their proper positioning and alignment

relative to the stator. This support is crucial for withstanding mechanical stresses and centrifugal forces that arise during motor operation, particularly at high speeds. Furthermore, the rotor core assists in reducing central deflection and minimizing shaft eccentricity, thereby maintaining a consistent air gap. Additionally, the rotor core aids in heat dissipation by conducting and distributing heat away from the permanent magnets. This helps to keep the magnets and the overall motor operating within optimal temperature ranges, promoting reliable performance and longevity.

The rotor core consists of stacked laminations made from similar materials as the stator core. These laminations are typically fabricated using laser cutting techniques and stacked together to achieve the desired stack length. The thickness of rotor laminations in a motor is significant because it affects the overall performance and efficiency of the motor. Thinner laminations offer lower eddy current losses, reduce magnetic losses, and improve the motor's efficiency. Thicker laminations, however, provide increased mechanical strength and robustness to withstand the mechanical stresses experienced during operation.

Chapter 4

Contemporary Design of Rotor Assembly of Radial Flux SPMSMs

Several advancements have been made in the structural design of the rotor assembly of a Radial-flux SPMSMs with the aim of enhancing power-density [40]. These include the utilization of composite materials for magnet retention, which has facilitated further optimization of the rotor geometry. As a result, the mass of the core was optimized, leading to improved high-speed performance of the machines [41]. One persistent challenge has been the uneven loading on the bearings caused by eccentricity. However, the introduction of hybrid ceramic bearings has shown promise in mitigating bearing and frictional losses associated with high-speed eccentricity. Several other current state-of-the-art design features will be addressed in this chapter. In this chapter, we will delve into a comprehensive discussion on the design of each rotating component shown in Figure 4.1. The insights gained from this analysis will serve as a valuable reference point for the integrated design discussions in the forthcoming chapters.

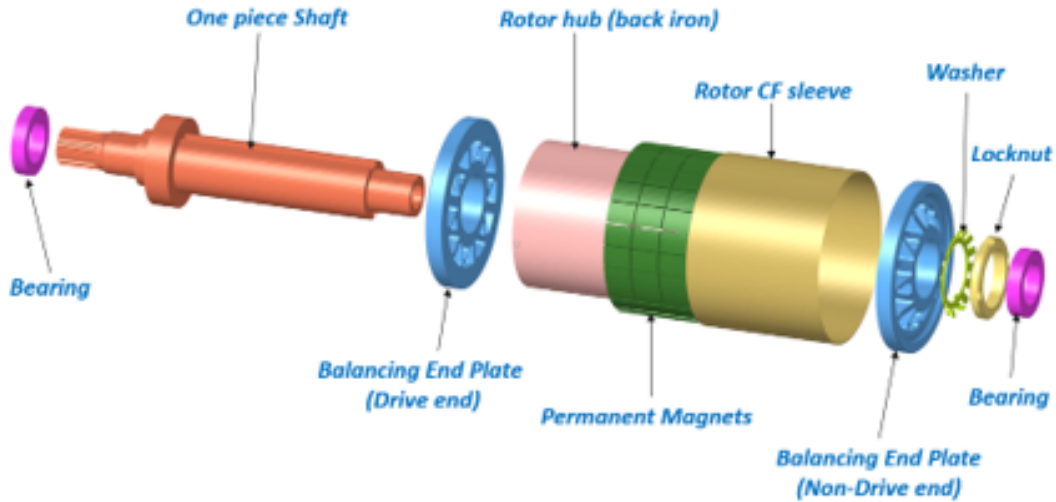


Figure 4.1: Contemporary FE design of a Radial-flux SPMSMs[7]

To facilitate meaningful comparisons, it is essential to establish a standard motor specification. In this case, a $150kW$ motor with a peak torque of $75Nm$ at $20,000rpm$ will serve as the benchmark for an eVTOL (electric Vertical Take-Off and Landing) application. The specific goal for this application is to achieve a power density of over $7kW/kg$. It is important to note that the electromagnetic design of the motor is already finalized and will be considered as a fixed parameter as the thesis focuses more towards the structural optimization of the rotating assembly and its boundary-sharing components. The same motor specification will be carried forward into the integrated design phase, as it represents a seamless continuation of the existing contemporary design.

4.1 Design of Shaft and Rotor Hub

The function of the shaft in a traction motor is to supply pulsated torque to the powertrain and handle undue acceleration without fatigue [17, 42]. The shaft for

the contemporary design of a Radial-flux SPMSMs is designed to endure $75Nm$ of torque and a maximum speed nearing $22,000rpm$ (with a design safety margin of 1.1), which makes the design and analysis procedure complex. With an overall rotating assembly mass of approximately $6.5kg$ over a radius of $61mm$ (sizing of magnets after performing electromagnetic analysis) spinning at $22,000rpm$, the shaft will encounter a centrifugal force of about $2.1MN$. This requires the material to have a higher yield strength and fatigue resistance. The most commonly used shaft material is the AISI 4340 which is a low-alloy steel known for its excellent machinability (even with 50 rockwell hardness), wear resistance to press fits and higher core strength.

A yield strength of $850MPa$ can be obtained upon austenizing the AISI 4340 at $845^{\circ}C$ for direct hardening and tempering at $425^{\circ}C$ to relieve stresses produced during the “thru-hardening” process [43]. But doing so will cause the shaft to behave extremely stiff or, in other terms, becomes brittle in nature. This yields torsional stiffness reducing the ductility of the shaft, i.e., a brittle core, which may promote failure during maximum service conditions. To achieve a balanced tensile core and compressive outer case, “induction case-hardening” is adopted. The shaft is heated in an induction coil environment and then quenched to make the surface harder [44]. The depth of the case hardening depends on the heat that is applied. Higher temperatures and slower scan rates promote a higher penetration of hardening. A case depth of 0.125 to 0.150 inches is typical for stock shafts and 0.3 inches for a selective high-strength application.

To design the shaft for comparative analysis, the traditional analytical method calculates the two important parameters, i.e., the minimum and maximum diameter of the shaft. From the strength criterion formulae, the ratio of motor torque (T) to

the polar moment of inertia (J) is a function of the ratio of shear strength (F_s) to the radius of shaft (R) as shown in equation

$$\frac{T}{J} = \frac{F_s}{R} \quad (4.1.1)$$

From Equation 4.1.1, the polar moment of inertia J for a solid shaft is $\frac{\pi}{32}D^4$. A FOS of 1.3 was considered for the maximum torque in order to accommodate sudden motor torque surge. The minimum diameter is calculated as 11mm by substituting the known values of torque and allowable shear stress in Equation 4.1.1. Upon rearranging Equation 4.1.1,

$$\frac{T}{F_s} = \frac{J}{R} \quad (4.1.2)$$

The $\frac{T}{F_s}$ ratio is calculated from a solid shaft and can be used in a hollow shaft since material properties and torque will remain constant. For hollow shafts, the ratio of outside diameter to inside diameter is considered as 2 and can be changed as per design constraints. From solving Equation 4.1.2, the minimum outside diameter is 12mm and the minimum inside diameter is 6mm. Due to specific design constraints from selected bearing diameter, shaft manufacturability, the designed shaft upon scaling 3.5 times has a maximum diameter of 42mm and a minimum diameter of 18.2mm. Figure 4.2 showcases the stepped shaft design that consists of 2 keyways. The maximum key length must be within 1.5 times the diameter of shaft to minimize twisting [45] but is not necessarily applicable for every design. The rotor hub is made of laminated steel with inbuilt keys. Such a design upon stacking will require the keyway on the shaft to have a length larger than the key to accommodate sliding of

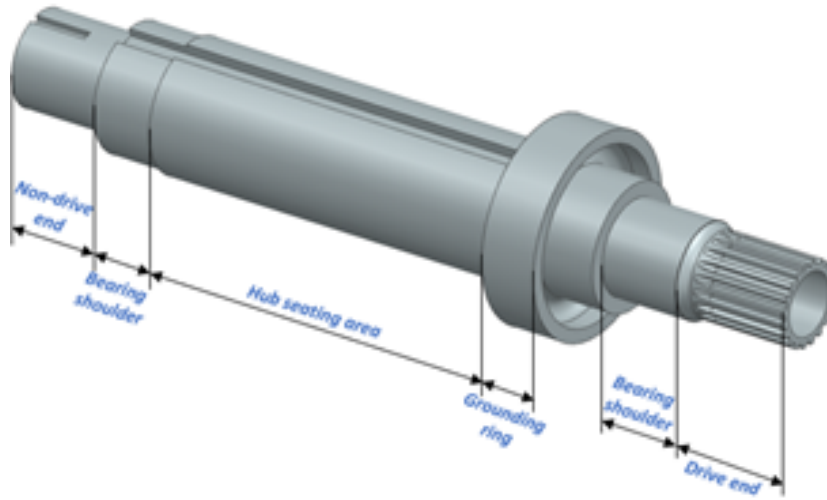


Figure 4.2: One-piece shaft design

laminated rotor hub. The shear force experienced by the designed shaft is $4.76kN$ obtained from the Equation 4.1.3,

$$\tau = \frac{\text{Torque}_{\max}}{\text{Radius}_{\text{shaft}}} \times \frac{1}{(\text{Length of keyway} \times \text{Width of keyway})} \quad (4.1.3)$$

The shear stress on keyway is calculated using the shear force from Equation 4.1.3 and results in 10MPa. One of the keys will be responsible for the torque transfer, whereas the other keyway kept 180° apart is for redundancy. A one-piece design approach is applied where the shaft can be produced from a single AISI 4340 bar of OD $44mm$, using major machining processes such as turning, milling, and broaching. The introduction of a one-piece design removes complex multi-interface press fits stepped shafts and provides even stress distribution.

The rotor back iron completes the magnetic circuit as the flux lines flow through the rotor back iron. Henceforth, the back iron should be a magnetic material otherwise there will be a significant increase in the magnetic circuit reluctance. The increase in

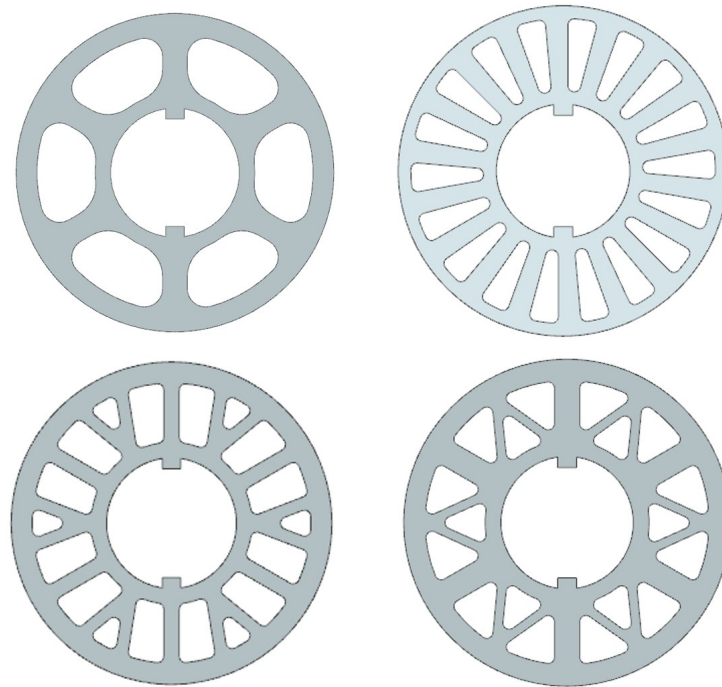


Figure 4.3: Different types of optimized laminated hub design

the magnetic circuit reluctance due to the use of a non-magnetic back iron reduces the coils flux linkage and hence reduces the machine torque significantly. In order to have a higher power density machine, the rotor back iron should be manufactured out of magnetic steel to reduce the magnetic circuit reluctance and increase the machine flux linkage and hence increase the machine torque. But this is only applicable when the PM's do not have the halback array configuration discussed in section 3.2.1. The rotor losses in the SPMSMs are the PM loss, the back-iron loss, the windage loss, and the bearing loss. The PM losses and the back iron loss are eddy current losses that the back iron lamination and the PM segmentation can limit. The back iron is made of non-oriented silicon laminated steel with $0.2mm$ lamination thickness to reduce back iron eddy current loss. Non-oriented silicon steel is chosen due to its high magnetic

saturation point compared to common magnetic material and lower cost than Cobalt-steel laminations. Several advancements are made in the internal shape of the rotor core shown in Figure 4.3. The back iron thickness was maintained at about 6mm, and the supporting structure was framed around the back iron. The primary constraint lies in the relatively low yield strength of the electrical steel, which poses challenges in optimizing the rotor core for enhanced strength and improved ventilation.

4.2 Design of Permanent Magnet

The rare earth permanent magnet on the rotor hub provides the machine with the magnetic flux required for torque production. Rotor coils can produce this magnetic field for machines like field-excited synchronous machines. The problem with field-excited synchronous machines is that they require brushes to connect the rotor coils to the DC supply, which reduces machine reliability. The PMSMs do not require brushes, as the rotor PM provides the required flux for torque production. The performance of any PM-based machine can be enhanced by carefully choosing the right PM material [46]. Neodymium Iron Boron (NdFeB), which has a greater maximum energy product than Samarium Cobalt (SmCo), and a higher coercivity and remanence flux density, has been chosen for this application.

This selection improves the power density of the machine due to the high airgap flux density that the NdFeB magnets can provide compared to the SmCo magnets. To improve the airgap flux density further, the halback array configurations are used [47]. The segmentation of the halback array helps in reducing the eddy current loss of the PM. A brief comparison of NdFeB and SmCo magnets is provided in Table 4.1. NdFeB magnets are chosen due to their high remanence flux compared to the

Non rear earth magnets	NdFeB	SmCo
<i>Density (g/cm³)</i>	7.5	8.4
<i>Composition</i>	Nd = 29-32.5%	Sm = 35%
	Fe = 63.9-68.6%	Co = 60%
	B = 1.1-1.2%	Fe = 2.5%
	Re = 0.6-1.2%	Cu = 2.5%
<i>Remenant flux density (T)</i>	1.1	1.0
<i>Compressive strength (MPa)</i>	900	850
<i>Youngs modulus (GPa)</i>	160	150
<i>Thermal conductivity (W/m.K)</i>	10	10
<i>Torque density (kN/m³)</i>	67	56
<i>Cost effectiveness (USD/Nm)</i>	1.5	2.09

Table 4.1: Comparison of electrical and mechanical properties of NdFeB and SmCo permanent magnets [12]

Samarium-Cobalt magnets (SmCo). The maximum continuous operating temperature of the NdFeB magnet is lower than SmCo magnets. Demagnetization temperature is determined by the load curve of the magnets on the demagnetization curves and it is found that as the machine operates at 150°C , there is no demagnetization. It is also to be noticed that the demagnetization temperature of a NdFeB PM is about 180°C to 240°C . However, the maximum operating temperature of most of the high-speed rotors is around 150°C , which means NdFeB can be used to benefit from its high remanence flux to increase the machine power density and its lower cost to reduce the machine cost compared to the SmCo.

4.3 Design of Axial and Radial Rotor Assembly Retention Systems

When the motor functions at $22,000rpm$ under full load conditions, the PM temperature can go up to $120^{\circ}C$, resulting in thermal expansion and thereby introducing stress risers in various components [48]. The laminated rotor back iron is stacked with layers of laminated sheet and adhesives, which when exposed to a thermal gradient from the PM, will expand. This expansion might cause the stacks to become loose, causing catastrophic failures in electric motors [49]. Henceforth to provide axial retention, the end plates are designed to secure the rotor laminated stacks from the ends. The end plates can be designed for two reasons, to provide axial retention and rotor shaft balancing activities.

Figure 4.4 provides an accurate description of the balancing rings and their position in the assembly. The material commonly used for the balancing end plates is either an aluminum alloy (6061 or 7068) or low-alloy steel plates, being known for their superior strength and fatigue resistance properties at elevated temperatures. Aluminum 7068 is used for high-speed applications as it has a yield strength of $414MPa$ at $150^{\circ}C$, which is better performing than traditional Aluminum T66061 with a $220MPa$ yield strength at $150^{\circ}C$. Other Aluminum alloys, such as Aluminum 7078 (aerospace grade), have a lower yield strength at elevated temperatures. The balancing end plates comprise a raised lip contributing nearly 25g of mass per side for dynamic balancing activities during rotor testing. The manufactured laminated rotor stack is sandwiched between the two balancing end plates as shown in Figure 4.4, and a full-faced tight-fit contact is provided between the two components with

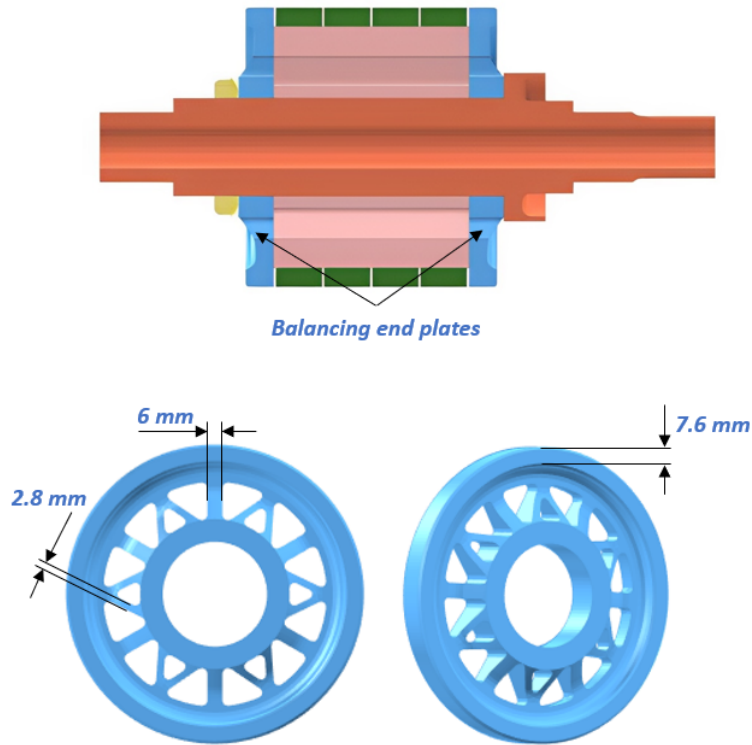


Figure 4.4: (a) Location of balancing end plates in motor assembly (b) Side and (c) Isometric view of end plates with dimensions

minimal pretention. A radial flux motor with end plates is a common element for axial retention and can even be found in Tesla Plaid S and other common PMSMs constructions for aerospace applications [50]. The balancing end plates have a press fit contact with the shaft and are axially constrained by using the washer and locknut from SKF, as shown in Figure 4.4. Once the balancing end plates are press fitted with a calculated interference, the washer with flange is inserted, proceeded by the locknut having a tight fit threaded connection to the shaft. Since both the balancing end plates and washer have a press fit, a very high axial preload for the washer is unnecessary, as some room for expansion will reduce the internal stresses of the laminated rotor core. While stacking and compressing, the laminated electrical plates

may be joined using intermediate adhesives, interlocking pin hooks, or seam welds [51] are provided at specific locations for additional stacking stiffness and assembly fixture. Certain types of lamination stack-up might not have the axial end plates but instead have a through bolt setup to hold laminations in place.

In Radial-flux SPMSMs, the centrifugal forces are dominant and will have a ripping effect on magnets causing catastrophic machine failures [52, 53]. To ensure radial retention, a sleeve is selected and tightly fitted around the permanent magnets. This sleeve can be made of either metal or composite material, providing a secure hold through a slight interference fit. While using a metal retaining sleeve, it was found that there is an increase in the eddy current loss in the rotor, majorly caused by spatial and time harmonics. In some cases, it causes overheating zones and demagnetization of permanent magnets [52]. Composite materials such as fiberglass or carbon fiber have very high electrical resistivity, which reduces the rotor eddy current losses [54]. The chosen carbon fiber in this thesis is Hextow IM7, and its composite property has a tensile modulus of 164GPa , tensile strength of 2700MPa , and a CTE of $6.4e^{-7}/C$. In comparison to other composite matrices, the CTE for carbon composites is considerably lower, which makes it an ideal candidate for high-tension sleeves due to its increased strength and thermal stability.

The carbon fiber being orthotropic in nature, has its strength and rigidity aligned highest in the tensile direction of fiber and lowest in the transverse fiber direction. This indicates that the fibers must be aligned so that maximum stiffness is achieved along the vector of radial expansion. Carbon fiber sleeves are manufactured using a process called filament winding. The carbon fibers are sourced from suppliers with specific strength capabilities. A suitable resin is chosen based on the bonding strength

and curing temperature. While designing the carbon fiber sleeve, it is critical to consider the resin impregnation losses on the final sleeve, as the carbon fiber volume in a unit would be considerably lesser as the resin takes up space for bonding. The % loss is based on the resin impregnation and is generally between 25 to 35%. The pre-preg carbon fibers are in strands of thin filaments following a specific width and resin coating that are wound with a calculated minimal prestress across a rotating rotor with PM. The carbon fiber sleeve is filament wound using a slight initial interference fit of 0.01mm representing tension of 33 pounds per tow (1 tow = 24,000 strands of carbon fiber) with which the sleeve is filament wound on the PM's. If an extremely tight interference fit is applied, the strain on the longitudinal fibers could increase under high-speed conditions, potentially resulting in fiber tearing. At times the filament winding is done on a mandrel with the same tolerance and outside diameter as that of the PM. This process is chosen when the magnet demagnetization temperature is closer to the curing temperature of the resin used for bonding carbon fiber filaments. A filament winding is generally unidirectional, with an angle varying between 80 to 89 degrees per turn of a filament which is decided based on the strength required and thickness of the sleeve.

4.4 Issues with Contemporary Design of Rotor Assembly

In the previous sections, we explored the key structural design considerations of the rotor assembly in the contemporary design of radial-flux SPMSMs. In this section, we will delve into the associated challenges. Listed below are some of the common

mechanical challenges that the industry faces when it comes to the contemporary rotor design of Radial-flux SPMSMs. This thesis aims to address these challenges by employing suitable FEA methodologies with mechanical considerations to offer effective solutions.

- **Structural integrity** -

Reason → The presence of multiple press fits results in a coefficient of thermal expansion (CTE) mismatch between components, which can give rise to fatigue cracks, particularly when operating at very high speeds.

Countermeasure proposed → Reducing press fits by integrating the shaft and hub machined from a solid bar of AISI4340 using high stress-bearing materials.

- **Manufacturing complexity** -

Reason → When multiple press fits are involved, precise control of tooling tolerances becomes essential. For the laminated electrical steel core, achieving the desired tolerances for shaft fit necessitates meticulous processes such as high-precision laser cutting, inter-sheet welding, and precision surface grinding.

Countermeasure proposed → By integrating the shaft and rotor hub, the requirement for electrical steel and its associated components, including axial retention end plates, locknuts, and washers, can be eliminated. This integration significantly reduces the necessity for high-precision machining since the integrated shaft/hub can be CNC-lathed from a single steel bar.

- **Lower power density** -

Reason → Usage of low-strength electrical steel results in less stress-bearing capability of the component. Henceforth mass is added to increase local stiffness

that increases rotational mass, thereby reducing power density. The absence of employing suitable FEA methodologies to optimize topology and mass can lead to sub-optimal design outcomes, either by under-designing or over-designing components.

Countermeasure proposed → By utilizing high-strength steel for both the shaft and hub, combined with a meticulous assessment of boundary stiffness, there is increased potential for mass optimization while maintaining a higher level of reliability in FEA.

- **Poor thermal performance** -

Reason → To enhance core stiffness and reduce shaft deflection, a significant amount of material is added. However, this approach inadvertently reduces available space for ventilation, resulting in increased rotor core temperatures and bearing shoulders (due to bearing losses) during high-speed operation. As a consequence, high operating temperature conditions arise.

Countermeasure proposed → Study and implementation of topology optimized rotor core designs prioritizing lower shaft central deflection while positioning air vents closer to the back iron. This strategic approach aims to enhance heat dissipation for improved thermal management and reduced central mass.

- **Magnet demagnetization** -

Reason → Many motors employ retention sleeves composed of high-strength materials like Inconel and titanium, ranging in thickness from 2 to 5mm depending on operational speeds. However, the increased thickness of these sleeves inadvertently acts as a thermal barrier, impeding heat dissipation and causing

elevated magnet temperatures. Most magnets have a demagnetization temperature range of 140 to 180C. Insufficient heat dissipation from the magnets, coupled with reduced air ventilation for the rotor back iron, can lead to magnet temperatures exceeding the demagnetization threshold, resulting in motor stalling.

Countermeasure proposed → The utilization of ultra-high strength composite materials like carbon fiber enables a remarkable reduction in sleeve thickness by approximately 60%. This reduction is attributed to the unique properties of carbon fiber, which is an orthotropic material. Unlike isotropic materials, carbon fiber does not exhibit yield strength but rather a maximum tensile strength ranging between 2000 to 3000MPa (considering post-resin impregnation losses). This characteristic feature allows the material to withstand stress without experiencing plastic deformation until it reaches its ultimate strength, distinguishing it from isotropic materials that undergo plastic deformation after the yield point.

Chapter 5

Impact of AISI4340 vs

Non-oriented Electrical Steel

In the integrated design, the permanent magnets are held in place by the laminated rotor back iron. To ensure stability, axial locking end plates secure the laminations and facilitate their attachment to the shaft. However, this configuration can lead to challenges in maintaining structural integrity. One potential solution is to combine the hub and shaft, creating a single piece made from the same material. This approach enhances structural integrity and reduces the likelihood of any issues arising from the integration of multiple components. Before proceeding with this step, it is crucial to recognize the importance of Halbach array, electrical steel, and its laminations, as well as the reasons behind their application. Most traction PMSMs use conventional PMs where the magnetic field is strong on both sides, as shown in Figure 5.1. The laminated back iron serves as a conduit to effectively direct and guide the magnetic field, enabling efficient torque generation by the permanent magnets. By insulating the laminations from each other, eddy current losses are minimized as the circulation

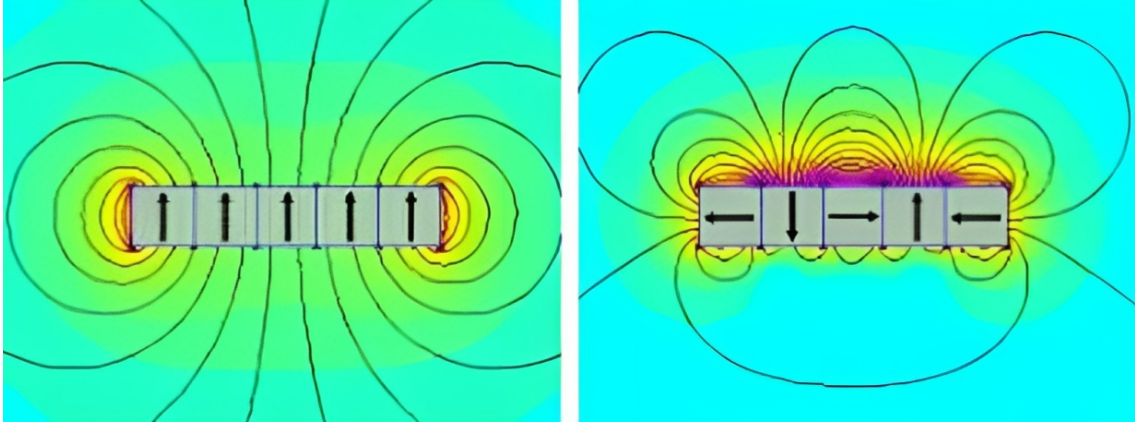


Figure 5.1: Magnetic field strength of Normal PM's (left) and Halbach-array PM's (right) [8]

of eddy currents is impeded. Additionally, the presence of laminations disrupts the continuous path of magnetic flux, leading to reduced energy dissipation in the form of hysteresis losses.

In contrast, the Halbach array arrangement generates a powerful magnetic field on one side while producing a less significant stray field on the opposite side, as shown in Figure 5.1. Based on the information provided in Figure 5.1, it can be deduced that the requirement for laminated electrical steel is eliminated [55] since the magnetic field on the rotor side is negligible. Therefore, it is possible to consider using a non-electrical steel material as an alternative for the rotor core. Furthermore, a 4-segment Halbach array configuration is chosen in the design as it improves the field distribution [56] and higher torque production [57]. Given the selection criteria of considering alternative materials to electrical steel or soft-magnetic materials, it is important to note that the magnetic permeability of such materials would be significantly lower. Therefore, the choice of AISI 4340 is justified based on its exceptional wear resistance, high core strength with a yield strength of 800MPa after heat treatment, ease of

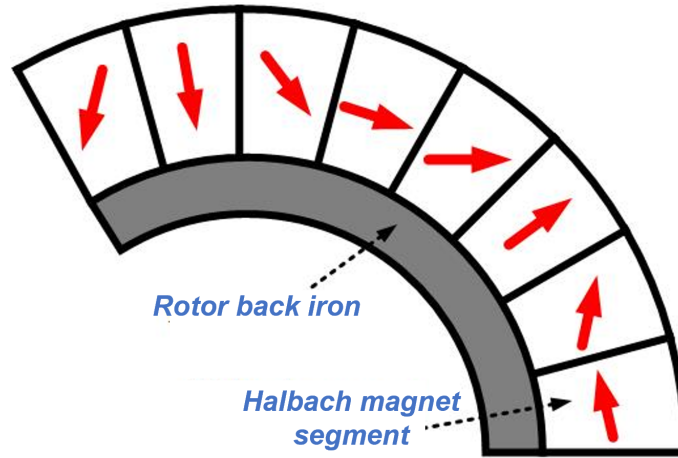


Figure 5.2: A 1/3 electromagnetic model of the rotor with 4-segment Halbach array /pole configuration

machinability even with a hardness of 50 Rockwell, cost-effective, and easily available in the market. As shown in Figure 5.2, the magnetic field is directed to follow the magnetization pattern of the Halbach segments.

The machine performance is simulated using the non-oriented silicon steel with 0.2mm lamination thickness and AISI 4340 rotor hub. While it is not mandatory to use a magnetic material for the back iron in the case of Halbach array magnets, there is still a minimal amount of flux present. Therefore, a thin rotor back iron made of AISI4340 is utilized, and its impact is examined. The back iron thickness for

Variables	Non-oriented silicon steel	AISI4340
Power (kW)	155	155
Average torque (Nm)	74	74
Torque ripple (%)	4.7	6.3
Phase voltage (V)	743	740
Magnets loss (W)	84	79
Total loss (kW)	3.77	3.77

Table 5.1: The machine’s electromagnetic performance with the different rotor hub material

both cases is 6.8mm . TABLE 5.1 shows the performance of the machine with the two materials. It can be concluded that changing the rotor material to AISI 4340 steel had a negligible effect on the torque production capability of the machine, thanks to the Halbach array configuration. The overall power output, average torque, and phase voltage remained unaffected, but there was a slight increase in the torque ripple %. However, considering the numerous structural advantages of using AISI4340, a trade-off was made, as the increase in torque ripple was deemed negligible. It was found that the rotor back iron thickness could be reduced further since the Halbach array configuration is used. It was determined that a final back iron thickness of 5mm is necessary, as reducing it further would negatively impact the torque production capability of the machine.

Chapter 6

Design Considerations for Integrated Design

The integrated design combines the purpose of a shaft, rotor hub and balancing rings into a single machined component made from AISI 4340. Figure 6.1 shows a major component reduction from the traditional design shown in Figure 4.1. The main focus of this chapter is to examine four factors that, when incorporated into the integrated design with careful considerations and assumptions, will improve the high-speed performance of the machine. Furthermore, a thorough FEA validation will confirm the impact of the considerations and assumptions.

Improve structural integrity -

The main objective for improving the contemporary design is to simplify the model and reduce stress development. In the contemporary design, the rotor shaft is composed of alloy steel that undergoes tempering and case hardening. It has a yield strength ranging from $700 - 850\text{MPa}$ and a CTE of $1.3e^{-5}/C$. The laminated rotor hub is constructed from non-oriented sintered electrical steel, commonly used, with a

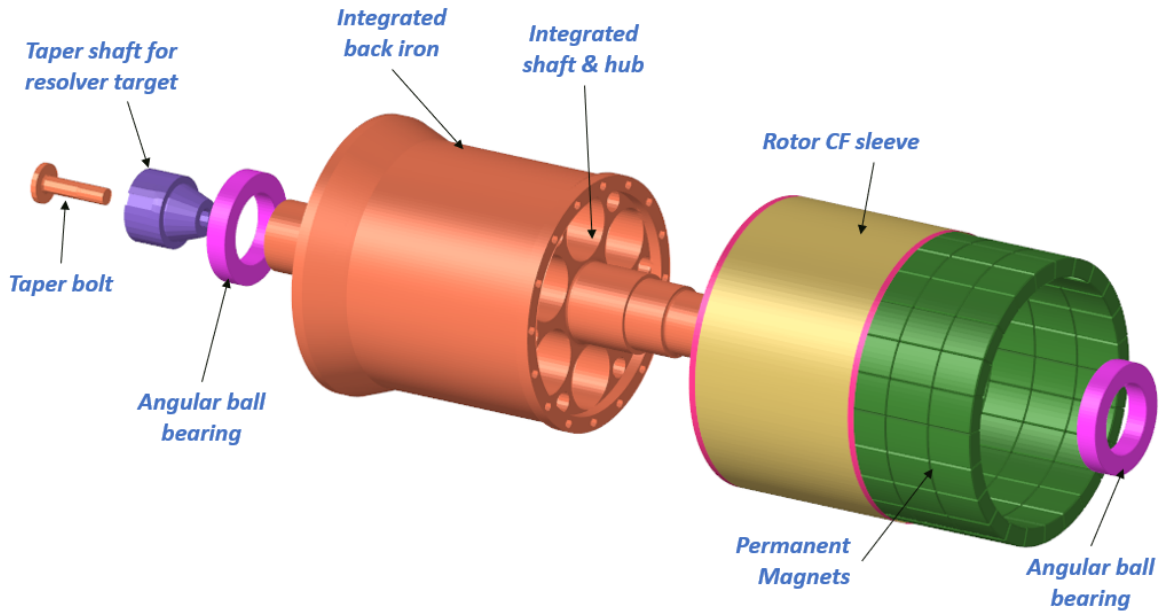


Figure 6.1: An FE representation of the integrated design

yield strength of 350 to 500MPa and a CTE of $1e^{-5}/C$. The laminated rotor core and the shaft are press fitted together with intermediate bonding through welding, and they are secured with a key on the shaft and a keyway on the rotor core. At high-speed operation, elevated temperatures occur due to increased bearing losses and magnet temperatures. These elevated temperatures cause thermal stresses in both the shaft and laminated rotor hub. Due to the different CTE's of the two materials, the rotor back iron, being the weaker material, experiences greater expansion in proportion to its expansion ratio. The shaft induces compressive stresses on the key thereby increasing local strain at key attachment regions on the rotor hub. One possible solution to address this issue is to introduce a slight clearance or backlash in the joining of the rotor hub and shaft. This allows for some space for expansion during high-speed operation but may have an impact on the structural integrity of the rotor. Additionally, the rotor manufacturers have mentioned that it is not feasible to provide

a diametric interference fit on the ID of the laminated electrical steel due to challenges in achieving high dimensional tolerance with laser cutting. Grinding the ID after attaching the laminations could potentially lead to fatigue on the laminations due to the clamping force or heat generated during machining.

By adopting the approach of machining both the shaft and rotor back iron from a single block of AISI 4340, the complications arising from CTE mismatch or the need for press fits can be eliminated. The reduction in mass by removing components relating to axial retention from the contemporary design also corresponds to a significant decrease in centrifugal force experienced by the rotor components at higher speeds. The lower the rotational inertia, the better lower will be the shaft deflection. Moreover, using AISI 4340 provides additional benefits, such as a higher yield strength of 800MPa post-heat treatment, which allows for better accommodation of bearing bending stresses and optimization of material distribution in the rotor core. The ratio of tolerable stress to material density increases [58], allowing for further design optimization to reduce weight. Certain considerations made while designing and analyzing the integrated design for structural integrity include analyzing the yield strength of the material lower than 800MPa . The yield strength of the material would be much lower in the manufactured product since a thru-hardening procedure is not adopted instead a case hardening with a depth between 3 and 4mm is considered leaving the core of the shaft to be ductile. This improves the bending stiffness allowing a higher degree of flex yet having compressive stresses on the surface level resisting bending.

The selected adhesives from Delo are of the highest strength, boasting a tensile strength of 75MPa and a shearing strength of 30MPa . However, it is evident that at

20,000rpm, the adhesive will experience much higher stresses than 75MPa. This will result in the magnet fly-by condition by not providing the required radial retention. To address this concern and enhance structural integrity, the carbon fiber sleeve is employed to safeguard the magnets. The adhesives can still be utilized as a potting material for the segmented PMs, creating a smooth surface for the carbon fiber sleeve to be wound on. The design of the carbon fiber sleeve requires specific attention due to its orthotropic nature of having very high strength in its longitudinal direction. Carbon fiber, with its low CTE and a modulus of elasticity 12% higher than steel, creates a rigid boundary that expands less than the magnets. Considering that the PMs have low tensile strength, it is necessary to segment them. Without segmentation, bending of the shaft generates tensile stress on the magnets, leading to fatigue. Segmentation reduces the load on the PMs, allowing the carbon fiber sleeve to better engage in providing the magnet retention without causing fatigue to the PM's.

Reduce manufacturing complexity

The manufacturing complexity of the contemporary design is higher due to the requirement of multiple press fits and specialized tolerance-specific machining. Table 6.1 references the manufacturing processes involved in the contemporary design to that with the integrated design for the shaft and rotor core. The shaft used in the contemporary design can be made of high-carbon alloy steel, such as AISI4340, which incorporates Nickel to enhance strength and fracture resistance. In the conventional machining process for the contemporary design, the outer radius is turned, and the inner diameters are drilled. However, for longer shafts, thru-drilling is avoided due to potential uneven runout resulting from tool deflection during prolonged drilling activities. Therefore, halfway drilling is conducted on both sides, and a final reaming

	Contemporary design	Integrated design
<i>Shaft</i>	Material - Shaft steel Manufacturing process - 1) Conventional lathe turning for all OD's. Lathe drilling for the ID. 2) Broaching or milling of key slots 3) Surface grinding and smoothing for final dimensional tolerance 4) Tempering - relieve internal stresses 5) Nitriding - compressive surface stresses	Material - AISI 4340 Manufacturing process - 1) 3 Axis CNC lathe for all OD's. Lathe drilling for slots and shaft ID 2) Surface grinding, reaming and smoothing for all dimensional tolerances (runout specially) 3) Rotor balancing after machining with fan mass. 4) Tempering and nitriding
<i>Rotor hub</i>	Material - Laminated electrical steel Manufacturing process - 1) High-precision laser cutting of laminations 2) Fusion or spot welding of laminates 3) Insulative insertions, clamping fixtures, jigs for rotor core stacking 3) Surface grinding after stacking near key regions and OD to achieve high tolerance	

Table 6.1: Machining processes involved in the contemporary vs integrated design

process is utilized to achieve the required dimensional tolerance. The key slots can be milled using either broaching or 2-axis milling methods. The latter option may be more expensive, but it can achieve higher tolerances. Afterward, a final surface grinding and smoothing process is performed to eliminate any surface roughness that could lead to excessive wear or fatigue cracks. The most common shaft surface finish is maintained at $0.10\mu m$ to strike a balance between the necessary lubrication roughness for bearings and wear protection under high-stress conditions. After the surface finishing processes, there may be residual tensile stresses in the material, which could potentially cause fatigue cracks under cyclic loading. Tempering is carried out to

alleviate these residual stresses resulting from machining and additional hardening. Nitriding, a relatively newer technology, is a form of case hardening that involves heating the shaft and diffusing nitrogen onto the surface, enhancing its wear and fatigue resistance. The rotor core comprises laminations made from electrical steel, which can be produced using laser cutting or hydro-cutting methods. Hydro-cutting is a cost-effective option, but it may result in lower manufacturing tolerances than laser cutting, which is pricier but provides above-average tolerance levels. The laser-cut laminations are carefully stacked using special jigs and fixtures in a controlled pressure environment to prevent buckling caused by excessive clamping forces. During the stacking process, fuse or seam welding is applied to ensure the alignment and structural integrity of the stacks. A final step involves surface grinding on the key and outer diameter locations for magnet fixtures to achieve the required manufacturing tolerances.

In contrast, the integrated design demands a simpler approach, relying on regular lathe turning, preferably using CNC technology for precise geometric positioning. Unlike the contemporary design, the integrated design eliminates the need for specialized setups due to the absence of laminations. However, it is still advisable to perform rotor balancing after machining, as using a solid block of material may result in varying material density, which could affect the overall balance of the rotor.

Increase power density

Having a lighter rotor assembly offers three significant benefits. Firstly, reduced rotational inertia leads to higher power output, as less energy is needed to move the unit volume, resulting in improved efficiency. Secondly, lower rotational inertia translates to reduced centrifugal force, allowing for better optimization of material

Rotating assembly	Mass (kg)	
	Traditional Design	Integrated design
One piece shaft	2.3	4
Rotor core	2.8	
Balancing end plates (clamping)	0.5	NIL
Bearings	0.68	
Permanent Magnets	1.7	
CF sleeve	0.09	
Locknut & Washers	0.09	NIL
Taper shaft & Bolts	0.25	0.1
Total	8.41	6.57

Table 6.2: Mass savings between contemporary and integrated design

volume and enhanced performance. Lastly, a lighter rotational mass results in a higher power density, making the system more efficient overall. As shown in Table 6.2, implementing the integrated design allows for the elimination of components like clamping end plates and associated parts, resulting in a reduction of assembly mass by 26%. The total mass of components, including bearings, PMs, carbon fiber sleeve, taper shaft, and bolts, remains constant as the primary goal of the integrated design is to enhance structural integrity. However, through a well-planned FEA, the integrated design was optimized to weigh approximately 4kgs , resulting in a significant mass reduction of 1.1kgs compared to the traditional design, which weighed around 5.1kgs .

Improve thermal performance

The contemporary design faced significant thermal challenges due to the requirement of additional material in its core to withstand the stresses. However, the integrated design overcomes this limitation by saving more mass in the core, resulting in increased space for air to flow and thereby improving thermal performance. Figure

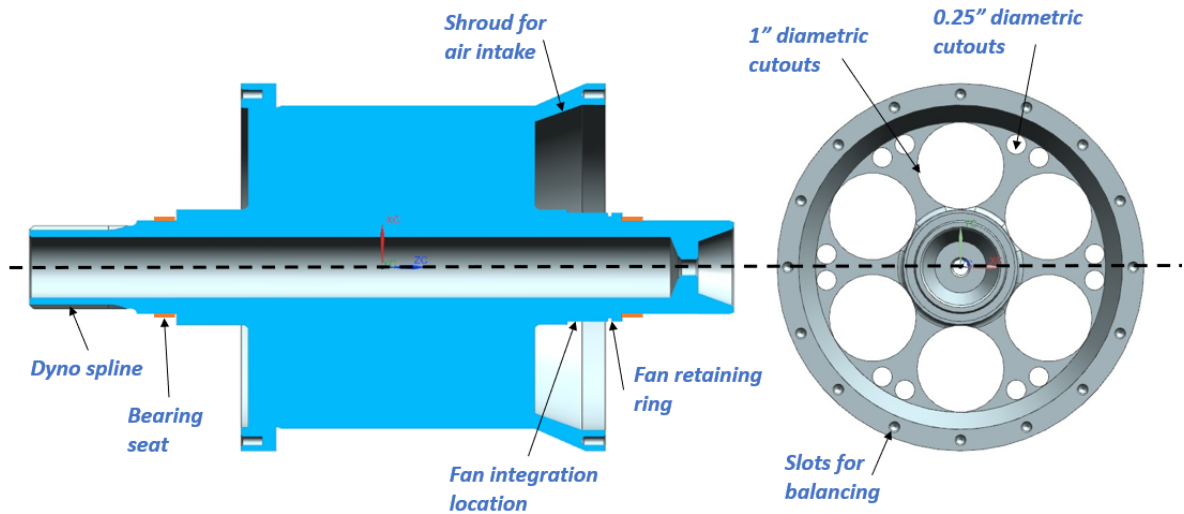


Figure 6.2: Layout of integrated design

6.2 illustrates the integrated design's features that favor structural integrity and thermal performance. The inclusion of diametric cutouts in the design serves three main purposes. Firstly, from a structural engineering perspective, a cylinder followed by a triangular shape offers the strongest support due to the absence of corners. Corners or sharp edges in shapes can lead to stress concentration and higher bending moments. To enhance the efficiency of the air intake, a shroud is being devised around the fan. Smaller vents would result in a lower mass flow rate, leading to ineffective cooling. Finally, a cylindrical hole is the most straightforward to machine, as it can be easily accomplished using a simple drilling process.

Chapter 7

Simulation Framework for Static and Dynamic Analysis

This chapter will provide a comprehensive explanation of the design framework, covering the entire process from the initial design stages to the manufacturing of the final component. The integrated design framework for the rotor assembly is organized into four main sections: CAD design, static analysis, dynamic analysis, and optimization framework. The CAD design framework, as depicted in Figure 7.1, commences by molding the integrated design around the predetermined dimensions of the PMs and rotor backiron length and thickness obtained from the EM simulations. The shaft assembly includes additional components, such as the resolver target, which is press-fitted on a taper shaft and bolted to the main shaft, high-speed bearings with a labyrinth seal, centrifugal fan and its retainer rings. Hybrid bearings, equipped with a robust steel cage and race, incorporate ceramic balls known for their extended grease life, resulting in reduced friction and heat losses, thus prolonging the bearing's operational lifespan [59].

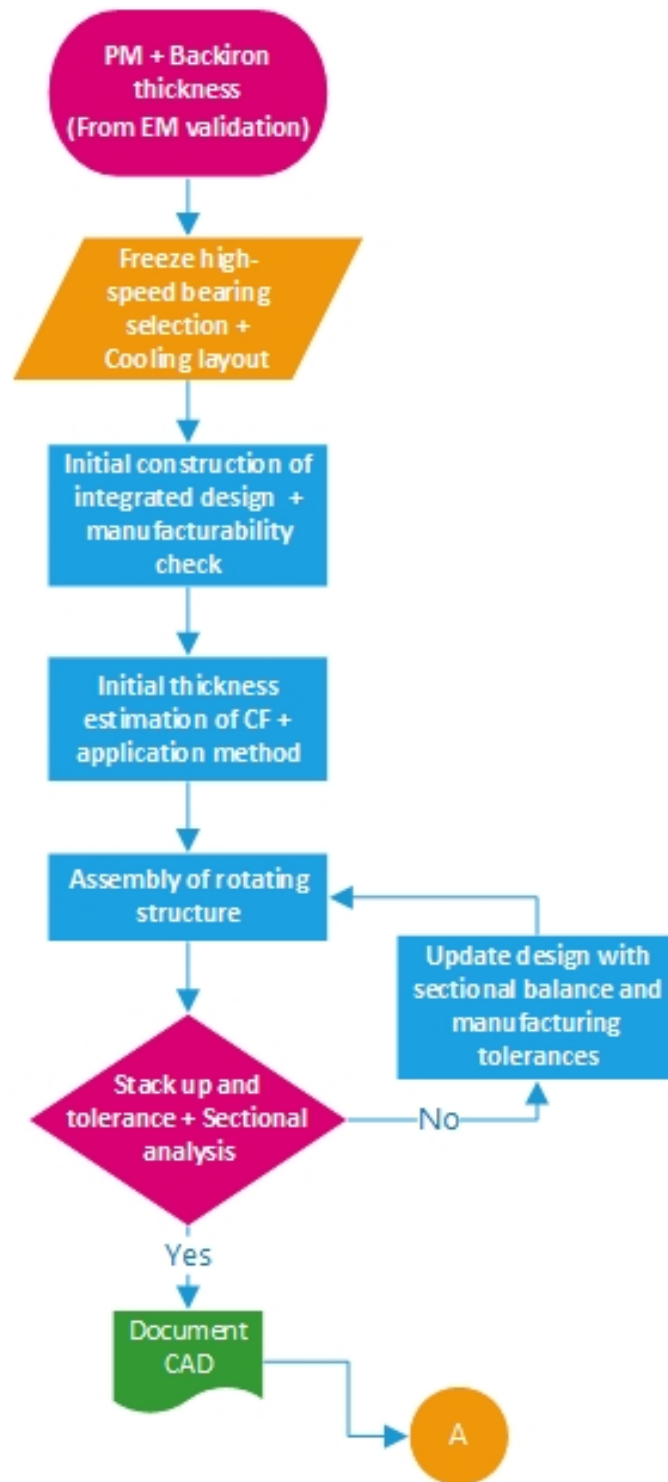


Figure 7.1: Framework for CAD design

After conducting analytical calculations in Section 4.1 and considering various factors such as standard bearing inner and outer diameters, drill sizes, tool features, and support for PMs, the initial design for the integrated assembly is proposed. The peripheral components that will be attached to the integrated shaft are assembled, and the overall dimensional tolerance is assessed for manufacturability. The carbon fiber sleeve is designed with an initial estimated thickness of 1.35mm and is filament-wound around the PMs, with adhesives serving as potting materials during magnet assembly. A base design stage radial stack up analysis is performed and is stored.

Figure 7.2 illustrates the steps involved in static analysis using FEA in Altair Optistruct. The process begins with a mesh sensitivity analysis to determine the appropriate fine mesh size for areas with complex features, thereby avoiding stress concentration. All components are 3D with a second-order tetra mesh, and for the thin carbon fiber sleeve, a composite ply modeling technique is utilized in Hyperlminates software, as explained in Section 8.1.2. After completing the modeling, the different components are integrated using specialized connection elements and contact modeling methods. A thorough check is performed to ensure that all contacts are properly established and structural loading is applied to the model, including SPC constraints through rigids, modeling of boundary condition mount bolts, pretension forces and thermal loads from CFD, and centrifugal (RFORCE) loading. Four loading case scenarios are analyzed to understand the contribution of each loading scenario in case of component failure. In Case 1, temperatures obtained from CFD analysis are applied to conduct a steady-state heat transfer analysis and study its impact. In Case 2, all the interferences applied to the contact are resolved, as interferences are sensitive to structural loading.

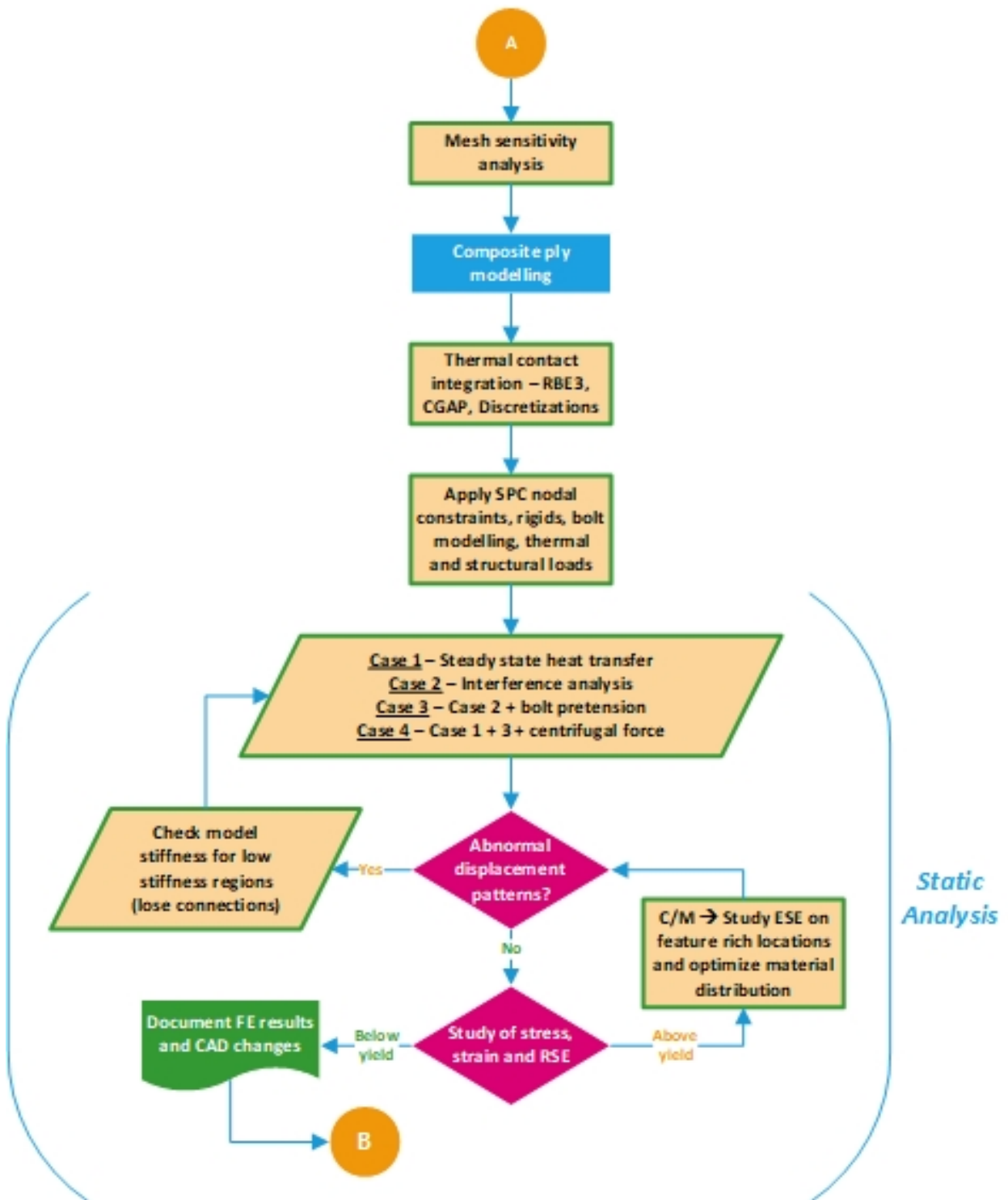


Figure 7.2: Framework for FEA design - Static analysis

Case 3 builds upon the results from Case 2 and incorporates the pretension force on the bearing and mount bolts. Lastly, in Case 4, the outcomes from Case 3 are utilized, and a centrifugal force equivalent to $22,000rpm$ is applied. After the simulation, particular convergence criteria are met, and the outcomes are subsequently examined. Initially, the displacement patterns are analyzed to identify any irrelevant deformations. If any, it could indicate poor contact stiffness. In such cases, countermeasures involve either correcting the contact or establishing a new local contact definition. On the other hand, if displacements appear within normal ranges, the stress, strain, residual strain energy (RSE), compliance, and element strain energy (ESE) are examined. The durability clearance conditions require that the highest von Mises stress be below the yield stress, and the strain should be below the material's % elongation (with a suitable safety factor). The RSE, or epsilon (ϵ) shown in Equation 8.1.1, represents the ratio of work done by the residual force (δP) to work done by the applied force (P), must be as small as possible (generally below $10e^{-9}$). The u^T is the calculated displacement vector in Equation 8.1.1 and k is the stiffness matrix.

$$\epsilon = \frac{u^T \delta P}{u^T P} \quad (7.0.1)$$

$$\delta P = ku - P \quad (7.0.2)$$

To achieve a small ratio, the applied force should significantly surpass the residual forces. If the residual forces are equal to or greater than the applied forces, the system will retain forces even after resolving all external forces, leading to fatigue from increased residual stress.

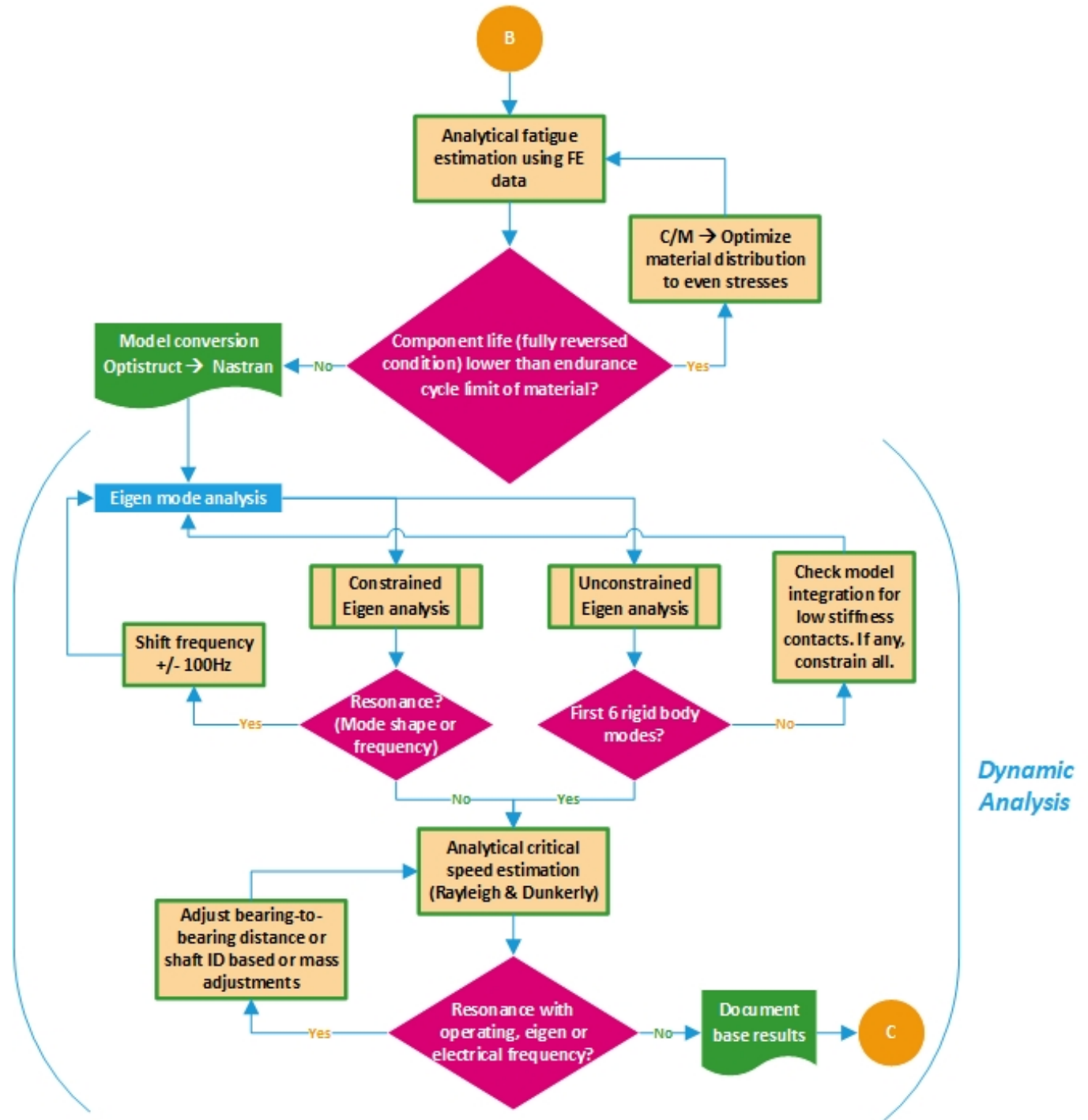


Figure 7.3: Framework for FEA design - Dynamic analysis

The compliance is calculated as the vector product of displacements and forces. It serves as an inverse representation of stiffness, implying that as the displacement increases, the compliance also increases, indicating a lower stiffness in that specific section. The analysis of Element Strain Energies (ESEs) is carried out extensively to identify areas of concentrated strain energy. While high concentrations of strain energy at specific locations may not result in von-Mises stress exceeding the yield strength, they could still cause fatigue when subjected to cyclic loading.

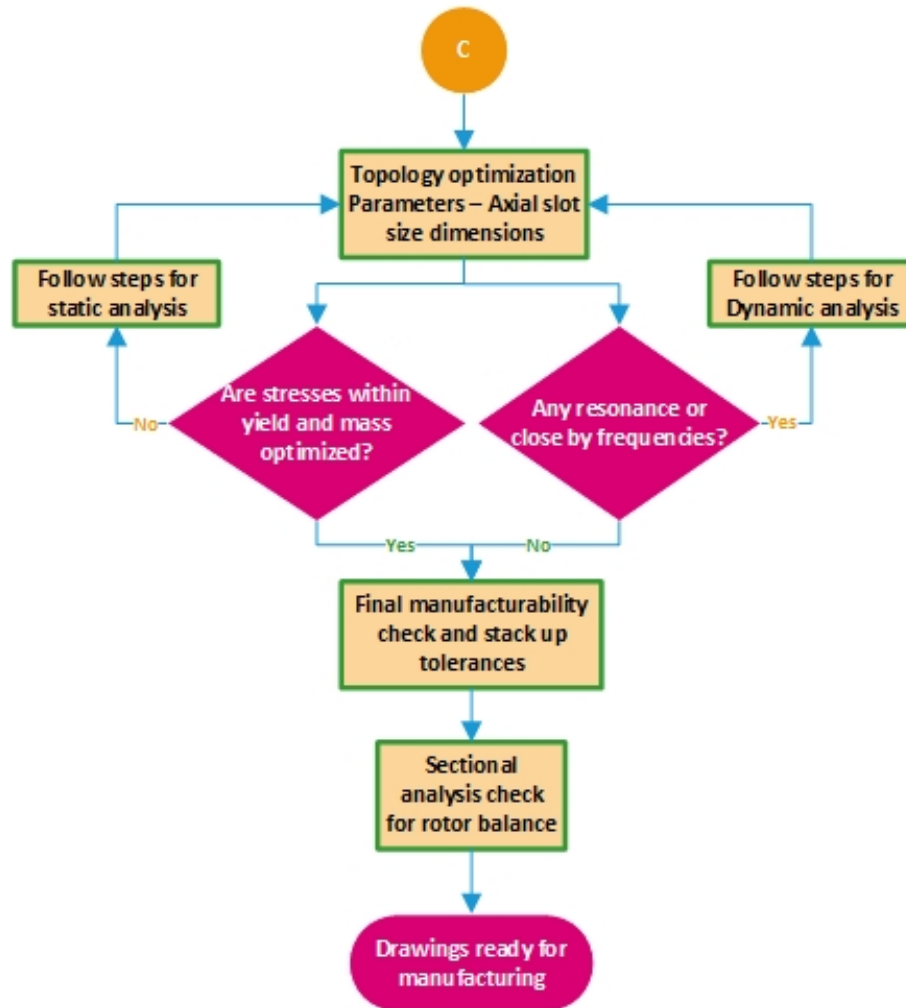


Figure 7.4: Framework for FEA slot optimization

Upon studying these parameters, a suitable decision is made and the corresponding FE data is documented as shown in Figure 7.2. To ensure the component's reliability throughout its operational life cycle, it is essential to validate its dynamic response. The framework for dynamic response is illustrated in Figure 7.3. It begins with the design carried over from the static analysis. The system has four dominant frequencies: the eigen frequency, representing the natural vibration frequency of the assembly; the critical frequency, corresponding to the frequency at which the shaft experiences the highest transverse vibrations; the electrical running frequencies; and the operating frequency. The dynamic analysis involves a thorough examination of these frequencies and the potential for resonance caused by frequency clusters. Subsequently, a frequency array is generated to identify resonant frequencies, and appropriate measures are implemented to mitigate clusters by adjusting frequencies. A more comprehensive discussion of FEA and analytical results will be presented in Chapter 9. The optimization process depicted in Figure 7.4 demonstrates the efforts made to achieve a lightweight rotor assembly. Optimization is essential as it not only aids in reducing weight but also enhances thermal performance by incorporating parametric adjustments to the axial cutouts in the rotor core.

Chapter 8

Static Performance of Integrated Shaft-Hub Design

The precision of FEA results relies on well-executed modeling and integration approaches, considering accurate boundary and loading conditions based on the test bench data. In Figure 6.1, an exploded view of the entire rotating assembly in the FE analysis is depicted. This section encompasses various modeling techniques, such as mesh definition and its impact on the results, contact modeling for press-fit components, effective computation of SS (stress-strain) curves, and multiphysics modeling to simulate different boundary and loading scenarios. Notably, a thermal input is supplied to the rotating system to replicate the conditions of the machine operating at $20,000rpm$. Additionally, this chapter will delve into detailed discussions on the static performance of the integrated design. Various parameters such as displacement, stress, strain, residual strain energy, element strain energy, compliance, and strain vector are thoroughly analyzed in this chapter.

8.1 Finite Element Pre-Processing

The first step in the FEA process is known as finite element preprocessing, during which the geometry and material characteristics of the model are determined and discretized into finite elements. The model must be prepared in several important ways before it can be examined using FEA software (Altair Optistruct). The following tasks are frequently performed during the preprocessing phase:

Geometry correction → During the design process using CAD software like NX Siemens or any other, it is possible to encounter surface imperfections, especially in complex features. If these imperfections go unnoticed and are directly meshed, they can lead to various issues such as sleever elements, free edges, and duplicate elemental surfaces, among others. While for simple components, these problems can be easily addressed in FEA, for intricate geometries like the integrated design with multiple features, detecting such issues with the naked eye can be challenging. Therefore, proper CAD preparation becomes essential to identify and rectify these imperfections before proceeding with the finite element analysis.

Mesh Generation → During the discretization or meshing process, the geometry is broken down into smaller, finite parts. In this step, the intricate geometry is broken down into basic shapes like triangles or quadrilaterals in $2D$ or tetrahedrons or hexahedrons in $3D$. Mesh sensitivity analysis is carried out to determine the proper mesh density for a feature since mesh quality is vital for achieving reliable results. Due to the ply structure and material strength orientation, which is covered in this chapter, composite materials demand specialized modeling.

Material Properties → Based on the materials utilized in the physical system, the finite elements are given material properties, such as Young's modulus, Poisson's

ratio, density, and thermal conductivity. This information is essential since they influence how the structure responds to different loading scenarios.

Contact Definitions → Contact definitions are defined in situations where there are many parts or components in contact with one another to describe how the parts interact and transmit loads. Bolted, transition, and interference fit contacts are examples of defining contacts. Each design calls for a distinct choice of specialized contact process to achieve high levels of convergence.

Loading and boundary conditions → To imitate the restrictions and loading conditions of the real world, boundary and loading conditions are introduced to the model. These circumstances, which include fixed supports, pretension, thermal and centrifugal loads, boundary constraints that restrict intended DOFs, and offset displacements, dictate how the structure interacts with its surroundings. A much more detailed explanation is provided in this chapter.

Solution Parameters → A number of solution parameters are set to regulate the correctness and effectiveness of the analysis, including convergence criteria, time steps, and solver options. In this chapter, a thorough description of how to accelerate solver convergence is presented.

The model is set up for finite element analysis after the preprocessing stage is complete, such that the behavior and response of the structure under various conditions are simulated and analyzed. The study's findings can offer insightful information about the functionality and behavior of the system, assisting in the design and optimization processes.

8.1.1 Stress-Strain Curve Extraction

When extensively optimizing components for mass and topology, it is possible that the components may develop undesirable stress concentration points that exceed the yielding strength of the material due to the extreme centrifugal loading, resulting in a reduction of component life [60]. The design of a component should ensure that it does not surpass the yield strength of the specific material. In the FE simulation, contact non-linearity is considered to establish a realistic contact definition between two press-fit components and to identify potential stress concentration areas. Material non-linearity is also examined to understand how the material behaves in its non-linear range when subjected to higher loads during component optimization. For the scope of this thesis, material non-linearity is not specifically studied since the component does not include any welded joints nor any fatigue-specific simulations being conducted. However, this section will provide valuable insights for those interested in studying non-linear behavior when optimizing components.

While plotting the stress-strain curve, they are of two types, namely the true stress-strain curve and engineering stress-strain curve. The engineering stress-strain curve represents the relationship between stress and strain using the original cross-section and gauge length, whereas the true stress-strain curve represents the relationship using the instantaneous cross-section's area and length [61]. From a practical perspective, utilizing the true stress-strain curve would be more suitable as it accurately represents the real-life situation of higher stress levels corresponding to lower incremental strain. However, this holds primarily for ductile materials experiencing higher loading conditions. In cases where such conditions do not apply, the distinction between using either method would be negligible. The true stress-strain curve is

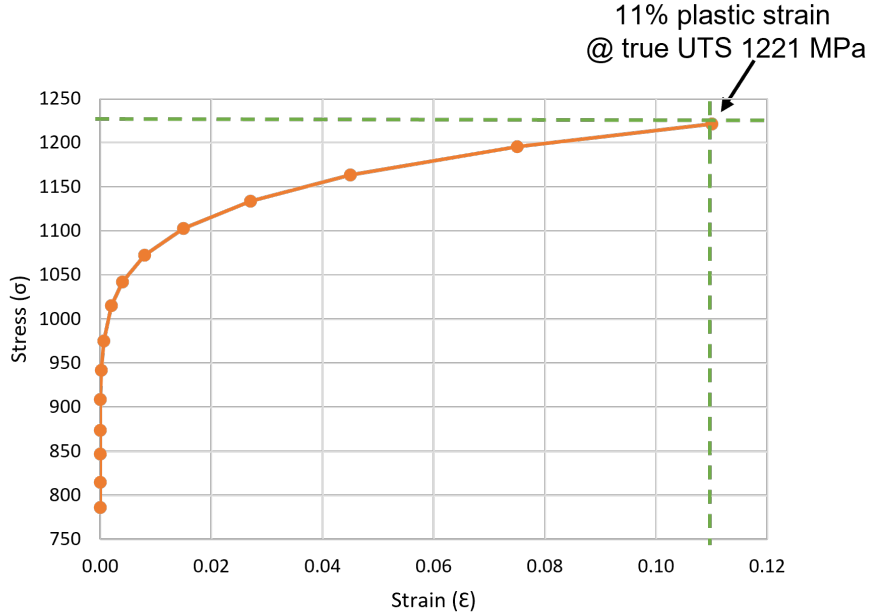


Figure 8.1: True stress-strain curve for AISI 4340 using modified power-law hardening

calculated using modified power-law hardening, which states in Equation 8.1.1 that,

$$\sigma = \sigma_y + k\epsilon^n \quad (8.1.1)$$

In Equation 8.1.1, the first half of the equation equates to the maximum stress (σ) in the elastic region, denoted by the yield strength (σ_y) of the material and the second half of the equation relates to the stresses in the plastic region where the plastic strain (ϵ) is dependent of both strength coefficient (k) and work hardening coefficient (n). The work-hardening coefficient is generally between 0 and 0.5, with a lower work-hardening rate as the material strength increases [60, 62]. For heat-treated AISI 4340, the work hardening exponent is as low as 0.16, denoting lower formability and higher hardness [63]. Figure 8.1 shows the true stress-strain curve

for AISI 4340, and it can be observed that 11% plastic strain is achieved at the ultimate strength of 1221MPa . Henceforth the theoretical plastic strain calculated using the modified power-law hardening is relatively closer to the 13.2% elongation of the material provided by the supplier. A similar result can be obtained using the Romberg-Osgood model [60, 63]. It is to be noticed that the incremental true strain value has a crucial role in accurately capturing the curve as shown in Figure 8.1. The increments for the true strain can either be calculated by keeping a constant difference between the obtained true stress or using Taylor series expansion of Equation 8.1.1 for higher-order terms. A simple interpolation of the first and last values of true stress and strain can also provide intermediate points for a smooth curve.

8.1.2 Finite Element Modelling

Finite element modeling incorporates various modeling techniques and justifications on the usage of $2D$ and $3D$ elements and their types, mesh quality effect on results and assignment of properties and material to FE components are discussed in this section. For the rotor assembly, a second-order tetrahedral $3D$ mesh is used for all the solid components except the washer flange and carbon fiber. The stiffness matrix for a tetrahedral element is higher than hexahedral element [64] due to the shape of a tetrahedral element making it less compressible with a susceptibility of mesh locking. This issue is repressed by increasing the mesh density of tetrahedron elements and implementing a second order but at the cost of higher computational time. Secondly, the hexahedral elements have a poor mesh quality due to the two additional faces resulting in skewness [65] as the elements are though to be modeled at feature-rich locations.

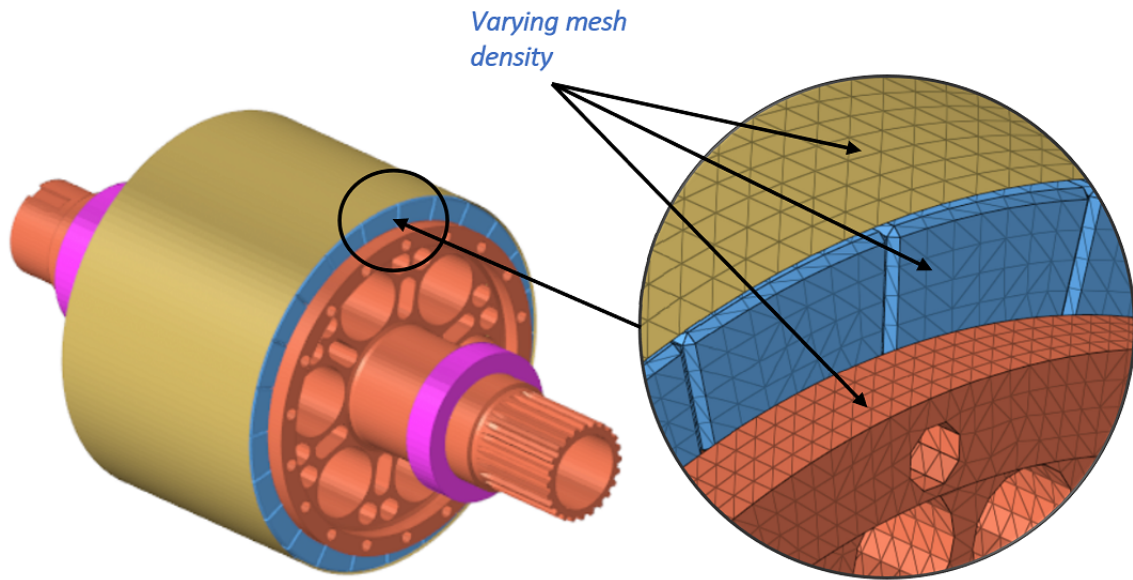


Figure 8.2: A Varying mesh density based on feature and component of study

The force at any given instantaneous node is determined by the product of the displacement and stiffness matrix, which is applied sequentially to each node and is vital for a smooth mesh for better force transition. Second-order 2D shell elements define the washer flange and carbon fiber since they have a relatively less complex shape and uniform thickness of 1.25 and 1.35mm, respectively. The strategy for meshing the integrated design is to create a variable mesh density as shown in Figure 8.2, keeping in mind three scenarios; Scenario 1 is to identify the components of the study, scenario 2 is to conduct mesh sensitivity to rightly capture all features of components for study [66] and scenario 3 is to predetermine master and slave components for a smooth transition of mesh while defining contact conditions [67]. A fine-meshed feature location might not necessarily contribute towards improving the local strains in most cases but is considered vital in studying the strain pattern and stress concentration.

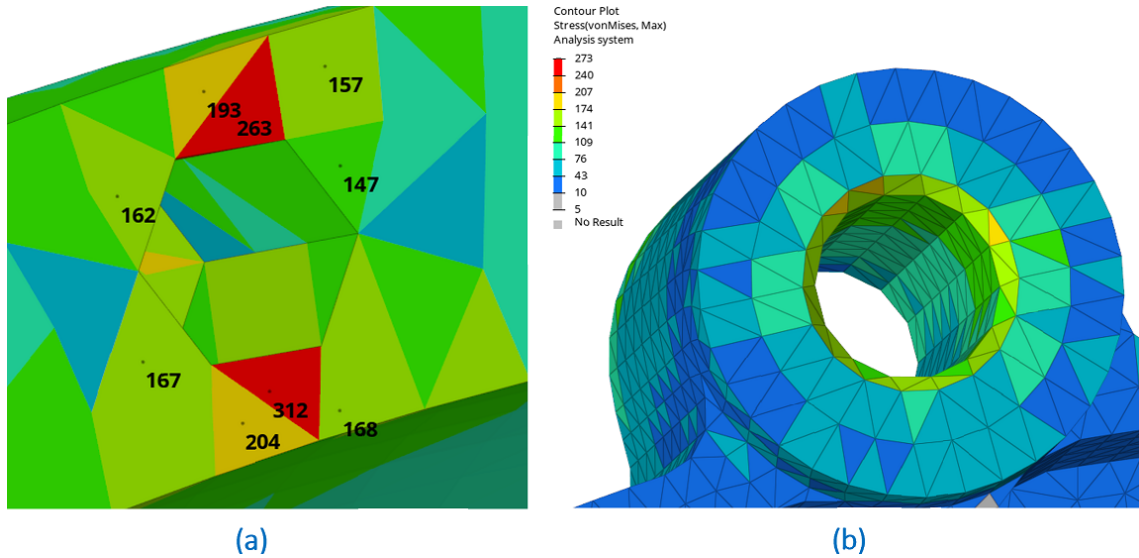


Figure 8.3: (a) Abrupt von-mises stress concentration due to insufficient capture of feature (b) Two rows of washer layers to enhance stress distribution along load/boundary path

Risk Zones	Feature to mesh size ratio	Element type
Low	1.5:1	(Tetrahedron if 3D
Medium	3.5:1	Rtria or Quad if 2D
High	5:1	RBE3 - Loading RBE2 - constraints)

Table 8.1: Suitable mesh size and element type - Mesh sensitivity

Fillet strain can be observed when the fillet features are captured incorrectly, leading to high strain concentration. Sharp corners abruptly increase point stiffness leading to excessive elemental distortion, and one such example is showcased in Figure 8.3. Washer layers promote better distribution of stresses but fractionally increase the computational time as the elements are made finer near load path locations. Table 8.1 shows the apt feature length to mesh ratio size and the corresponding element type that provides a smooth stress transition upon static and dynamic loading. The

carbon fiber is a composite material, and special modelling is applied to define the stresses formed in the material accurately. In FEA, it is possible to define the material nature as either Isotropic, anisotropic, or orthotropic based on the physical property in a measured direction. Carbon fiber is orthotropic since its physical properties vary in all three principal directions. The maximum tensile strength is associated with the longitudinal direction, and the minimum with the transverse direction. In the FE solver (Optistruct, Abaqus, or Nastran), the orthogonal properties for carbon fiber, the tensile and shear modulus, poisson's ratio, and CTE in the two principal vectors are applied. It was noticed that the information relating to either the shear modulus (G) or poisson's ratio (ν), henceforth using Equation 8.1.2, either of the two unknown values can be found.

$$E = 2G(1 + \nu) \tag{8.1.2}$$

The ply thickness of $0.15mm$ completes to 9 layers to obtain an overall thickness of $1.35mm$. The mesh size for the slave surface (carbon fiber composite) is considered finer than the master surface (balancing ring and magnet's top surface), such that the master surface can penetrate the slave surface during contact open/close conditions. Additionally, it is important to consider the ply orientation, whether it is cross-ply or unidirectional, during the design process. Some motor manufacturers opt for bidirectional cross-ply, which offers higher stiffness in both longitudinal and lateral directions, but it comes with increased manufacturing complexity. To streamline the manufacturing process, filament winding with an angle between 80 to 86 degrees is considered during the analysis phase.

8.1.3 Finite Element Integration

Finite element integration involves the seamless joining of two meshed components. This process is essential to simulate real-world scenarios where the components interact through press-fitted connections, bolted connections, thread/washer locks, or touch-based contact conditions. When dealing with press-fitted connections with interference, a contact pair definition is used in FE solvers to establish the contact boundary. To increase convergence rates in the Optistruct solver, several techniques were adopted. The first is the usage of an optimal contact discretization technique. The usage of Node-to-surface (N2S) discretization was preferred over Surface-to-surface (S2S) discretization as shown in Figure 8.4 due to the below mentioned reasons:

- N2S is faster in terms of solving contacts since N2S has contact between one node in the slave surface to one element in the master surface. Whereas for S2S contacts, there is a contact element (CGAP) between one node on the master surface to one node on the slave surface, thereby increasing simulation time for the increased number of CGAP elements, shown in Figure 8.4.

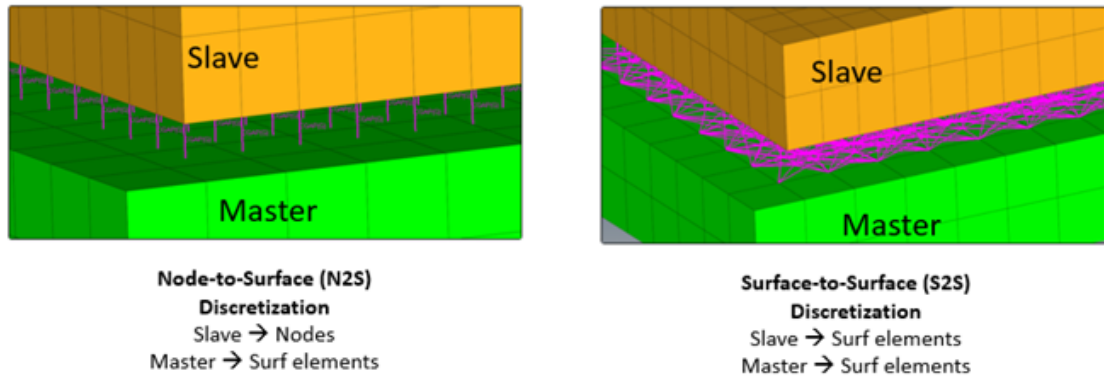


Figure 8.4: N2S and S2S discretization with CGAP elements (purple) [9]

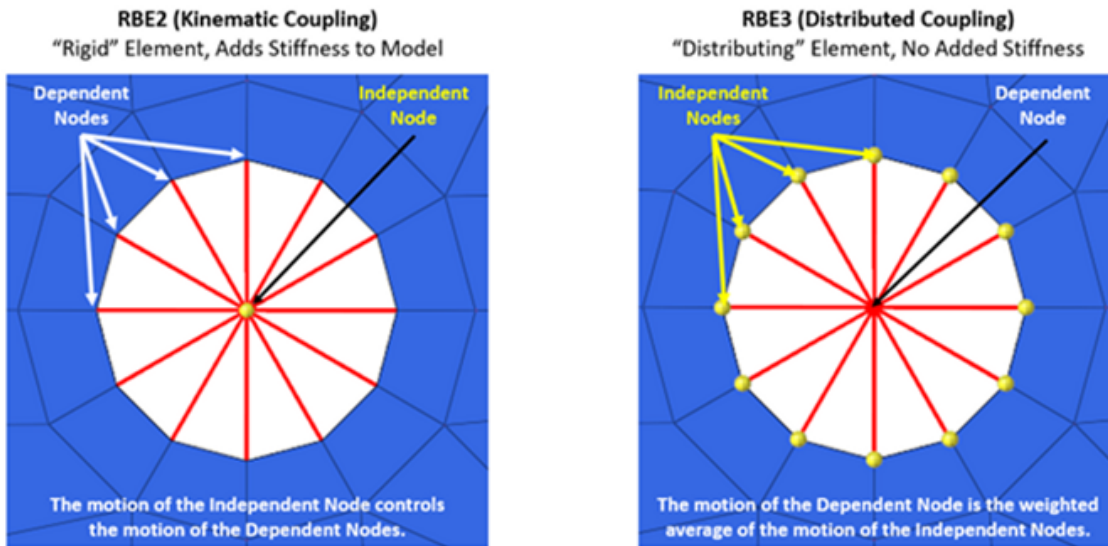


Figure 8.5: RBE2 and RBE3 coupling in Optistruct/Nastran/Abaqus [9]

- In terms of accuracy, S2S discretization has better accuracy than N2S but is only noticeable over a larger surface area of contact such as body panels, etc. Here the overall contact surface area of the carbon fiber sleeve and PMs are considerably small to showcase any noticeable difference in accuracy.
- Majorly, only N2S contacts support thermal contacts as a thermal load is defined for the PMs. Using S2S will detain the modal from performing a multiphysics analysis.

RBE2 and RBE3 are rigid definitions in FEA. RBE2 are high stiff elements that are majorly used for boundary location. Figure 8.5 showcases the RBE2s as having one independent node and the other spider legs are dependent. In simple terms, any loading applied at the independent node will be dispersed equally to all the spider legs. On the other hand, for an RBE3 element, a weighted average is obtained based on the stiffness matrix, which changes per spider leg based on its length from the

central node. In several locations, using an RBE3 element, especially where a force is defined, would be wise to choose as it does not provide any added local stiffness compared to the RBE2 coupling elements. Henceforth for hard contact locations such as Dyno adapter plate mounting, an RBE2 coupling is used for defining constraints.

Thermal contact allows the solver to know that there is heat exchange that is allowed between two surfaces in contact. Henceforth in the analysis, N2S is considered with a thermal contact card known as PCONTHT in Altair Optistruct. Once the N2S discretization type is applied, the solver creates the CGAP elements and assigns the thermal card applied by the user. When there is a displacement between two relative parts due to an applied force, there will be a movement in contact that can either cause the master and slave surfaces to come close or separate (open) themselves from each other.

Another sliding condition is relative to the interference provided. The press fit contacts can be modeled as an interface pressure on either of the contact surfaces or applied as a negative clearance (also known as interference). The solver applies the provided interference to the system by pushing the slave surface outwards to the applied interference value. The only contact interference in the integrated design is between the bearing and shaft, as well as between the bearings and end plate/housing. This specific fit has been suggested by the bearing manufacturers, considering the difference in CTE among the shaft, bearing, and housing materials. The contact between the permanent magnets and carbon fiber sleeve is realized using a slight initial interference fit of $0.01mm$ representing tension of 33 pounds per tow (1 tow = 24,000 strands of carbon fiber) with which the sleeve is filament winded on the permanent magnets. The master and slave surfaces defined are specific to the contact

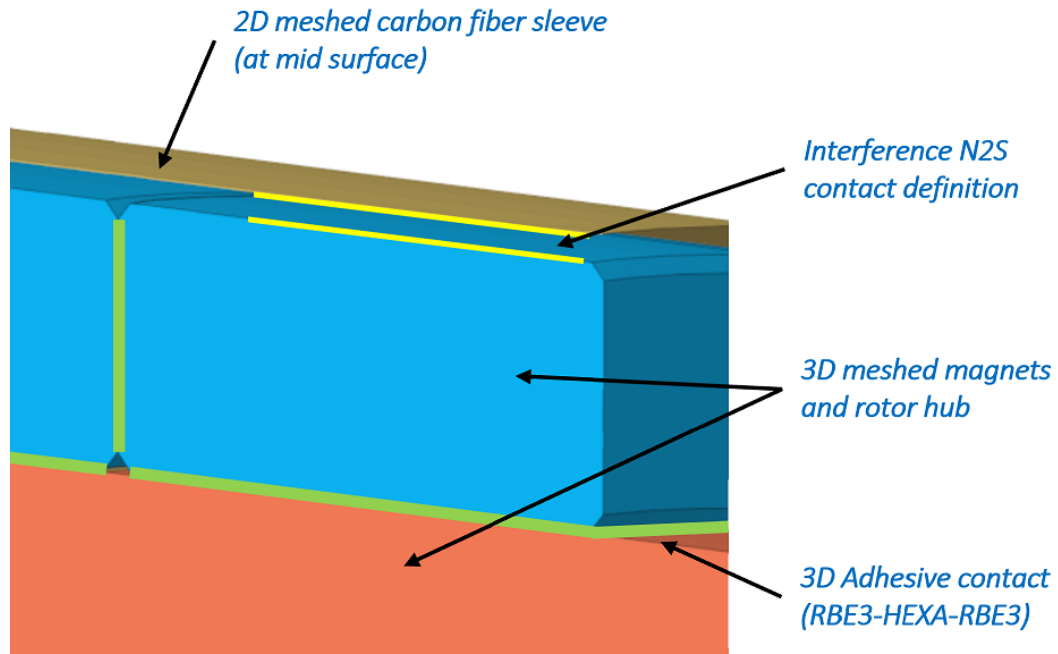


Figure 8.6: Contact definition and adhesive modeling

locations and have a variable mesh density based on the surface type. For the master surface, the mesh is kept coarser, and for the slave surface, the mesh is kept finer. This is because the master surface can penetrate a slave surface and not vice versa. When there are two surfaces, how would one estimate which is master and which is slave surface? The master surface is generally the component that is stiffer or has a larger area than the slave surface. For example, between the interaction of the carbon fiber sleeve and PMs, the carbon fiber sleeve was kept as the master surface, and the PMs the slave surface considering that the CF sleeve is stiffer and slightly larger in area than the PMs.

The term “Adjust” defines the position of the master and slave surface in FEA. For all the simulations, the adjust factor is kept as 0 since the CAD modeling considered for the simulation has a just-touch-based contact in CAD. A tie contact is used

between two components that establish a connection but have almost zero relative displacements with a high degree of stiffness, unlike press-fit contacts, where the stiffness is based upon the corresponding contact pressure obtained from the interference provided. A tie contact is used at mount bolt to casing face and other high torqued areas. The adhesive bond line, which measures $0.1mm$, between the PMs and rotor hub is represented by RBE3-HEXA-RBE3, as depicted in Figure 8.6. The ideal approach for adhesive modeling involves utilizing cohesive zone modeling (CZM), where no RBE3 elements are used, and instead, direct node equivalency is established for the Hexa elements. Under CZM, the hexa elements are assigned specific properties, including traction opening curves that describe the interface opening. The linear-exponential curve over the exponential curve is the most suitable choice for defining simulation time and achieving accurate data representation.

8.1.4 Constrained Boundary and Optimal Loading Conditions

A simulation is considered multiphysics when two different physics are called together to obtain a conjoined result [68]. A complex interdependent analysis setup is considered to obtain the end yield results. Initially, the boundary constraints are set up where the constraints are applied further away from critical low stiff components such as the shaft or end plates. The dyno adapter plate is made of an extremely stiff material and would be the apt location to constrain the assembly, as shown in Figure 8.7(b). Figure 8.7(a) showcases the detailed boundary setup modeling for various stator components. Various aspects of boundary, loading and their combinations towards a multiphysics simulation will be discussed in this section.

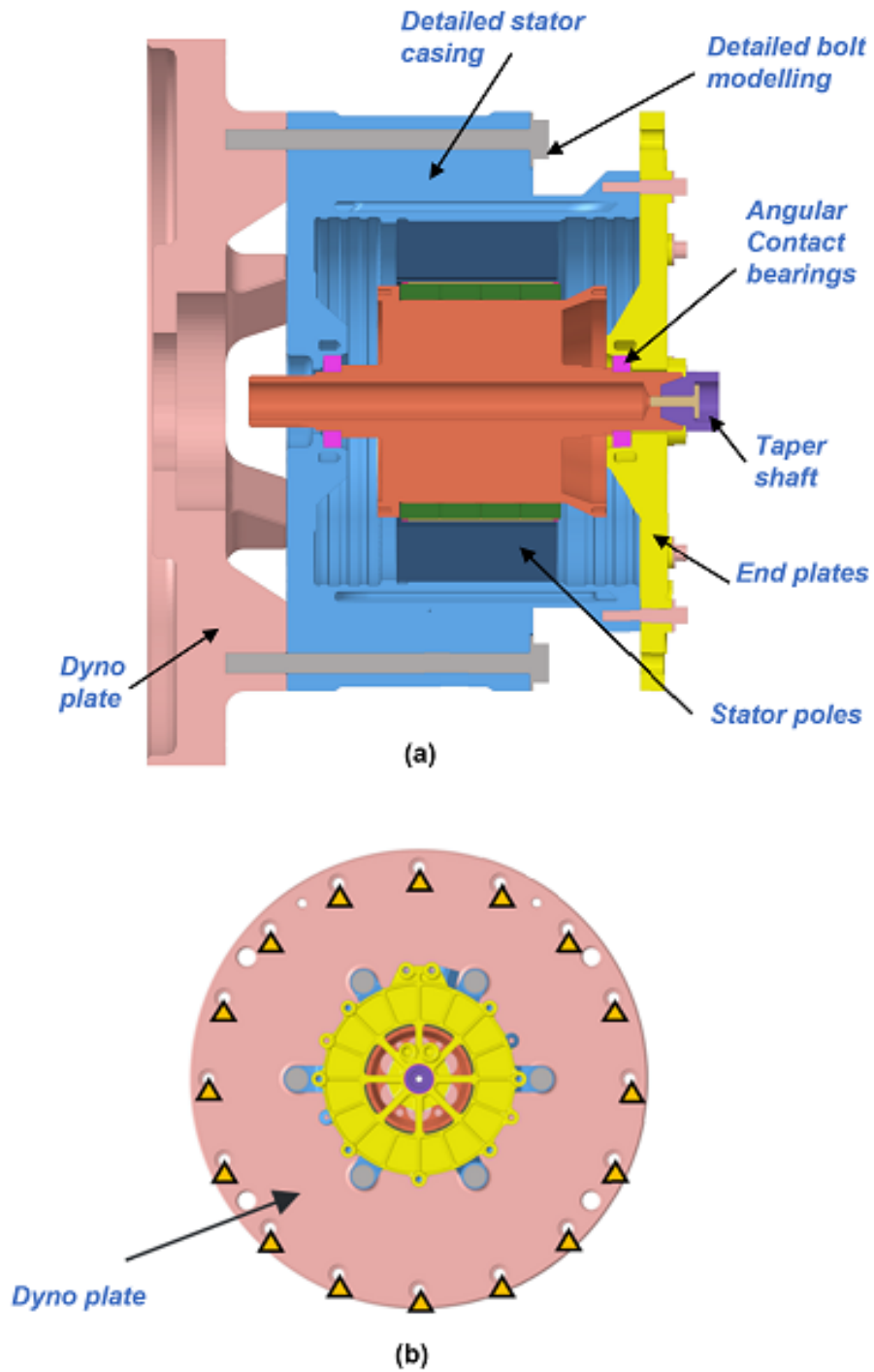


Figure 8.7: (a) Sectional side view of boundary components for integrated design analysis (b) Location of constraints applied on Dyno adapter plate

The constraints are applied to all Degrees of Freedom (DOF), encompassing 3 degrees of translation and 3 degrees of rotation. It was observed that when these constraints were imposed on the shaft/bearing, there was a sharp increase in stress concentration on the shaft/bearing, reaching 1125MPa , far exceeding the material's yield strength. This phenomenon can be attributed to the high stiffness imposed by the constraints (SPC's), which restricts the thermal expansion of the shaft/bearing in either the axial or radial direction, resulting in localized strain when the expansion is limited to a specific magnitude. On the other hand, applying constraints on the dyno adapter plate allows for a lower stiffness path due to the presence of various intermediate components such as end plate, casing, and bearing. This setup permits limited room for expansion of the shaft based on the material properties, effectively reducing the stress to below 600MPa and creating a test-like configuration in FEA.

The system is subjected to two main types of loading, primarily one thermal and two significant structural loadings. The two primary areas where thermal loading occurs in the rotor assembly are the PM and bearing locations. The thermal loading is simulated using grid temperatures obtained from CFD analysis. The CFD simulation revealed a temperature variation ranging from 110°C to 160°C , with the highest temperature observed near the bearing section due to bearing frictional losses. For analysis purposes, an ambient temperature of 80°C is considered, and a corresponding convective heat transfer boundary is defined. The structural loading includes two main components: the axial preload force applied to the angular contact bearing and the pretension force on the casing mount bolts. The axial preload force of 600N is applied to the bearings as recommended by the manufacturer, taking into account factors such as bearing life and contact gap maintenance as the speed increases.

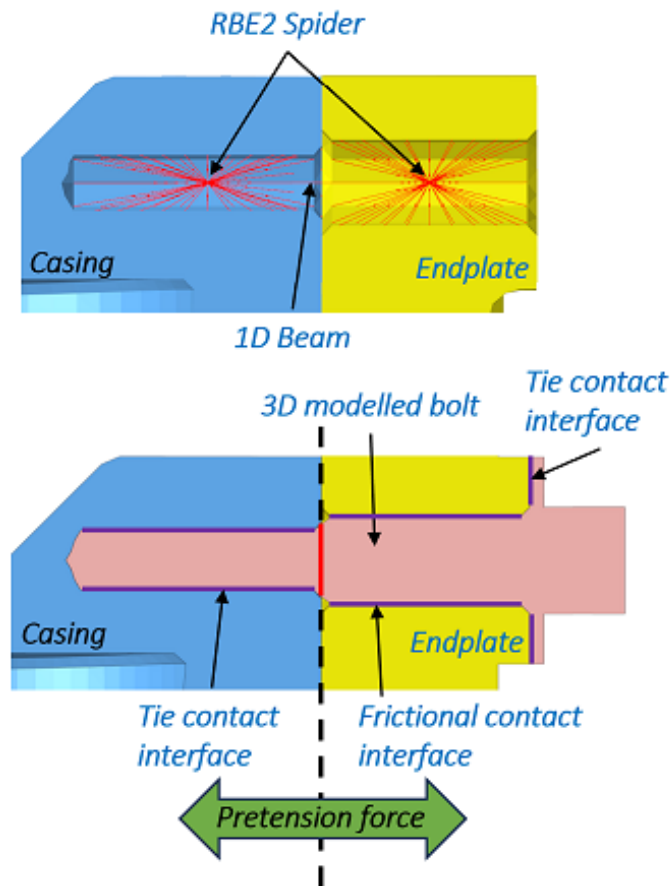


Figure 8.8: Corrected 3D bolt modelling for preload application

The pretension force is a crucial aspect often overlooked, but its significance lies in ensuring the stability and performance of the system. Bolt preload refers to the tensile force generated in a fastener during tightening. The tension created in the bolt during tightening leads to a corresponding compressive force within the bolted joint, commonly known as the clamping force. Figure 8.8 illustrates the placement of the pretension force in the form of a tensile force applied to the bolts. The purpose of this approach is to introduce a tensile force on the bolts, which in turn prestresses them and applies compressive pressure on the stacked surfaces. As per Shingley [45], the bolt preload can be calculated from Equation 8.1.3 and where the preload force

(F_{PL}) is the product of 64% of tensile yield strength (S_Y) and tensile area of bolt (A_T).

$$F_{PL} = 0.64 \cdot S_Y \cdot A_T \quad (8.1.3)$$

The A_T of the bolt can be calculated by using Equation 8.1.4, which states the relation between nominal diameter (d_{nom}) and pitch (P) of the bolt.

$$A_T = \frac{\pi}{4} (d_{nom} - 0.9382P)^2 \quad (8.1.4)$$

After analyzing various scenarios, the preload force obtained for 5/18-inch bolts was $38kN$, considering nearly 60% of the proof load and 25% over torque. To simplify the modeling process and reduce simulation time, RBE2s were used; however, this led to additional high-stiffness regions near the spider leg attachment locations, restricting displacement or rotation of the elements attached to the spider leg. The significant difference in stiffness between the weaker element surrounding the RBE2 resulted in excessive elemental distortion and an increase in stresses by nearly 200%. In one study, a model was analyzed with bolts modeled as RBE2s and 1D beam element, as shown in Figure 8.1.3. Figure 8.1.4 shows the detailed 3D bolt model with a realistic test-like contact setup. Multiple iterations were performed to determine the right contact methodology. The contacts were applied to ensure the bolt head engages with a tied contact with the stator casing, as the applied pretension almost eliminates any relative displacement through friction between the surfaces. The bolt shank contact was split into two parts. The unthreaded portion was set with a contact pair, defining a frictional value between the bolt shank and casing surface, allowing

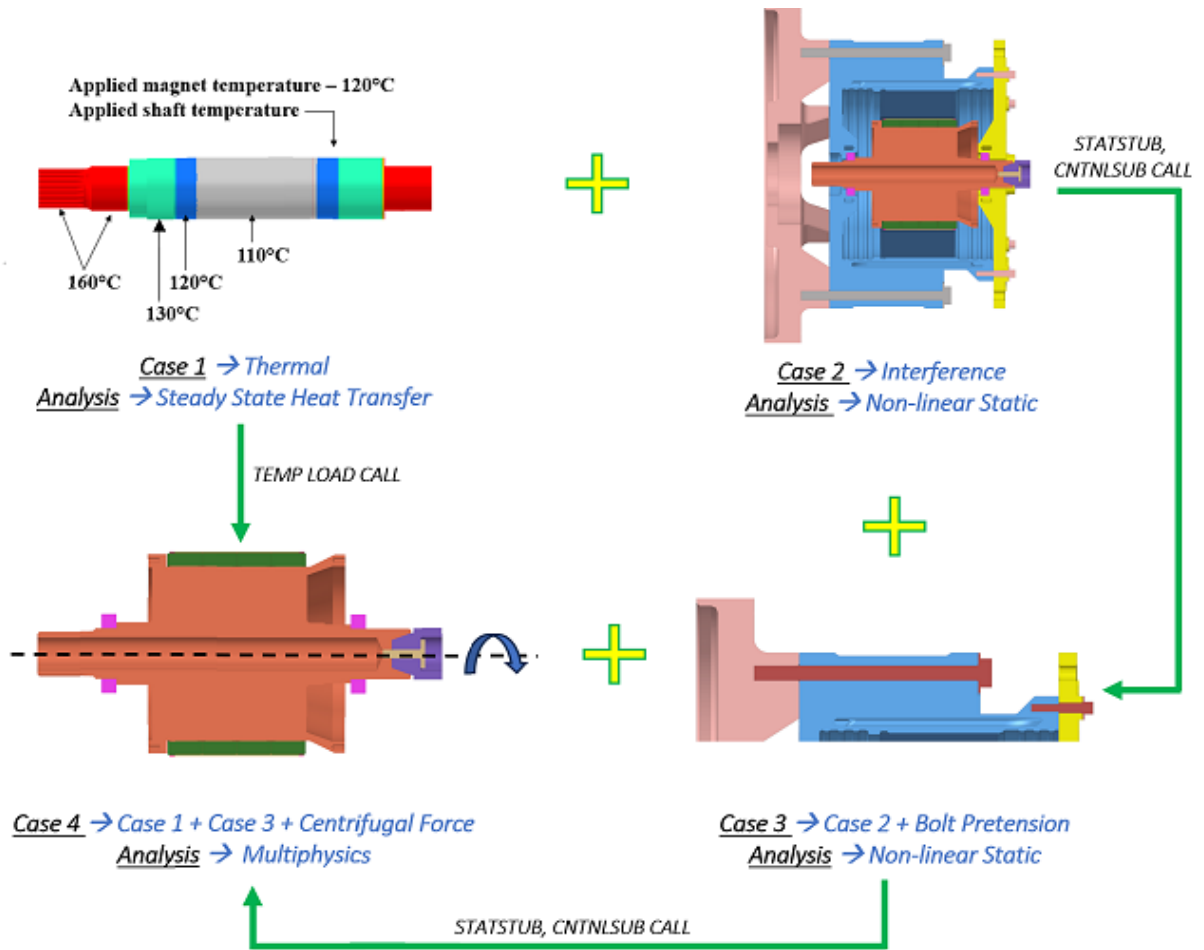


Figure 8.9: A subcase process flow setup for multiphysics simulation

the central shank to expand and contract along the bolt’s axial axis. The threaded section of the bolt had a tied contact with the dyno adapter plate. This setup was considered the most ideal after trying eight different setups in FEA, resulting in proper convergence of the solution and establishing a stress path between the bolt and its interface components.

The multiphysics setup comprises three interconnected subcases, as illustrated in Figure 8.9. In essence, a temperature distribution obtained from CFD analysis is applied to the assembly in Case 1. The resulting grid temperature mapping from

a linear steady-state heat transfer analysis is stored in the result file. In Case 2, a pretension force of $38kN$ is applied to the main bolts on the casing, and $7.5kN$ pretension force is applied to the end plate casing bolts. This enhances the initial stiffness of the model by prestressing the bolted components. As Case 2 involves contacts in the simulation, an iterative non-linear solution is employed. Case 3 is a dependent subcase that relies on the results from Case 2. It starts at the end of Case 2 (using the CNTNLSUB for continuing a subcase and STATSUB for a pretension subcase), incorporating the pretension on the bolts and solving for prestress. In the final Case 4, the case is initiated by extracting the results from Case 3, combining the grid temperature mapping from Case 1 (utilizing the TEMPLOAD card), and applying a centrifugal loading at $22,000rpm$. The max operating condition of the machine is $20,000rpm$, but all components are analyzed at $22,000rpm$ considering the worst-case scenario of over-power ($+2000rpm$). Being an iterative solver, Case 4 applies centrifugal forces based on the convergence rate generally at 10% loading per iteration and further reduced based on the convergence criterion of contact stiffness.

8.2 Finite Element Post-Processing

The main objective of performing FEA is to model and integrate the rotating assembly in a test-like scenario where the maximum von Mises stress in the optimized components is lower than the yield strength of the material (considering safety margins) and reduced displacements to lower shaft vibrations. Von Mises's stress theory is also known as the maximum distortion theory or equivalent stress theory, where the concept states that failure occurs when the distortion strain energy in a material reaches or exceeds the limiting distortion energy (yield point) [69]. Von Mises stress

criterion is specifically used for ductile materials where the yielding of the material leads to plastic deformation. The von Mises stress is theoretically calculated from the principal stress components, as shown in Equation 8.2.1.

$$\sigma_{\text{VM}} = \sqrt{\frac{(\sigma_1 - \sigma_2)^2 + (\sigma_2 - \sigma_3)^2 + (\sigma_3 - \sigma_1)^2}{2}} \quad (8.2.1)$$

However, due to the complexity of the integrated design, analytical calculations are not feasible, and computer simulations are used to predict the von Mises stresses for ductile materials. For brittle materials like composites, where there is no yielding or necking and fracture occurs at ultimate tensile strength, it is more appropriate to use the maximum principal stress theory or Rankine's theory. This theory states that if a brittle material experiences a multiaxial stress system, the fracture will occur at any location where the maximum principal stress exceeds its local strength. The following sections present the results of the most optimized model, including displacement, thermal stress risers, and strain energy densities.

8.2.1 Displacement Pattern

The initial step in checking a finite element analysis involves examining displacement patterns to ensure they are within expected limits. Given the complexity of the model with nearly 48 contact surfaces and 17 groups, there is a chance of human error. Excessive displacements or underconstraint can lead to a drop in stiffness matrix, causing non-convergence in the non-linear solution. This issue may trigger a MAXRATIO error if the displacement matrix exceeds the maximum ratio defined during the simulation setup. Additionally, some displacements might appear partially constrained due to improper contacts, may still achieve convergence but are not ideal.

Division	Integrated design							
	<i>Material</i>	Maximum FE displacement (mm)						
		Axial			Radial (Out)			
		Location	Non drive side	Drive side	Location	Non drive side	Mid	Drive side
Shaft	AISI 4340	Bearing shoulder	0.445 (out)	0.28 (in)	Bearing shoulder	0.025	0.033	0.025
Back iron		Axial end of back iron	0.405 (out)	0.313 (in)	Magnet base on back iron	0.078	0.08	0.085
PM's	NdFeB	Axial end of PMs	0.445 (out)	0.288 (in)	Axial end of PMs	0.127	0.118	0.123

Table 8.2: Axial and radial displacement pattern of integrated design and PMs

After several simulations in improving the design, mesh, contact conditions, and simulation setup, the deformation results for the most optimized design are showcased in Table 8.2. Studying the deformations serves the purpose of understanding the maximum displacement of PMs, which can impact the reduction of the air gap. As shown in Table 8.2, it is evident that the axial displacement is predominantly towards the non-drive side of the machine. The shaft displacement, which measures 0.445mm on the non-drive side bearing shoulder and 0.28mm on the drive side bearing shoulder, both displacing in the same axial direction, which is towards the non-drive side as rightly shown in Figure 8.10. After conducting a root cause analysis, it was revealed that under full load conditions, the combined effect of 36kN pretension force on the casing and a significant centrifugal force of 1.5MN causes displacement towards the weaker side. In this context, the weaker side refers to the side without any constraints, resulting in the assembly expanding axially outwards (away from the dyno plate).

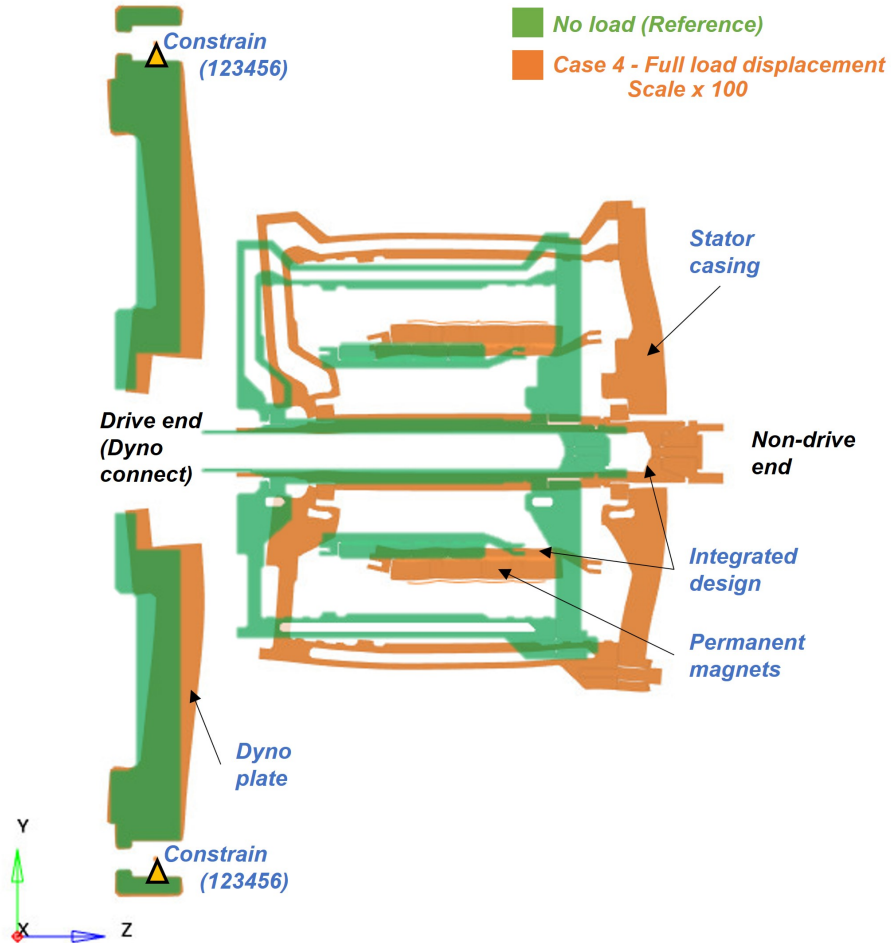


Figure 8.10: Clipped axial displacement of integrated design in both no-load and full-load condition

The radial displacement pattern presented in Table 8.2 for the shaft indicates a slight coning of the shaft at the center, with a central deflection of 0.033mm , which is higher compared to the displacement observed at the bearing shoulder ends of 0.025mm . This outcome aligns logically with the design concept. Additionally, the radial displacement of the back iron is slightly greater on the drive end than on the non-drive end. This difference is attributed to the presence of a notch introduced in the design to improve the axial alignment of PMs during assembly. However, it is

important to note that this effect will not exist during actual testing, as a potting connection will be established between the vertical surface of the back iron and the PMs. The radial displacement of the PMs plays a critical role, along with the carbon fiber sleeve, determines the reduction in the actual air gap. Currently, the physical air gap of the machine measures $2mm$. As observed in Table 8.2, the maximum displacement measures approximately $0.123mm$ on the PMs. This displacement is also reflected in the carbon fiber sleeve since it is wound around the PMs with a low tensional force of 33 pounds per tow. Considering worst-case scenarios, such as rotational speeds of $22,000rpm$ and a conductive heat transfer of $120^{\circ}C$ directly from the PMs without considering cooling effects from the air gap, an overall radial displacement of $0.123mm$ is considered acceptable to achieve stable performance.

8.2.2 Thermal Stress Risers

The mechanical stresses that arise in a motor's parts due to fluctuations in temperature are referred to as thermal stress in motor design. Due to the flow of electric current and other losses, a motor produces heat when it operates. The stator, rotor, bearings, and motor housing could experience a higher temperature. The materials used to build the motor have various coefficients of thermal expansion, which implies that when exposed to temperature changes, they expand or contract at various rates. Thermal expansion and contraction can occur in the components of the motor as it heats up during use and when it cools down after operation. Internal stresses in the material can arise from the thermal expansion and contraction of the motor's parts. The parts of the motor may deform or warp due to these thermal stresses, which could eventually impact the motor's performance, effectiveness, and dependability [70].

Components		Material	Target (MPa)	Static loading {Multiphysics Sim- Case 4} (MPa)	
Integrated design	Shaft	AISI 4340	YS-780 SS-350	Von mises	302
				Max shear	172
	Back iron			Von mises	371
				Max shear	206
PMs		NdFeB	CS-900 FS-250	Von mises	419
Carbon fiber sleeve		Hextow IM7	TS-2100	Max Hoop stress	748

Table 8.3: Summary of thermal stress in the integrated design

The table presented as Table 8.3 displays the von Mises stress values for the highly optimized integrated design. These values were acquired through multiple simulations aimed at achieving convergence by enhancing mesh quality, optimizing contact conditions, and making various geometry improvements to keep stresses well below the yield strength of the material. A more in-depth study supported by FEA snippets will be showcased in this section. The integrated design is divided into three distinct sections to facilitate the study. Section 1 comprises the shaft, Section 2 encompasses the back iron, and Section 3 includes the connecting ribs between the shaft and back iron. The shaft section is subjected to comprehensive analysis due to its critical role in withstanding stresses and requiring in-depth studies. On the other hand, the rib section is of secondary importance as it connects the back iron base to the shaft. The rigidity of the rib section determines the deflection of the overall component.

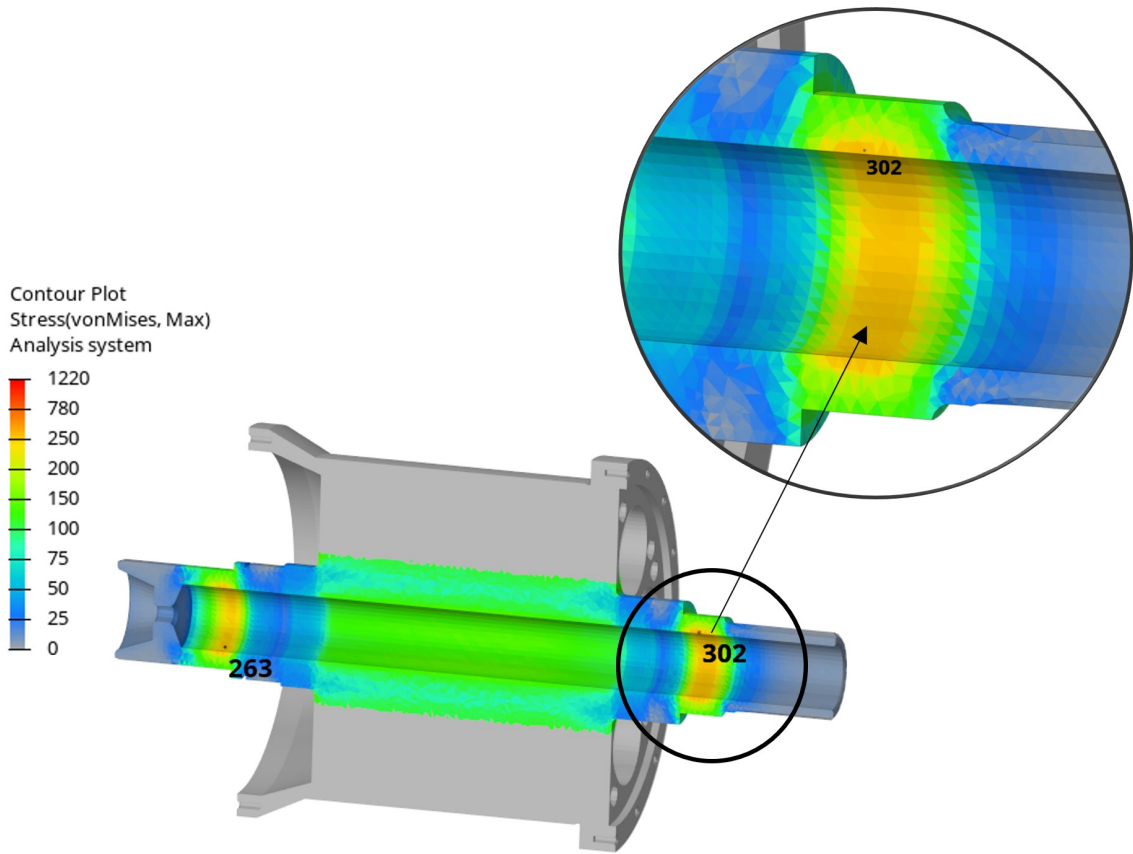


Figure 8.11: Sectional view of maximum stress in bearing base region of the integrated design

The shaft section of the integrated design contains various turned features and serves as the primary pathway for transmitting constraints. Table 8.3 presents the maximum shaft stress, which reaches 302MPa , while the material's yield strength is 780MPa . Figure 8.11 illustrates that the highest stress occurs at the bearing base location. This can be attributed to the combination of compressive stresses arising from interference between the bearing and shaft, along with constraints originating from the dyno plate leading to increased thermal stress. Figure 8.12 confirms the earlier statement, displaying the maximum strain observed at the bearing base location of the shaft. Within the elastic limit, stress is directly proportional to strain, meaning

that any increase in stress leads to a corresponding increase in strain. Nonetheless, analyzing strain provides benefits since it relates to displacement. The strain tensors present strain vectors that offer insights into how the load application impacts the system (strain concentration), how strain dissipates within the material, and the neighboring components the strain could influence.

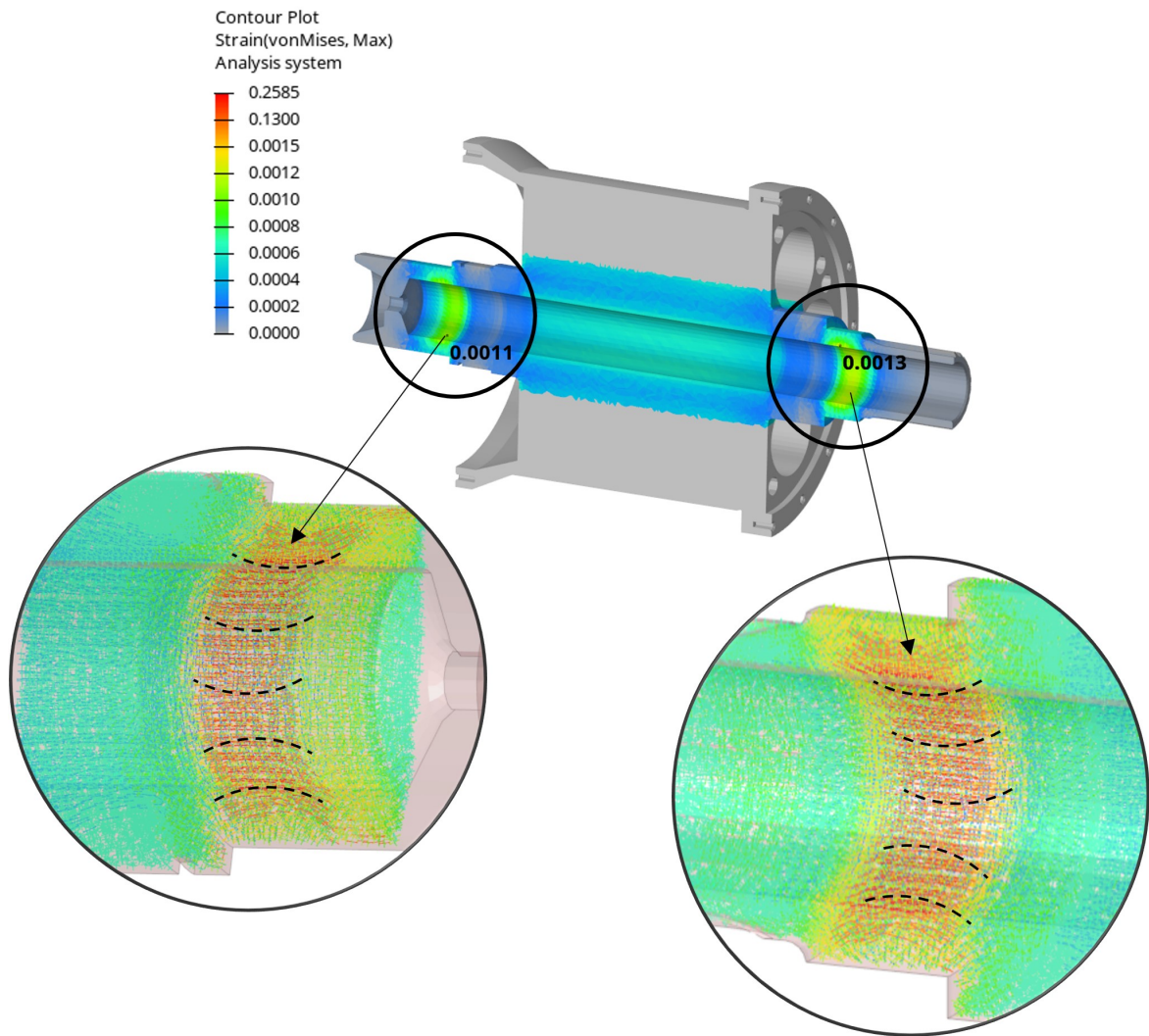


Figure 8.12: Sectional view of maximum strain and strain tensor in bearing base region of the integrated design

In Figure 8.11, it is evident that the stresses are uneven, with the drive side experiencing $49MPa$ more von Mises stress compared to the non-drive end. A similar increase in drive side strain is also observed in Figure 8.12. The strain vectors exhibit significant clustering on the drive side, indicating a higher strain flow path, which corresponds to more localized bending deformation. This behavior is influenced by the arrangement of constraints, which are intentionally kept similar to the test setup. Since the stresses are way lesser than the yield strength of the material, further optimization of the geometry is not considered.

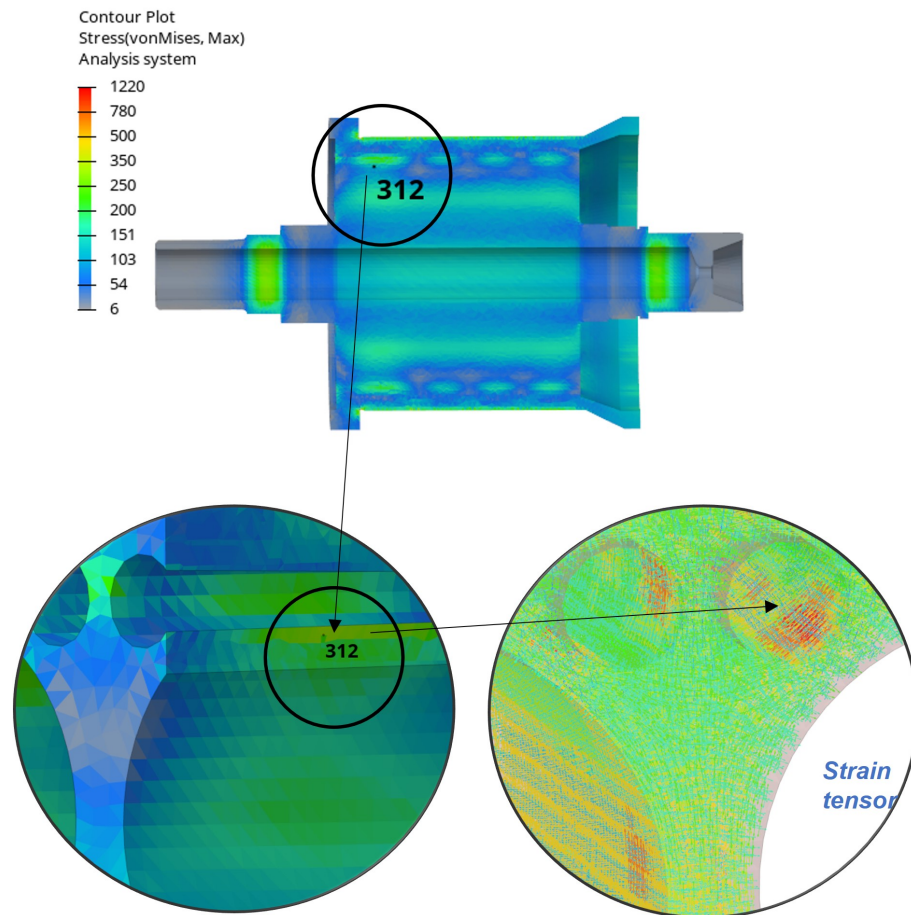


Figure 8.13: Sectional view of maximum strain and strain tensor in bearing base region of the integrated design

The rib section, the second crucial component of the integrated design, is pivotal in connecting the back iron with the shaft. The performance of the entire integrated design heavily relies on the stiffness of the rib section, as it serves as a stress bridge between these two mediums. The Figure 8.13 the maximum stress near the rib region is observed as $312MPa$ with a stress concentration factor of 1.91 considering an area of $46mm^2$. This stress concentration is even across the $2.5mm$ rib thickness and the strain tensors showcase a local compressive strain on the drive side due to the constraints. This is evident in Figure 8.13, where the stresses are higher on the left-hand side of the image (drive side) than the non-drive side due to the location of constraints and, thereby, a high stiffness region. These rib stresses were confirmed to be nominal as the max von Mises stress is lesser than the yield strength of the material.

The PMs, constituting approximately 60% of the mass of the integrated design, play a crucial role in generating a significant centrifugal force. This force is highly influenced by the magnet's distance from the axis of rotation, apart from mass and rotational speed. Placing the magnets farther away from the axis increases the centrifugal force. The PMs are composed of NdFeB material, which possesses a high compressive strength ($900MPa$) due to sintering, while its tensile strength is relatively weaker due to anisotropy. However, within the rotor assembly, the magnets are mainly subjected to compressive stresses arising from factors such as the centrifugal force, thermal expansion of the shaft, and the centripetal force exerted by the carbon fiber sleeve. The segmentation allows for expansion and stress propagation, preventing the PMs from acting as stress-bearing elements within the rotor assembly. A snippet of the tensor plot in the major principal axis is showcased in Figure 8.14.

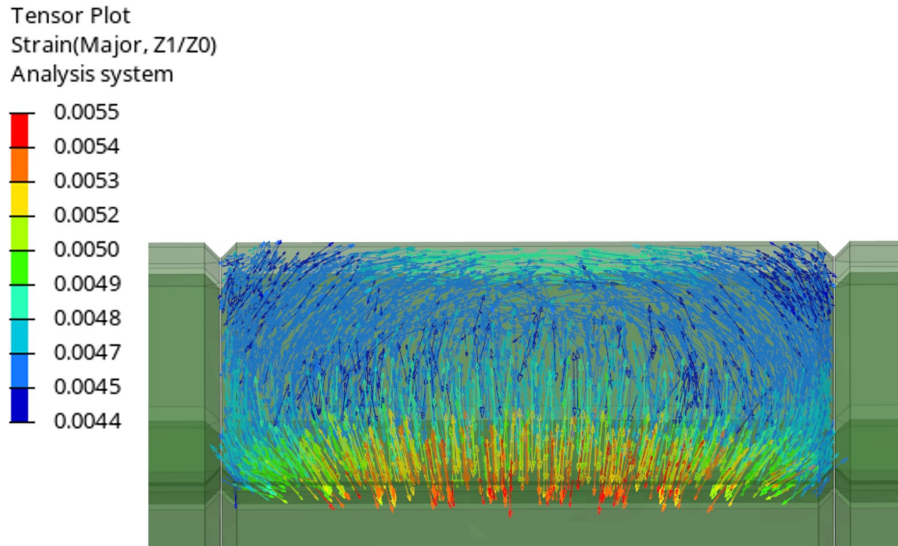


Figure 8.14: Strain tensor in major principal (normal) axis of a single PM

The interplay of strain tensors along the major and minor principal axes results in a combination of radial and axial strains. The radial strain is caused by the compressive force exerted on the PMs by the back iron and carbon fiber sleeves, causing them to contract. Simultaneously, the axial strain occurs as the material expands in the axial direction, leading to strain patterns swirling around the sides of the magnet, as illustrated in Figure 8.14. Upon further examination of the simulation, the outcomes reveal a maximum von mises stress of 415MPa . Analyzing the strain vectors, it becomes evident that a significant portion of the strains is compressive in nature. As a result, the stress direction can be associated with the radial direction, ensuring the magnet experiences a safe peak compressive stress.

The analysis of the carbon fiber sleeve posed a challenge due to its orthotropic nature, requiring a complex modeling approach. The material properties were applied to a $2D$ shell with ply thickness and their count determining the overall thickness of the carbon fiber sleeve. Additionally, a cylindrical coordinate system was employed

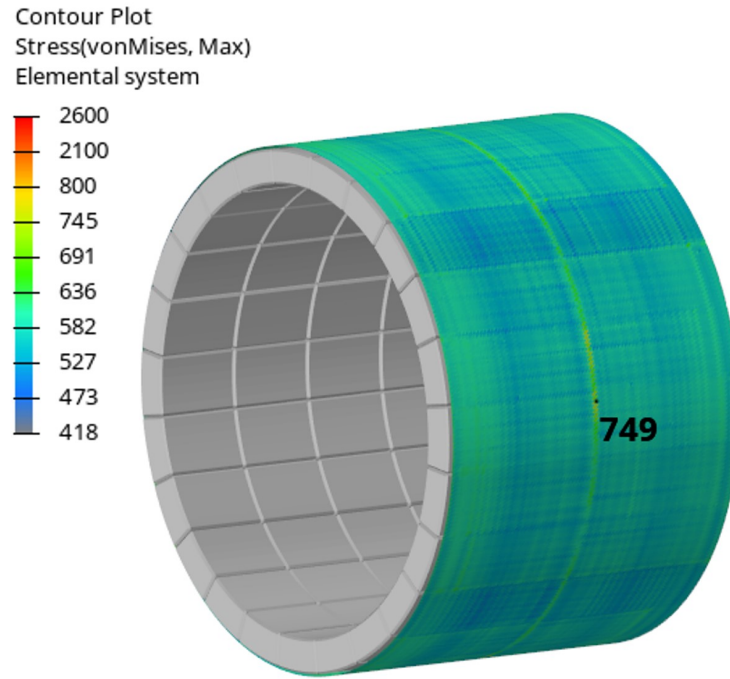


Figure 8.15: Max hoop stress on Carbon fiber sleeve

instead of the conventional Cartesian rectangular coordinate system, as the carbon fiber is treated as a thin-walled cylinder, enabling the calculation of hoop stress. In the non-linear solver, the maximum hoop stress is determined by considering the cylindrical coordinates and calculating the von mises stress. The maximum hoop stress in the carbon fiber sleeve is determined as 748MPa . Figure 8.15 illustrates the stress distribution in the carbon fiber sleeve, particularly at the locations where the PMs are segmented. However, it is essential to note that in real test conditions, the PMs will be potted with adhesive material, resulting in a smoother surface for the carbon fiber wrap. By excluding the segmented high-stress locations in the carbon fiber, the maximum hoop stress reduces to 625MPa , henceforth exhibiting no signs of fatigue or stress concentration.

8.2.3 Optimization of Integrated Design

The main objective of optimizing the rotor hub was to reduce its mass by removing excess material while ensuring that stress concentrations remained within the material's yield limits. This thesis primarily focused on optimizing the cutouts of the integrated design to improve stiffness and reduce mass while ensuring that the stresses remained within the material's yield and tensile strength.

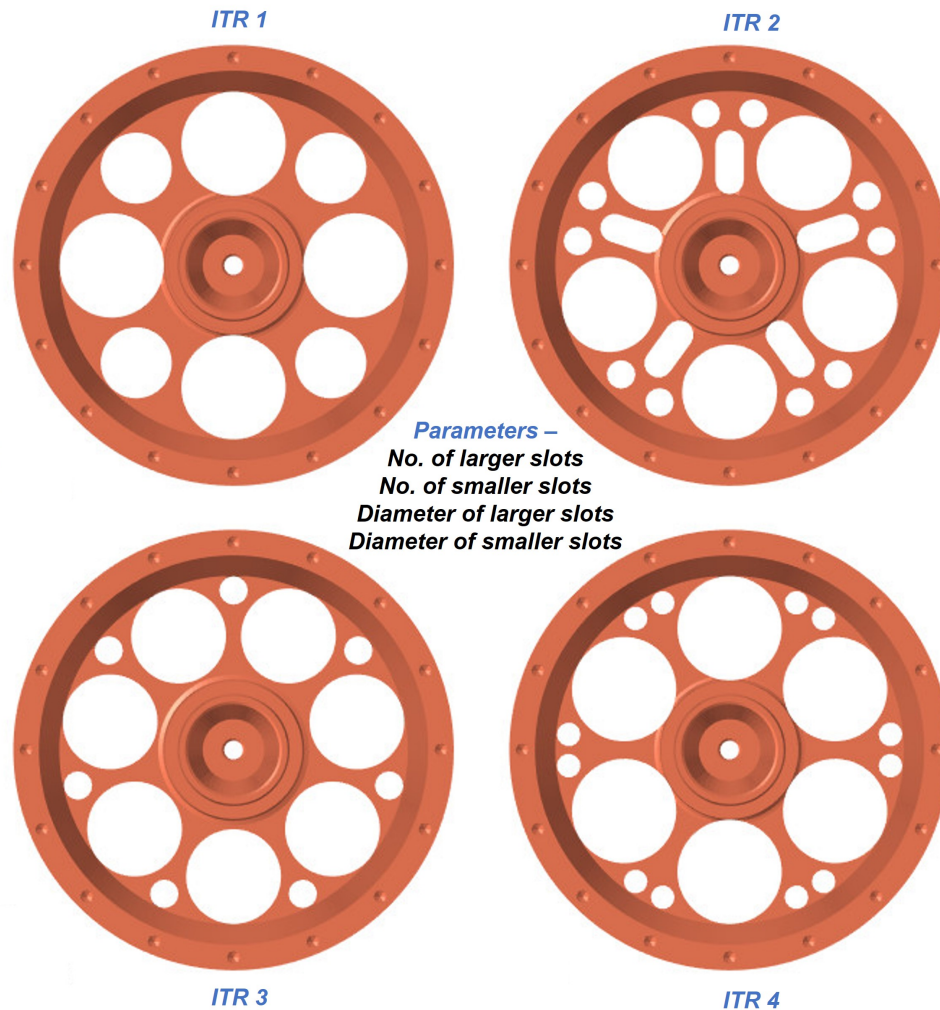


Figure 8.16: 4 of the best chosen parametric optimization of slots for the integrated design

Components		Mat	Target (MPa)	Max Von Mises stress {Multiphysics sim-Case 4} (MPa)			
				<i>ITR1</i> <i>4.3kg</i>	<i>ITR2</i> <i>4.31kg</i>	<i>ITR3</i> <i>4.16kg</i>	<i>ITR4</i> <i>4kg</i>
Integrated Design	Shaft	AISI 4340	YS-780	309	300	306	302
	Back iron			376	384	377	370
PMs		NdFeB	CS-900 FS-250	411	409	414	423
Carbon fiber sleeve		Hextow IM7	TS-2100	739	738	745	748

Table 8.4: Summary of thermal stress in the optimized integrated designs

Four different models (ITR1 to ITR4) with varying parameters for the slots were selected, taking manufacturability and cooling efficiency into consideration as shown in Figure 8.16. ITR1 was designed to explore the concept of increasing the mass flow rate by incorporating larger diametric cutouts. On the other hand, ITR2 focused on optimizing the slot configuration by reducing the size of the larger diameters from 1.1” to 1”, thus creating room for two smaller holes and milled slots. Although both ITR1 and ITR2 weigh the same, ITR2 has a higher manufacturing cost and longer lead time due to its more intricate design. ITR3 is characterized by a mass-optimized design featuring 1” diametric holes along with smaller holes to eliminate excess material from the center. On the other hand, ITR4 represents the final model with a greater number of smaller holes, effectively removing a significant portion of material from the center. The simulation results are presented in Table 8.4, showing a total reduction of 300g without compromising the max von mises stress levels.

8.3 Analytical Fatigue Estimation of AISI 4340

Predicting fatigue failure is of utmost importance in the analysis of real-world engineering structures, as it is a prevalent technical issue and a common cause of failure in metallic structures. Researchers consider two critical factors in this context. The first factor pertains to the material's fatigue resistance, while the second focuses on the stress distribution within the structure. To describe the fatigue behavior of a material, S-N curves are generated based on fatigue tests conducted on standard specimens. On the other hand, FE methods are employed to calculate the stress field distribution [71]. Common materials like various steel and aluminum alloys can be found in the MMPDS-05 [72]. However, in the present motor design, materials used for the carbon fiber sleeve and PMs lack a tested endurance limit value. Henceforth analytical fatigue calculation could only be performed for AISI4340 steel.

Fatigue life calculations are typically performed when the stresses obtained from FEA are close to the yield strength of the material. Each S-N curve for a material characterizes High Cycle Fatigue (HCF) and Low Cycle Fatigue (LCF) behaviors. HCF is particularly interesting in the study, as it deals with elastic deformations, while LCF involves plastic deformations, as shown in Figure 8.17. Electric motors commonly experience HCF, as repetitive rotational cycles occur at lower constant stress amplitudes within the elastic deformation range. To mitigate the risk of HCF failure, several measures can be taken, including using materials with high fatigue strength and resistance, implementing surface treatments, improving microstructure and homogeneity, and controlling the load range and frequency.

In some cases, specific regions with high-stress concentrations may exhibit relatively higher stress risers compared to the surrounding areas. Although the stress

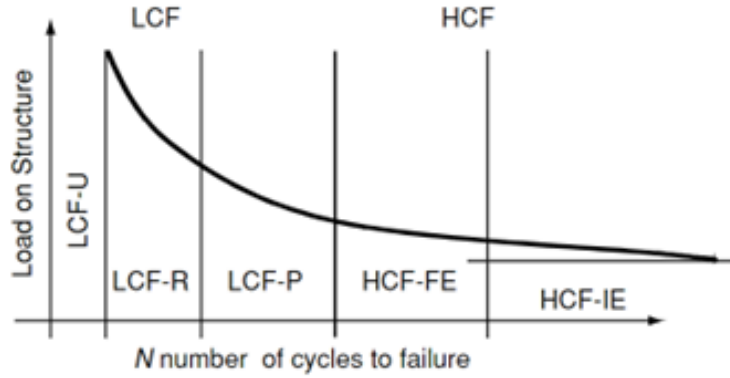


Figure 8.17: Wohler curve denoting HCF and LCF with ascending loads [10]

riser may be below the yield strength, cyclic loading can lead to further concentration of stresses in that area, potentially initiating micro cracks. It is crucial to thoroughly examine all locations with high-stress concentrations in the FEA and conduct analytical calculations based on various sources mentioned in this section to ensure structural integrity. One such area is identified and shown in Figure 8.18. The bearing base location in the integrated design shows a very high-stress concentration and an analytical fatigue assessment is required.

According to Shigley’s design textbook [45], the theoretical endurance limit of a material is influenced by various reduction factors such as surface finish RF_{SF} , size RF_{size} , loading RF_{load} , temperature RF_{temp} and reliability $RF_{reliability}$ factors. The total reduction factor RF_{total} is the product of all reduction factors calculated as shown in Equation 8.3.1.

$$RF_{total} = RF_{SF} \times RF_{size} \times RF_{load} \times RF_{temp} \times RF_{reliability} \quad (8.3.1)$$

$$RF_{SF} = SF_{(factorA)} \times F_{TS}^{(exponentB)} = 0.686 \quad (8.3.2)$$

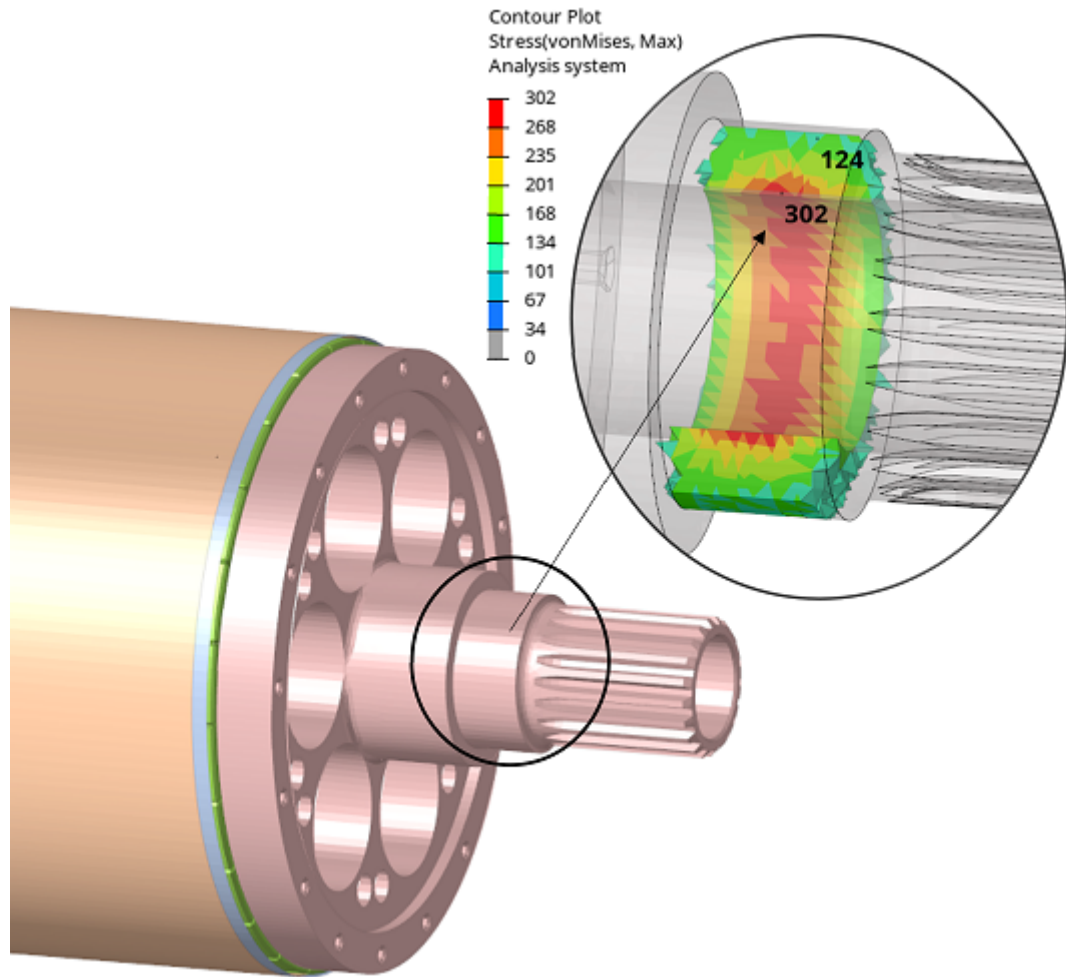


Figure 8.18: Possible location of HCF in integrated design on bearing base

$$RF_{\text{size}} = 1.51 \times D^{-0.157} = 0.864 \quad (8.3.3)$$

For bending loads the RF_{load} is considered as 1 and the RF_{temp} for the material at 150°C is 1.025. The $RF_{\text{reliability}}$ for 90% is considered as 0.897; thereby, the RF_{SF} is calculated to be 0.545. The modified endurance limit EL_{mod} is calculated to be the product of EL_{supplier} which is $570\text{MPa}@1^6$ cycles and the RF_{SF} , showcased in

Equation 8.3.4.

$$EL_{\text{mod}} = EL_{\text{supplier}} \times RF_{\text{total}} = 310.63 \text{MPa}@1^6 \text{cycles} \quad (8.3.4)$$

The analytical calculation for the fatigue life cycle is derived based on maximum and minimum stress from FEA. A fully reversed operational cycle is considered as the motor experiences an alternating loading during functioning. It is to be considered that the minimum stress from FEA is to be recorded either from the opposite region of the maximum stress in terms of bolt locations or the adjacent region in terms of complex feature plane. Upon tabulating the minimum (σ_{FEmin}) and maximum stress (σ_{FEmax}) from 8.18, mean stress (σ_{mean}) and alternate stress ($\sigma_{alternate}$) is calculated as shown in Equation 8.3.5 and 8.3.6.

$$\sigma_{\text{mean}} = \frac{\sigma_{FE_{\text{max}}} + \sigma_{FE_{\text{min}}}}{2} = 213 \text{MPa} \quad (8.3.5)$$

$$\sigma_{\text{alternate}} = \frac{\sigma_{FE_{\text{max}}} - \sigma_{FE_{\text{min}}}}{2} = 89 \text{MPa} \quad (8.3.6)$$

For brittle materials, the true fracture stress is very close to the ultimate tensile strength, and in this condition, the Goodman's line equation will prove beneficial. Whereas for ductile materials, the true fracture stress is far greater than the ultimate tensile strength, Gerber's parabolic equation is proven beneficial. Considering a material like hardened AISI 4340 for the shaft, which is neither too brittle nor too ductile, the Goodman or Gerber equations can be used. Henceforth, for a fully reversed stress loading, the effective alternating stress (σ_{Effalt}) using Gerber's parabolic equation is

explained in Equation 8.3.7 [73].

$$\sigma_{Effalt} = \frac{\sigma_{alternate}}{1 - \left(\frac{\sigma_{mean}}{UTS}\right)^2} = 91.8MPa \quad (8.3.7)$$

$$\text{Margin} = \frac{EL_{mod}}{\sigma_{Effalt}} - 1 = 2.384 \quad (8.3.8)$$

A margin of 2.384 was obtained from solving Equation 8.3.8, which subtracts the ratio of the modified endurance limit to the calculated effective alternating stress with 1. The so-calculated margin ≥ 0 indicates that it is a positive margin for the fatigue life of a component, and thereby, the local stress concentration would not impact the life of the integrated design upon cyclic loading.

Chapter 9

Dynamic Performance of Integrated Shaft-Hub Design

Dynamic performance pertains to the realm of structural mechanics, delving into an object's behavior in response to acceleration or time-based equations, which might include studying its reaction to impact loading or analyzing the motor's vibrational characteristics. The impact loading is not prioritized since it is assumed that the carbon fiber and other components have undergone thorough analysis and optimization through static analysis. However, studying the vibrational characteristics of the motors is crucial as they significantly influence the motor's performance. Four significant frequencies influence the machine's performance: eigen, electrical, operating, and critical frequencies. The eigen frequency represents the natural frequency of the designed assembly, while the maximum mechanical rotor frequency aligns with the highest speed of the rotor assembly. On the other hand, the critical frequency pertains to the speed at which the shaft encounters maximum transverse displacements, and the electrical frequencies are derived from the electromagnetic characteristics of the

machine. When the electromagnetic harmonic frequency closely aligns with the modal frequency, it can lead to a sharp increase in the amplitude of vibration, significantly degrading the motor's sound quality. In a hypothetical motor where all mechanical components are flawlessly manufactured and electrical fields change instantaneously, the machine dynamics would be uniform without any variations. However, in real-world scenarios, several factors lead to slight inconsistencies in machine dynamics. These variations create ripples, especially as the rotational frequency increases. The primary goal is to avoid frequency clusters to prevent resonance, which can lead to fatigue and potentially result in catastrophic motor failure. This chapter includes a detailed discussion and analysis of the integrated design in a dynamic environment.

9.1 Eigen Frequency Analysis of Integrated Design

Eigen frequency, also known as natural frequency, denotes the inherent frequencies at which a system or object naturally vibrates without any external force acting upon it, and the so-obtained pattern of motion is defined as mode shape or eigenshape. Eigen frequencies are often enhanced during vibration optimization studies to avoid resonance in a mechanical structure [74]. Resonant frequency refers to the frequency at which an external force induces the maximum motion in an oscillating system (close to the system's natural frequency). Improving the structural stiffness leads to higher eigen frequencies since frequency is directly proportional to stiffness and inversely proportional to the mass of a component. To validate the results of a modal analysis (also known as eigen mode analysis), certain key considerations were made.

- The mode shape is analyzed for the entire system rather than individual components. If we were to study the frequency of the individual components, the integrated design's frequency, for instance, would be considerably high (above $2000Hz$). Therefore, it is essential to examine the eigen frequency of all the significant structural stator and rotor components.
- Analyzing the eigen frequency as a system is the preferred approach. Stiffness plays a crucial role in determining the eigen frequency, and factors such as applying preload and considering the stiffness of neighboring components significantly influence the accuracy of the assembly frequency.
- The removal of all thermal and structural loadings from the system is essential, as the fundamental equation of eigen frequency solely depends on the stiffness and mass matrix of the system.
- To prevent any undesirable amplitude gain in components when the mode shape resonates with the system mode, all interference, transition, just-touch, and clearance contacts are transformed into tied contacts. This conversion ensures stability and eliminates unwanted effects during resonance.

With the considerations in place, we now delve into common questions like "How can we ensure the accuracy of the results?" and "What specific outcomes do we aim to achieve from these results?" which will be addressed below.

- The first 6 modes of the system should mirror the rigid body modes, which are specific motions in distinct directions, either X, Y, and Z translations or rotational axes, occurring near $0Hz$. A free-free eigen mode analysis is conducted

to obtain the rigid body modes, which serve as indicators of the accuracy of the simulation setup.

- The first 6 eigen frequencies, following the 6 rigid body modes, should exhibit appropriate mode shapes, including fore-aft or breathing axial mode, transverse mode, axial torsional modes, and combined two-point or three-point bending modes. A constrained eigen mode analysis would eliminate the rigid body modes as it added boundary stiffness to the simulation.
- The first 6 eigen frequencies after the 6 rigid body modes must be well separated from any critical, electrical, or operating frequencies by at least $50Hz$, ensuring they do not overlap, which will lead to resonance.

To comprehend the significance of the aforementioned results, it is essential to grasp the methodology employed to obtain them. In the following two subsections, a comprehensive analysis will be presented, demonstrating the variation of eigen frequencies with different mode shapes. While eigen analysis does not require any constraints, applying mounting constraints introduces additional stiffness to the model. In free-free analysis, the first six modes represent rigid body modes, with the seventh mode corresponding to the first eigen frequency. These rigid body modes are low-stiffness modes that do not induce strain in the model and are characteristic of free-free analysis. It is crucial to ensure that only the expected six rigid body modes, denoting XYZ translation and rotation frequencies around 0, are present. Any rigid body modes or low-stiffness modes occurring from the seventh frequency or earlier should be carefully examined as they might result from an under-constrained part in the simulation.

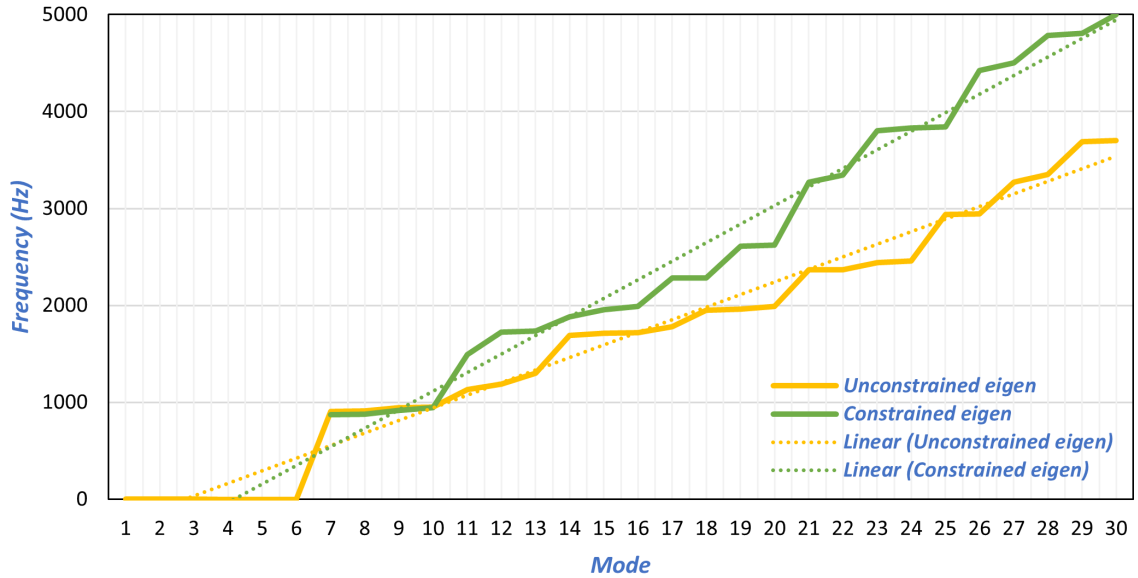


Figure 9.1: Comparison of eigen frequencies of constrained and unconstrained analysis setup of integrated design

The eigen analysis for the constrained setup is similar to the durability setup. During eigen analysis, it is important to apply pretension loads on the main and smaller bolts, as these forces enhance the model’s stiffness and subsequently increase the system’s frequency. Moreover, additional masses such as copper coil mass and water mass were included as lumped mass features in the model to represent damping, resulting in a reduction of the overall frequency. Figure 9.1 compares the two analysis setups. Several authors [75–77] have conducted various dynamic response analyses, but they were focused on individual components rather than the assembly level. When eigen frequencies are studied at the component scale and optimized, their mode shape changes when assembled due to a much higher constrained boundary stiffness, increasing in component frequency, as depicted in Figure 9.1. The linear relationship between the setup showcases a deviating frequency path stating that the δf would increase as the mode increases.

<i>Mode number</i>	<i>Frequency (Hz)</i>	<i>Type of mode</i>
1	869.89	Axial cross
2	877.82	
3	914.64	Radial cross
4	946.17	Shaft radial breathing
5	1492.57	Axial fore-aft
6	1723.75	Radial XX fore-aft
7	1737.4	Radial YY fore-aft
8	1884.54	Z rotation
9	1956.37	Casing breathing
10	1987.9	Casing breathing

Table 9.1: Critical eigen frequencies for the first 10 modes for the integrated design assembly

Two conclusions can be drawn from Figure 9.1. Firstly, the eigen frequency is most suitable for assessment when the setup is constrained, similar to the durability setup depicted in Figure 8.7. Secondly, the unconstrained setup can be employed to assess the structural integrity of the system, given the absence of local modes. The first six modes in the integrated design rotor assembly are identified as rigid body modes in various directions, including X, Y, and Z transitions and rotations. However, when analyzing the eigen frequency, special attention is given to mode shapes resembling the highest transverse mode followed by an axial mode shape, as these are considered critical eigen frequencies. Table 9.1 displays the initial eigen frequency starting at 869.89Hz , wherein the 1^{st} mode exhibits an axial cross mode, indicating the longitudinal mode being influenced by two vectors in different directions. The 2^{nd} and 3^{rd} modes exhibit axial and radial cross modes, respectively, and do not significantly influence radial vibration.

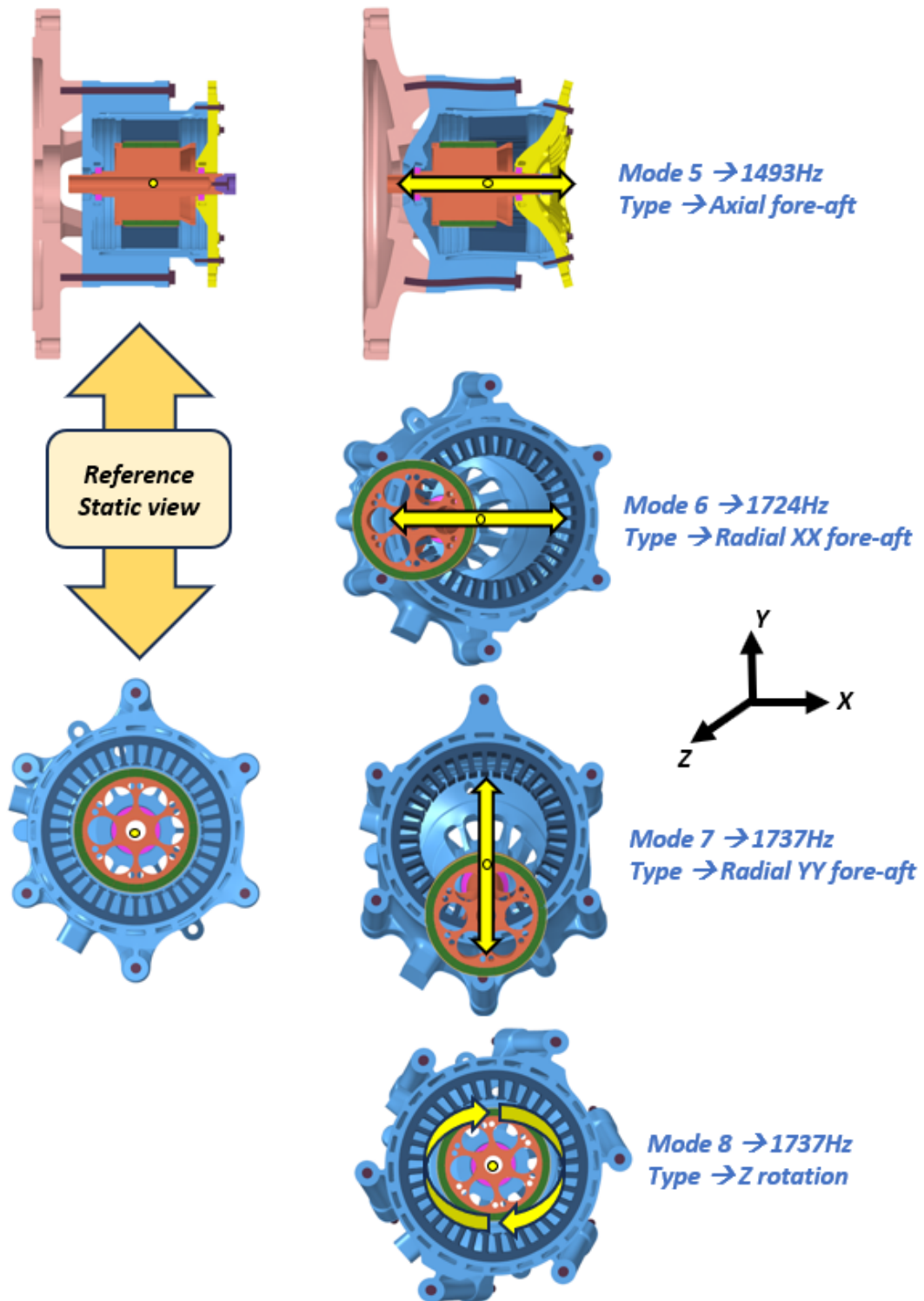


Figure 9.2: Critical eigen frequencies and their mode shapes

On the other hand, modes 5, 6 and 7 are crucial as they form zero order modes with maximum amplitude (resulting in maximum strain and displacement) due to their true mode shapes as shown in Figure 9.2. The zero-order modes in resonance with any other critical frequencies would lead to catastrophic failure of zero'th order component.

9.2 Analytical Critical Speed Estimation

Estimating critical speed is a challenging task, and existing rotor dynamic software can be intricate, often requiring numerous numerical inputs that may not be readily available during the design phase. Therefore, this chapter will include a section that outlines the analytical calculation of critical speed using both the Dunkerley and Reileighs method. Given the complexity of the rotor assembly in the integrated design, a simplified version is generated, containing only the essential dimensions needed to calculate the critical speed, as depicted in Figure 9.3. The shaft possesses its own critical speed due to its mass. At the same time, the mass attachments to the shaft (the hub and PMs) also have a critical speed that is considerably lower than the shaft's intrinsic critical speed. In cases where the geometry is straightforward, such as a shaft with a uniform diameter and simply supported, determining the critical speed (ω_s) becomes a relatively simple task [45, 78]. It can be expressed as shown in Equation 9.2.1

$$\omega_s = \left(\frac{\pi}{l}\right)^2 \cdot \sqrt{\frac{g \cdot E \cdot I}{A \cdot \gamma}} \quad (9.2.1)$$

In Equation 9.2.1, l is the length of shaft, g is acceleration due to gravity, E is the

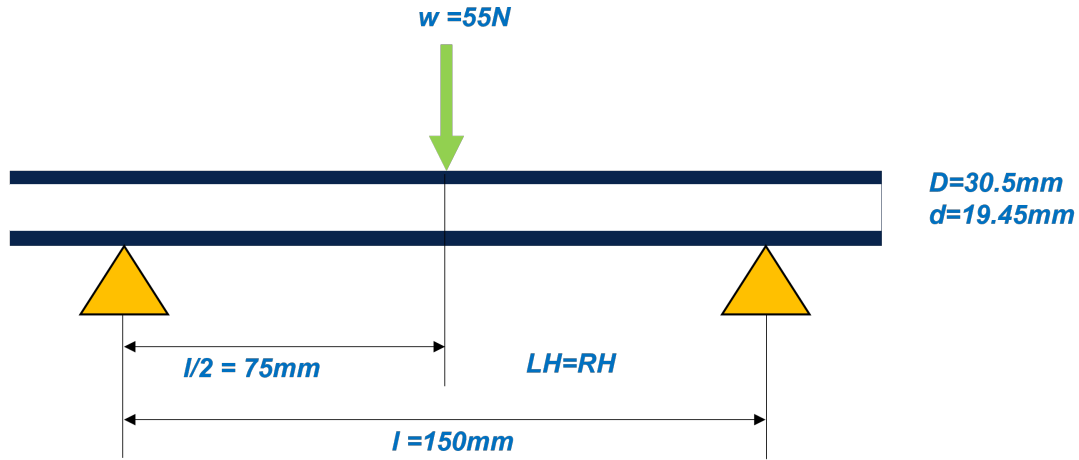


Figure 9.3: Free body diagram of the integrated design

young's modulus, I relates to the second moment of area obtained from $\frac{\pi}{64}(D^4 - d^4)$, A being the cross-section area of shaft and γ translates to the specific weight. After plugging in the parameters, the natural frequency of the shaft without considering the weight is calculated to be $3339Hz$. However, in our specific case, where there is a load of $55N$ acting at the center of the shaft, modified Rayleigh's equation for lumped mass can be used along with influence coefficients. Influence coefficients are the transverse deflection at any instantaneous point (i^{th} location) due to a load at j^{th} location. Henceforth Shingly [45] suggests that for a single unit load acting on the shaft that is simply supported, the deflection at i, j^{th} location is given by the Equation 9.2.2.

$$\delta_{ij} = \frac{b_j \cdot x_i}{6 \cdot E \cdot l \cdot I} (l^2 - b_j^2 - x_i^2) \quad (9.2.2)$$

Here the b_j refers to the distance between the load center to the other end of the simply supported beam and is considered $75mm$. The variable x_i represents the distance from the instantaneous point to the other end of the simply supported

beam. In this case, we assume that the instantaneous point is located at the center of the load application, making x_i equal to half of the total distance between the two supports, which is $75mm$. Henceforth the influence coefficients δ_{ij} is calculated as $9.96e^{-6}mm/N$. With the help of influence coefficients from Equation 9.2.2, the deflections can be calculated from Rayleigh's Equation 9.2.3 and 9.2.4.

$$y = w \cdot \delta_{ij} \quad (9.2.3)$$

$$\omega_1 = \sqrt{\frac{g \sum w_i y_i}{\sum w_i y_i^2}} \quad (9.2.4)$$

From Equation 9.2.3 the deflection is calculated as $5.46^{-4}mm$ and upon substitution in Equation 9.2.4 the critical speed of the shaft with attachments obtained through Rayleigh's equation is $674Hz$. Dunkerley's equation, on the other hand, can be used to cross-check critical speed from Rayleigh's equation by also including the shaft's critical speed.

$$\omega_{11} = \sqrt{\frac{g}{w_j \delta_{ij}}} \quad (9.2.5)$$

Equation 9.2.5 provides a condition to calculate the critical speed of the ensembled weight with a calculated value of $674Hz$. The dunkerley's critical speed equation is the inverse summation of squares of all the critical speeds of various attachments calculated in Equation 9.2.5. Since in the integrated design, there is solely a single central mass, the dunkerley's critical speed will be the same as the critical speed of ensembled weights calculated in Equation 9.2.5. But to calculate the actual critical speed of the shaft using dunkerleys equation, considering the influence of weights is

provided by Equation 9.2.6.

$$\frac{1}{\omega_{ds}^2} = \frac{1}{\omega_d^2} + \frac{1}{\omega_s^2} \quad (9.2.6)$$

Henceforth the final critical speed modifying dunkerleys equation as a function of the shaft critical speed is calculated to be $661Hz$, which is $13Hz$ lower than the critical speed obtained from Rayleigh's equation. The difference between the results of the two methods was observed to have a higher delta as the ensembled attachments increased. Moreover, Shingley's mechanical design book [45] suggests keeping critical speeds at least 1.5 to 2 times the operational speed as eccentricity and misalignment prepones the critical speed. With a high-speed operating frequency of $333Hz$ it can be concluded that the critical frequency of the shaft at $661Hz$ does not cause any resonance with the eigen frequency starting at $869Hz$ nor with the electrical frequency at $6000Hz$.

Chapter 10

Manufacturing Processes Involved in Integrated Design

The selected material for the integrated design is AISI 4340, a commonly used shaft steel for high-speed applications. However, what sets it apart and how it can be machined from a single block of AISI 4340 for a 240mm long shaft remains a question. This chapter will explore the answers to these questions and provide insights from experienced machinists for achieving the desired design. To provide the best performance and dependability, motor shafts for high-speed operations are chosen based on several essential factors. Among the crucial factors taken into account are:

Material Strength → The shaft's material needs to be strong enough to sustain the strains produced at high speeds without deforming or failing. The study revealed that the shaft experiences stress spikes close to the bearing shoulder region, reaching approximately 500MPa. A shaft with a higher stress resistance, featuring a minimum yield strength of 750MPa, offers more capacity to handle stresses, thereby increasing its strength tolerance. In order to boost the strength of metals, alloying elements are

frequently added such as carbon, manganese, chromium, etc. These alloying components can alter the metal's grain size, dislocation movement, and crystal structure, which will improve the metal's mechanical qualities like strength and hardness.

Fatigue Resistance → To sustain repeated fully reversed cyclic loading during ongoing high-speed operations, shaft materials should have strong fatigue resistance. Higher chromium content in alloy metals enhances the material's ability to resist corrosion and oxidation, thereby leading to an overall improvement in its fatigue resistance.

Stiffness → To reduce deflection and vibrations and ensure smooth operation, high-speed motor shafts must be rigid case surfaces and a semi-flexible core. This provides some flexibility, reducing stress during high-speed operations. The addition of higher carbon content, combined with suitable case hardening or nitriding, will fulfill the necessary requirements.

Hardness → In the presence of possible impurities or challenging operating conditions, proper hardness levels are crucial to withstand wear and abrasion. Elements like carbon, chromium, and molybdenum play a significant role in enhancing the hardness of the component. Surface hardness is crucial as it helps resist bending and torsional deformations. However, it is essential to strike a balance, as extremely hard surfaces can make the component brittle due to a smaller work-hardening region.

Machinability → To facilitate effective manufacturing procedures, the chosen material should be readily machinable. It is advisable to machine alloy metals before the hardening process. When alloy metals are pre-hardened with a Rockwell C hardness (HRC) above 55, machining becomes challenging, leading to issues such as tool breakage or difficulties in achieving precise tolerances for the final component.

Thermal conductivity → High-speed motor shafts should have a high thermal conductivity to aptly disperse heat and avoid overheating during extended operations. The inclusion of copper (beryllium copper) or aluminum alloys significantly enhances thermal conductivity, albeit at the expense of compromising structural strength. In contrast, titanium exhibits relatively higher thermal conductivity than other high-strength metals.

Weight and cost → A lightweight shaft can help the motor accelerate and decelerate more quickly by reducing its rotational inertia. Cost-effectiveness is a factor as well, and the chosen material should strike a balance between affordability and performance.

The rationale behind selecting AISI 4340 is extensively explained in Chapter 6, and the subsequent sections of this chapter will delve into the manufacturing aspects. The AISI 4340 steel bar, with a diameter $2mm$ larger than the largest diameter of the integrated design, will be procured from the vendor. Additionally, the overall length of the bar will extend $2mm$ beyond the required dimensions. A prehardened shaft is avoided for two main reasons: Firstly, the hardening process makes the shaft core brittle, increasing the likelihood of fatigue failure under high-stress conditions. Secondly, pre-hardening the shaft up to HRC 55 may introduce residual strain from machining, which could reduce the effectiveness of surface-level compressive stresses transitioning to tensile stresses. As shown in Figure 10.1, the integrated design comprises approximately five significant features that require machining, including splines, larger and smaller turning radii, fillets, and chamfers, as well as cutouts and grooves. A 3-axis CNC lathe machine is necessary for machining certain features, such as the $0.7''$ radius, which requires a tool head capable of movement in three axes.

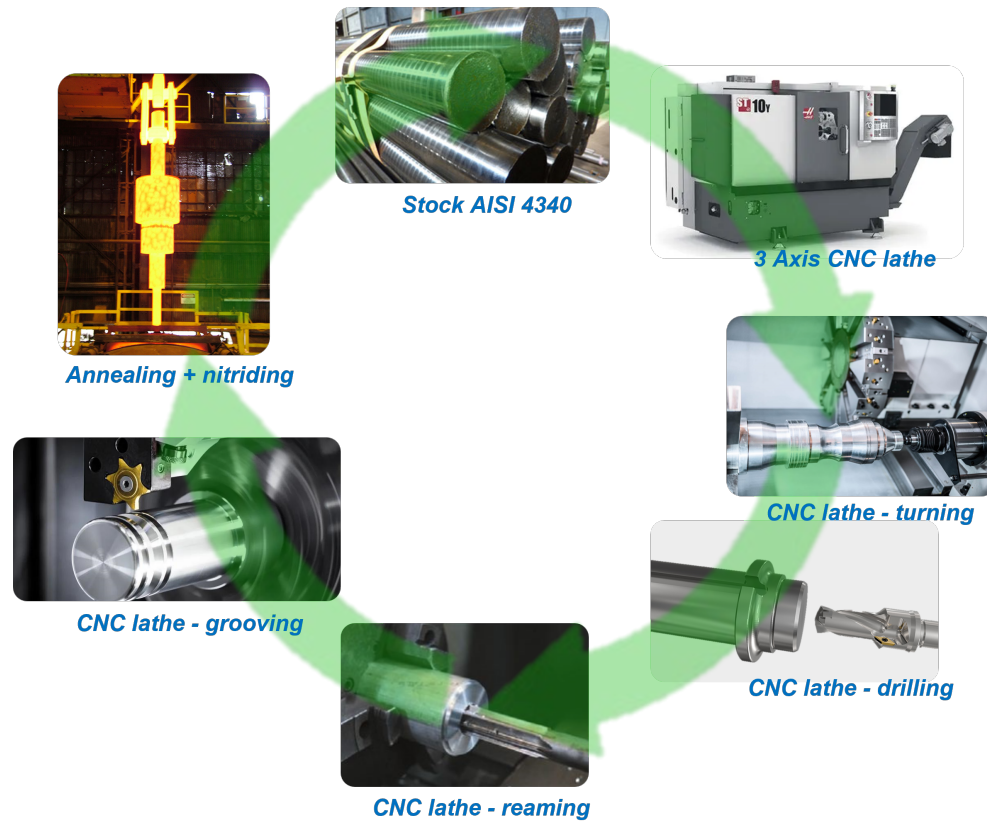


Figure 10.1: Various machining processes involved in the integrated design

Given that the integrated design has a length of 230mm , with the two ends having smaller outer diameters than the central outer diameter, the entire turning process must be executed in two steps. Step 1 involves multiple passes to accommodate larger material removal while the chuck securely holds the bearing shoulder location on the A-side. Utilizing the bearing shoulder as a fixture for machining is appropriate since the central mass of the larger diameter is positioned closest to the chuck, providing vertical support and minimizing component vibration during machining, thereby reducing inaccuracies. During Step 2, the component is rotated 180° so that the B-side bearing shoulder location is brought into the chuck for the same turning process. It

is crucial to maintain the fixture locations for both the A-side and B-side without any changes, as they define the geometric center of the machined component. After completing all the turning processes, there are only two remaining machining steps: drilling the central slots and the ID, as well as grooving the bearing shoulder location for the fan's retainer rings. To create the slots, larger diametric cutouts are chosen based on standard and common tool sizes available to the machinists. The 1.1" diameter slots are best machined using a three-pass process, with tool sizes of 75%, 90%, and 98% of the hole diameter selected to ensure vibration-free drilling and higher accuracy. First, the A-side is drilled halfway, and then the component is rotated 180° to drill the B-side similarly. A final reaming is performed to achieve high tolerance on the holes. Although there are no attachments, this activity is necessary to reduce the imbalance from continuous machining. The grooving process is carried out similarly to turning but with a grooving tool designed to match the depth and edge radius of the standard retainer ring.

After the main machining process, a surface finishing step is performed by grinding the machined surfaces to smooth out any surface-level stresses and irregularities resulting from turning and drilling. The most common shaft surface finish is maintained at $0.10\mu m$ to strike a balance between the necessary lubrication roughness for bearings and wear protection under high-stress conditions. Both surface-level and internal residual stresses are developed in the material during stress application, resulting in tensile stress and a decrease in the component's fatigue resistance. To counter this, a heat treatment process known as annealing is commonly used for alloy metals. In this process, the metal is heated to its critical temperature ($750^{\circ}C$ for AISI 4340) for a specific duration (based on the required ductility) and then allowed to cool

in a controlled manner. At a molecular level, the rapid cooling of metals like alloy steel leads to the transformation of crystalline grains into a lenticular shape, making the metal harder and more brittle. However, heating the metal to the right temperature allows for the uniform growth of new crystals. The higher the heat applied, the greater the metal's ductility, while its hardness decreases [79]. While annealing removes the internal stresses due to machining generating a ductile core, a harder surface with compressive stresses must be attained by a process called as hardening.

The most common hardening is induction or thru-hardening process where heated coils surround the component and the material is heated ($815^{\circ}C$ to $845^{\circ}C$ for AISI 4340) and slowly cooled. But this process removes the ductility from the equation and thereby is not favorable for high-speed shafts. Case hardening or nitriding is best to increase surface-level hardness. In case hardening, the heat is supplied through the same induction coil but at a relatively faster rate based on the depth of hardness required. Nitriding is conducted at temperatures below the transformation temperature of alloy steels to minimize or eliminate any distortion caused by the process. Afterward, the parts are exposed to active nitrogen at a carefully controlled temperature, usually within the range of $925^{\circ}F$ to $985^{\circ}F$. This temperature is typically below the final tempering temperature of the steel, ensuring that the nitriding process does not affect the mechanical properties of the base metal. Gas nitriding is a surface treatment process that introduces nitrogen to steel parts using dissociated ammonia as the nitrogen source. Through gas nitriding, a robust and hardened case is formed on the component's surface at relatively low temperatures, eliminating the need for quenching [80]. It is worth noting that gas nitriding tends to be a more expensive process than case hardening.

Chapter 11

Ideal Configuration of Strain

Gauges – Test Setup

FEA results are typically corroborated with analytical solutions, logical reasoning, or physical validation through specific testing methods. The integrated design, along with boundary components and various loading scenarios, involves a vast number of elements, making analytical calculations extremely laborious and free-body diagrams less precise. Therefore, logical inferences are drawn from the FEA results to arrive at conclusions. Additionally, incorporating standardized testing procedures would provide greater confidence in the FEA outcomes, enabling adjustments to be made to achieve results that closely align with test/CAE correlations. Enhancing confidence in a well-correlated FE model would lead to improved optimization and, consequently, enhance the overall performance of the machine. This section provides a detailed description of various static and dynamic testing procedures that can be employed to achieve a strong correlation between the experimental and simulated results. Static testing is conducted when there are no accelerated loadings, such as impact loading

or response functions, applied to the system. The setup for static testing is similar to that of a dyno setup, with thermal and centrifugal loadings acting on the system. To achieve an accurate correlation between experimental and simulated results, it is crucial to ensure that the test setup closely resembles the FE setup, considering the sensitivity of the integrated design's boundary conditions to rotor high-speed performance and vibrational characteristics. To achieve static correlation, the most effective approach involves examining the displacements at different points within the system. This study of displacements offers valuable strain data, which can then be converted into functional stress information using the hooks law in Equation 11.0.1.

$$\sigma = E \times \varepsilon \quad (11.0.1)$$

Strains are typically measured through a device known as a strain gauge. A strain gauge serves as a sensor to gauge the strain or deformation of an object when exposed to external forces. It operates by altering its electrical resistance in response to mechanical strain. As the object experiences deformation, the shape of the strain gauge changes, leading to a proportional change in electrical resistance. This change in resistance can be measured and utilized to determine the strain or stress applied to the object [81]. By offering valuable data, they aid in comprehending the behavior and performance of materials and structures under varying circumstances. The common types of strain gauges designed to measure strain are showcased below.

- *Metal Foil Strain Gauge* → This type is the most widely used and common strain gauge. It comprises a metal foil (made of constantan or karma) bonded to a flexible backing material. When subjected to strain, the metal foil experiences changes in electrical resistance, which is measured to determine the strain.

- *Semiconductor Strain Gauge* → These gauges are made of semiconductor materials like silicon or germanium. They offer higher sensitivity and better temperature compensation capabilities than metal foil strain gauges.
- *Wire Strain Gauge* → Wire strain gauges are composed of fine wire, often platinum or tungsten, arranged in a grid pattern. Changes in the wire's electrical resistance with strain allow for strain measurement. They are typically used in high-temperature environments.
- *Optical Strain Gauge* → These gauges utilize optical techniques to measure strain. They rely on fiber optic sensors or interferometric methods to detect changes in the material's optical properties induced by strain.
- *Piezoelectric Strain Gauge* → This type is based on piezoelectric materials that produce an electric charge when subjected to a strain. Piezoelectric strain gauges are employed in dynamic strain measurements and vibration analysis.
- *Capacitive Strain Gauge* → Capacitive strain gauges measure strain changes by detecting variations in capacitance caused by mechanical deformation.
- *Vibrating Wire Strain Gauge* → These gauges use a vibrating wire element and the frequency of vibration changes with applied strain. They are suitable for long-term measurements in harsh environmental conditions.

In the integrated design, the strain analysis primarily focuses on regions near the bearing base and shoulder locations. The strain tensor analysis reveals that these regions exhibit a high level of uniaxial strain with negligible traces of a biaxial strain. Uniaxial strain systems are characterized by predominantly occurring in one of the

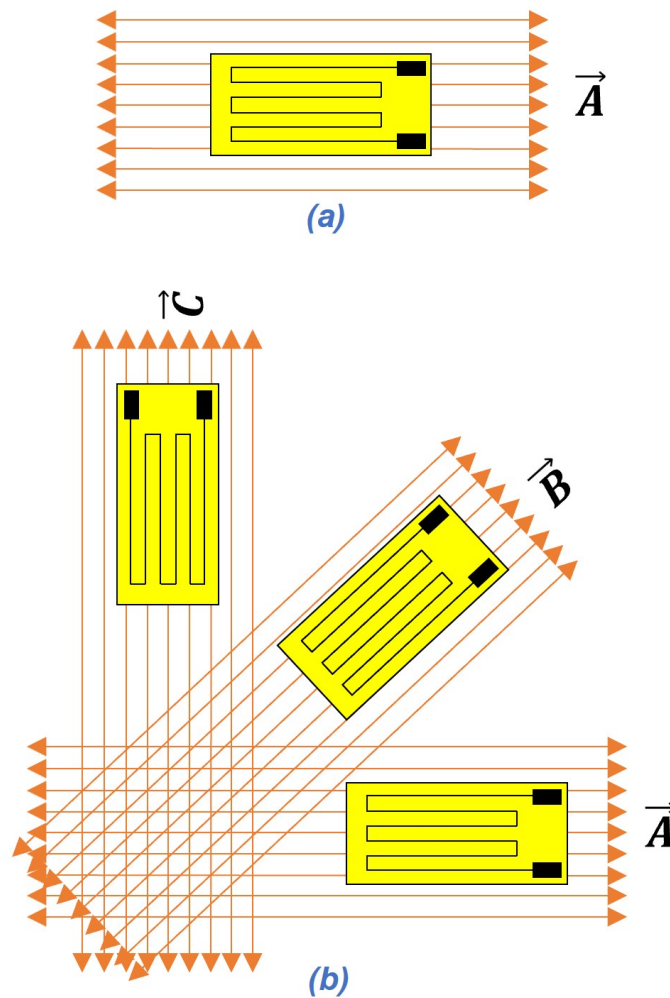


Figure 11.1: (a)uniaxial strain (meets criteria) (b) triaxial strain gauge setup

three principal directions of strain. In comparison, biaxial and triaxial strain systems involve strains in two or three principal directions of strain and are showcased in Figure 11.1 respectively. To confirm this observation, a strain tensor analysis is conducted on the top loading condition. As the strains are primarily uniaxial, there is no necessity for a strain gauge rosette, as depicted in Figure 11.1, to capture strains in multiple directions. There are three possible ways in which a uniaxial strain gauge can be arranged, especially when the loading increases and the sensitivity of the strain

measured is vital. The distinction among quarter, half, and full bridge strain gauges lies in the number of strain gauges employed in the bridge setup.

- *Quarter Bridge Strain Gauge* → In a quarter-bridge strain gauge configuration, a single active strain gauge element is used, placed on one side of the material being measured. The bridge completion is typically achieved using precision resistors. Quarter bridge setups are straightforward and cost-effective, but they have limited sensitivity and are more susceptible to temperature variations and lead wire effects. They are well-suited for applications with low strain levels and when cost is a primary consideration.
- *Half Bridge Strain Gauge* → In a half-bridge strain gauge configuration, two strain gauges are utilized in a bridge arrangement, with one gauge placed on the top and the other on the bottom of the material. Half bridges provide better sensitivity when compared to quarter bridges and are less influenced by temperature changes and lead wire effects. They are suitable for moderate strain measurements and offer a good compromise between cost and performance.
- *Full Bridge Strain Gauge* → In a full bridge strain gauge configuration, four strain gauges are arranged in a bridge, with two gauges placed on the top and two on the bottom of the material. Full bridges offer the highest sensitivity and are less impacted by temperature changes and lead wire effects. They provide precise and dependable measurements, making them ideal for applications with high strain levels or where precision is critical.

Given that the strain levels on the bearing base and shoulder are relatively low, a half-bridge strain gauge may be adequate. While the ideal choice would be to utilize



Figure 11.2: Induction based telemetric setup [11]

a full bridge strain gauge, it would necessitate a transmitter capable of transmitting signals from three channels. This would result in a larger transmitter size, potentially leading to fitment issues in the overall design.

The test setup is carefully designed to ensure that the boundary conditions (end plate and stator casing) of the integrated shaft closely resemble the final assembly. Using a bombshell or any other rigid setup would alter the modal pattern of the rotor assembly, potentially affecting the vibration characterization. While the structural durability would not be impacted significantly by the change in boundary conditions, the accuracy of vibration characterization would be compromised. Upon identifying the application of strain gauges from Figure 11.1, the test setup will be discussed in this section. Given the high rotational speeds of the rotor assembly, it is essential to use a dependable and highly sensitive telemetric system. There are two types of telemetric systems available: one that utilizes radio frequency transmission to send

data to an external receiver, and the other method involves using an induction ring being a relatively newer technology. The standard setup uses a radio frequency, where the strain gauge channels are connected to a battery-powered transmitter. However, incorporating the power source (a single 9V battery weighing approximately 86g) within the rotor assembly can lead to increased rotational inertia and potential issues with mass balance on the shaft. With limited packing space, this would lead to more concerns. Henceforth the induction-based telemetric setup is apt for the current motor testing as shown in Figure 11.2. The crucial aspect is determining the locations for conducting test/CAE correlation. These critical locations are selected based on high-stress areas, and the direction of the strain vector determines the orientation of the strain gauge.

Chapter 12

Conclusions and Future Work

The primary objective of this thesis is to develop and verify an integrated design approach for the hub and shaft of a Radial-flux SPMSMs. This approach addresses mechanical challenges and implements countermeasures to enhance the design and analysis accuracy, ultimately leading to higher power density in the motor system.

12.1 Thesis Summary

The summary of this thesis can be explained in 10 points as mentioned below:

1. A clear overview of the principles and functioning of PMSMs was provided, accompanied by an in-depth discussion of their applications in More Electric Aircraft (MEA) systems and other electro-mechanical subsystems, including wing actuators and aircraft generator applications.
2. Radial-flux SPMSMs encounter structural integrity problems arising from an increased number of press-fit components, inadequate magnet retention, and a

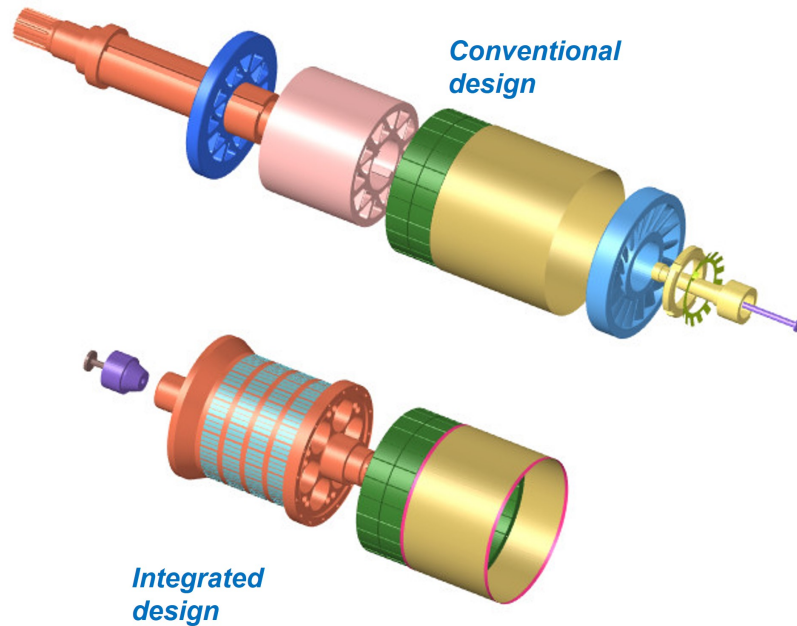


Figure 12.1: Conventional vs integrated design approach

less rigid rotor core, which results in higher core mass and ultimately lowers the power density of the motor.

3. A new approach for the integrated design of the hub and shaft using AISI4340 as shown in Figure 12.1 was studied . The usage of halbach array reduces the necessity of a back iron to be made from electrical steel due to the minimal flux production on the back iron face.
4. The electromagnetic analysis demonstrated that AISI4340 performed comparably to achieve similar torque and power outputs of $74Nm$ and $155kW$, respectively, with a similar total loss of $3.77kW$. Despite a 29% increase in torque ripple percentage, this sacrifice was justified by the overall enhancement in mechanical performance and power density.

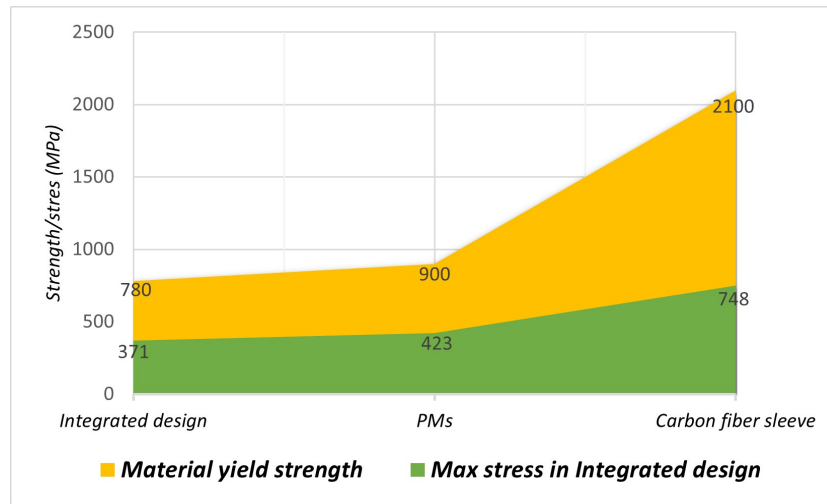


Figure 12.2: Max von mises stress from FEA vs yield strength of material

5. A comprehensive examination of the design considerations for the integrated design was presented, encompassing the essential inclusion of air pockets on the rotor core to enhance mass flow rate and provide stronger cross-section support between the back iron and shaft. Additionally, the integration of balancing holes facilitated rotor balancing activities.
6. This thesis presented a comprehensive FEA modeling, integration, and analysis approach resembling a test bench setup. It encompassed various stages, including mesh sensitivity analysis, contact modeling parameters for non-linear convergence, and a detailed multiphysics simulation setup. The combination of steady-state linear static and non-linear contact-based analysis was highlighted, emphasizing the significance of well-defined boundary and loading factors.
7. The multiphysics simulation had two primary goals: to determine the shaft displacements layout and to ensure that all von Mises stresses remained below the yield strength, as depicted in Figure 12.2. The results for the optimized design

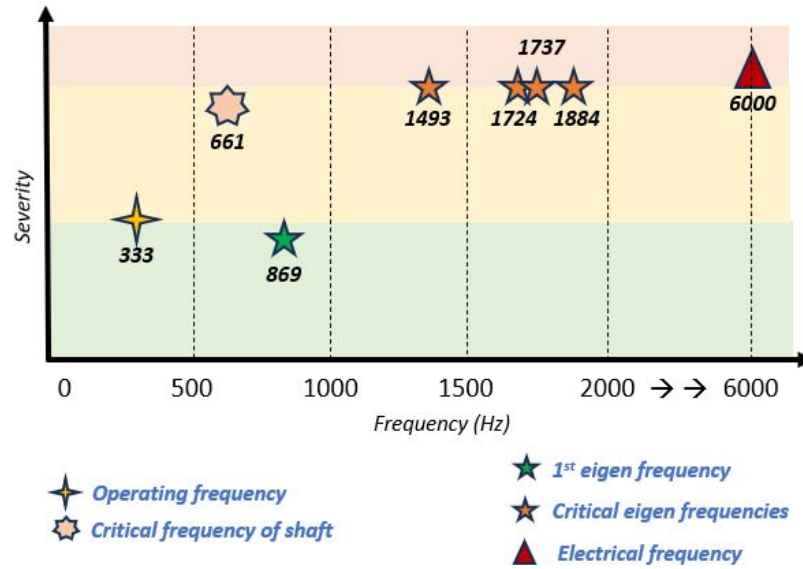


Figure 12.3: Frequency array of all dominant frequencies in the system

were obtained after 130 iterations, employing various modeling, integration, and design strategies.

8. In addition to the thorough study of static analysis, dynamic analysis was equally significant. The investigation encompassed critical shaft, eigen, electrical, and operational frequencies, ensuring that resonance was prevented by avoiding critical frequency clusters, as illustrated in Figure 12.3. Various adjustments were made to preempt or postpone critical frequencies, aiming for a safe range within $50 - 100Hz$.
9. The structural optimizations resulted in an overall mass reduction of 26% from the contemporary design, also focused on ensuring ease of manufacturability by utilizing commonly available tool dimensions and machining methods such as

CNC 3-axis lathe turning, drilling, reaming, grooving, and surface grinding. Additionally, a two-step process involving annealing and nitriding was established to enhance the surface hardness of AISI 4340 to 55 HRC.

10. The test procedure centered on strain gauges, their types, and arrangement was outlined. It was concluded that a half-bridge uniaxial strain gauge would be suitable since the strain tensors were primarily uniaxial, and this configuration would consider thermal expansion while locally measuring strain. Furthermore, detailed information on the induction-based telemetric system was provided in this thesis.

12.2 Future Work

Regarding future work, three key areas demand more comprehensive investigation.

1. *Test validation of integrated design*→ After providing an extensive account of the FEA outcomes, which include maximum stress, strain, strain tensor, and displacement patterns, along with a comprehensive test bench arrangement and measurement tools, it is crucial to conduct a physical validation to verify the accuracy of the FEA results. In various scenarios, there are discrepancies between FEA and test results due to the applied modeling and integration techniques. For instance, an inaccurate mesh on a feature can result in an increased stress concentration factor (k), leading to incorrect von Mises stress outputs during post-processing. Additionally, issues arise when using integration strategies involving kinematic and distributed couplings, giving rise to significant boundary value concerns.

2. *Mass optimization of integrated design* → The extensive optimization efforts resulted in an overall mass reduction of 26% (equivalent to 1.1kgs). The maximum von Mises stress values observed were 372MPa on the rotor back iron, 302MPa on the shaft bearing shoulder locations, and 312MPa on the rib section. Importantly, all stresses remained below the material's yield strength of 780MPa, indicating that only 50% of the material strength was utilized. Considering a safety margin of 1.2 for the material's yield strength, an additional 35 – 40% of the material strength can be utilized. To achieve this, further parametric optimization, particularly by varying the slot parameters, is recommended after obtaining a correlated test/CAE model.

3. *Precise critical speed estimation* → The critical frequency, commonly referred to as the shaft whirling frequency, was determined using analytical methods like Rayleigh's and Dunkerley's approach, resulting in a calculated value of 661Hz. However, it is important to note that this estimate is based on design-level analysis. In practical environments, various factors can influence the actual critical frequency, such as variations in the internal material density of the integrated shaft, eccentricity arising from machining tolerances, and uneven uni or biaxial loading caused by offset or angular coupling of the motor shaft and dyno shaft. These real-world complexities should be considered when assessing the shaft whirling behavior in a physical setting. Rotor dynamic software such as Dyrobes can provide the user the liberty to input critical assumptions on the axial/radial eccentricity, bearing dynamics (lobe type modeling), and CG offset without changing the load center.

Bibliography

- [1] M. Torabzadeh-Tari, “Analysis of electro-mechanical actuator systems in more electric aircraft applications,” *KTH Electrical engineering*, May 2005.
- [2] M. Galea, Z. Xu, C. Tighe, T. Hamiti, C. Gerada, and S. Pickering, “Development of an aircraft wheel actuator for green taxiing,” pp. 2492–2498, 2014.
- [3] G. Du, N. Li, Q. Zhou, W. Gao, L. Wang, and T. Pu, “Multi-physics comparison of surface-mounted and interior permanent magnet synchronous motor for high-speed applications,” *Machines*, vol. 10, no. 8, 2022.
- [4] A. El-Refaie, “Fractional-slot concentrated-windings: A paradigm shift in electrical machines,” pp. 24–32, 2013.
- [5] C. industries corporation, “Why encapsulating electric motor with epoxy resin?,”
- [6] T. engineer, “Permanent magnet synchronous motor construction,” 08 2020.
- [7] A. Manikandan, M. Abdalmagid, G. Pietrini, M. Goykhman, and A. Emadi, “Rotor durability optimization by means of finite element multiphysics analysis for high-speed surface permanent magnet electric machines,” vol. 2023-01-0529, 2023.

- [8] C. Danielle, “What is a halbach array and how is it used in electric motors?,” *Motion control tips*, 06 2018.
- [9] “Contact,” *Altair OptiStruct documentation*, 2021.
- [10] A. Constantinescu, K. VAN, and H. Maitournam, “A unified approach for high and low cycle fatigue based on shakedown concept,” *Fatigue Fracture of Engineering Materials Structures*, vol. 26, pp. 561 – 568, 05 2003.
- [11] “Wireless sensor telemetry systems - induction based,” *Michigan scientific*, 2023.
- [12] M. Chen, K. T. Chau, W. Li, and C. Liu, “Cost-effectiveness comparison of coaxial magnetic gears with different magnet materials,” *IEEE Transactions on Magnetics*, vol. 50, no. 2, pp. 821–824, 2014.
- [13] “Global electric vehicle sales up 109% in 2021, with half in mainland china,” *Canalys*, 14th February 2022.
- [14] “Electric vehicle trends,” *S&P Global Mobility*.
- [15] “Aircraft electric motor market,” *Markets and Markets*, 2021.
- [16] K. Kharrati, “Global electric traction motor market share likely to grow at a cagr of 13% by 2030,” *Custom Market insights*, September 17,2022.
- [17] W. Tong, “Mechanical design of electric motors,” pp. 38–40, January 31,2014.
- [18] A. Hughes, “Electric motor and drives,” vol. 3, pp. 2–42, 2006.
- [19] S. B, “A review: high power density motors for electric vehicles,” *Journal of Physics: Conference Series*, p. 1706, 2020.

- [20] J. Keljik, “Electricity 4: Ac/dc motors, controls, and maintenance,” *Delmar, Cengage learning*, vol. 9, pp. 227–239, 2009.
- [21] C. Pronovost, “10 things to consider when choosing an electric motor,” *Dana TM4*, May 17, 2016.
- [22] J. Murphy, “What’s the difference between ac induction permanent magnet and servomotor technologies,” *Motors & Drives, Machine design*, April 1, 2012.
- [23] B. Zhao, B. Li, and Z. Gu, “Research on an axial flux pmsm with radially sliding permanent magnets,” *Energies*, vol. 8, pp. 1663–1684, 03 2015.
- [24] H. Mel, A. Mansouri, and H. Trabelsi, “Fea-based performances evaluation of three permanent magnet machines for traction application,” in *2019 19th International Conference on Sciences and Techniques of Automatic Control and Computer Engineering (STA)*, pp. 353–358, 2019.
- [25] A. El-Shahat and M. Ruba, “Applied electromechanical devices and machines for electric mobility solutions,” pp. 2–5, Chapter 2, Mar 2020.
- [26] H. Y. Z. T. Lin, Y., “Comprehensive design and analysis of rotor stress for hspmm considering cooling method,” *Machines*, vol. 10, p. 475, 10 2022.
- [27] S. Gopalakrishnan, “Pump research and development: Past, present, and future—an american perspective,” *Journal of Fluids Engineering*, vol. 121, pp. 237–247, 06 1999.
- [28] T. M. J. Ayman M. EL-Refaie, “Optimal flux weakening in surface pm machines using fractional-slot concentrated windings,” *IEEE transactions on industrial applications*, vol. 41, no. 3, 2005.

- [29] T. F. Johnson, “Electric green taxiing system (egts) for aircraft,” *IEEE transportation electrification community*, March/April 2014.
- [30] W. Cao, B. C. Mecrow, G. J. Atkinson, J. W. Bennett, and D. J. Atkinson, “Overview of electric motor technologies used for more electric aircraft (mea),” *IEEE Transactions on Industrial Electronics*, vol. 59, no. 9, pp. 3523–3531, 2012.
- [31] A. Mitcham and J. Cullen, “Permanent magnet generator options for the more electric aircraft,” pp. 241–245, 2002.
- [32] T. Raminosoa, T. Hamiti, M. Galea, and C. Gerada, “Feasibility and electromagnetic design of direct drive wheel actuator for green taxiing,” pp. 2798–2804, 2011.
- [33] S. Fang, Y. Wang, and H. Liu, “Design study of an aerospace motor for more electric aircraft,” *IET Electric Power Applications*, vol. 14, no. 14, pp. 2881–2890, 2020.
- [34] R.-. W. Martin, Neary, “Introductory physics: Building models to describe our world,” *Libretexts*, p. 22.3, 2023.
- [35] A. Jasim, “Performance analysis of induction motor based on core material,” *Hunan Daxue Xuebao/Journal of Hunan University Natural Sciences*, vol. 48, pp. 7–15, 08 2021.
- [36] I. E. Tamm, “Fundamentals of the theory of electricity,” vol. 9, pp. section – 3.1, initial edition - 1979, revised - 2014.
- [37] A. Reinap, “Aerospace electric generator design considerations,” pp. 1–2, 2019.

- [38] O. J. Cui Jun, “Manufacturing processes for permanent magnets: Part i—sintering and casting,” vol. 74, pp. 1543–1851, 2022.
- [39] A. Yamada and I. Miki, “Novel rotor structure of permanent magnet synchronous motor with rare earth and ferrite magnets,” pp. 1–5, 2014.
- [40] S. Irfan Ali, S. Erwan, J. Mahyuzie, and A. Hassan, “Overview of inner rotor radial permanent magnet machines for electric vehicles,” vol. 917, 2020.
- [41] A. Damiano, A. Floris, G. Fois, M. Porru, and A. Serpi, “Modelling and design of pm retention sleeves for high-speed pm synchronous machines,” pp. 118–125, 2016.
- [42] J. Liang, J. W. Jiang, B. Bilgin, and A. Emadi, “Shaft design for electric traction motors,” *IEEE Transactions on Transportation Electrification*, vol. 4, no. 3, pp. 720–731, 2018.
- [43] “Sae aisi 4340 steel properties, heat treatment, equivalent, hardness chart, density, machinability,” *The world material*.
- [44] F. B. Lynn, S. Justin, and L. Z. Charlie, “Effect of steel hardenability on stress formation in an induction hardened axle shaft,” *Stress evolution, Fluxtrol, Detroit, MI*.
- [45] G. B. Richard and N. J. Keith, “Shingley’s mechanical engineering design,” pp. 380–385.
- [46] B. Bochenkov and S. Lutz, “A review of modern materials of permanent magnets,” vol. 1, pp. 201–203 vol. 1, 2004.

- [47] M. J. Bala, D. Roy, and A. Sengupta, “The performance enhancement of bldc motor using halbach array rotor,” pp. 405–409, 2020.
- [48] C. Marco, G. Gloria, P. Stefano, and S. Enrico, “Thermal management of a formula e electric motor: Analysis and optimization,” vol. 157, July 2019.
- [49] “Partially shifted rotor laminations,” *Association of Asset Management Professionals*.
- [50] D. Schweigert, M. E. Gerlach, A. Hoffmann, B. Morhard, A. Tripps, T. Lohner, M. Otto, B. Ponick, and K. Stahl, “On the impact of maximum speed on the power density of electromechanical powertrains,” *Vehicles*, vol. 2, no. 2, pp. 365–397, 2020.
- [51] C. Xia, H. Wang, Y. Wu, and H. Wang, “Joining of the laminated electrical steels in motor manufacturing: A review,” *Materials*, vol. 13, 10 2020.
- [52] F. Zhang, G. Du, T. Wang, G. Liu, and W. Cao, “Rotor retaining sleeve design for a 1.12-mw high-speed pm machine,” *IEEE Transactions on Industry Applications*, vol. 51, no. 5, pp. 3675–3685, 2015.
- [53] F. Zhou, J. Shen, W. Fei, and R. Lin, “Study of retaining sleeve and conductive shield and their influence on rotor loss in high-speed pm bldc motors,” *IEEE Transactions on Magnetics*, vol. 42, no. 10, pp. 3398–3400, 2006.
- [54] Q. Zhao, K. Zhang, S. Zhu, H. Xu, D. Cao, L. Zhao, R. Zhang, and W. Yin, “Review on the electrical resistance/conductivity of carbon fiber reinforced polymer,” *Applied Sciences*, vol. 9, no. 11, 2019.

- [55] K. Meessen, J. Paulides, and E. Lomonova, “Analysis of 3-d effects in segmented cylindrical quasi-halbach magnet arrays,” *Magnetics, IEEE Transactions on*, vol. 47, pp. 727–733, 04 2011.
- [56] G. Chu, H. Lovatt, M. F. Rahman, and R. Dutta, “Comparative analysis of different halbach array structures in the design optimization of an in-wheel permanent magnet machine for land speed racing,” pp. 1800–1805, 2020.
- [57] M. Mallek, Y. Tang, J. Lee, T. Wassar, M. A. Francheck, and J. Pickett, “An analytical subdomain model of torque dense halbach array motors,” *Energies*, vol. 11, no. 12, 2018.
- [58] J. F. Gieras, “Design of permanent magnet brushless motors for high-speed applications,” pp. 1–16, 2014.
- [59] K. Lars and N. Karin A., “Hybrid bearings for electrical machinery,” *Evolution - Technology magazine by SKF*, Sept 16, 2001.
- [60] G. Gadamchetty, A. Pandey, and M. Gawture, “On practical implementation of the ramberg-osgood model for fe simulation,” *SAE International Journal of Materials and Manufacturing*, vol. 9, no. 1, pp. 200–205, 2016.
- [61] R. Hurlston, “True-stress and true-strain – what is it and why does it matter?,” *Fidelis engineering associates*, 09 2023.
- [62] S. Ralph I., F. Ali, R. S. Robert, and O. F. Henry, “Metal fatigue in engineering,” 10 2000.
- [63] S. Liu, A. Wang, and J. Xie, “Effect of deformation temperature, strain rate and

- strain on the strain hardening exponent of copper/aluminum laminated composites,” *Advanced Composites Letters*, vol. 27, no. 4, 2018.
- [64] S. Benzley, E. Perry, K. Merkley, B. Clark, and G. Sjaardema, “A comparison of all hexagonal and all tetrahedral finite element meshes for elastic and elastoplastic analysis,” *Proceedings, 4th International Meshing Roundtable*, vol. 17, 01 1995.
- [65] R. Devin, “Tetrahedral vs. hexahedral mesh (mesh comparison),” 2020.
- [66] D. K. Kim, I. Ban, B. Y. Poh, and S.-C. Shin, “A useful guide of effective mesh-size decision in predicting the ultimate strength of flat- and curved plates in compression,” *Journal of Ocean Engineering and Science*, 2022.
- [67] K. H. Shivanna, S. C. Tadepalli, and N. M. Grosland, “Feature-based multi-block finite element mesh generation,” *Computer-Aided Design*, vol. 42, no. 12, pp. 1108–1116, 2010.
- [68] D. E. Keyes, L. C. McInnes, C. Woodward, W. Gropp, E. Myra, M. Pernice, J. Bell, J. Brown, A. Clo, J. Connors, E. Constantinescu, D. Estep, K. Evans, C. Farhat, A. Hakim, G. Hammond, G. Hansen, J. Hill, T. Isaac, X. Jiao, K. Jordan, D. Kaushik, E. Kaxiras, A. Koniges, K. Lee, A. Lott, Q. Lu, J. Magerlein, R. Maxwell, M. McCourt, M. Mehl, R. Pawlowski, A. P. Randles, D. Reynolds, B. Rivière, U. Rüde, T. Scheibe, J. Shadid, B. Sheehan, M. Shephard, A. Siegel, B. Smith, X. Tang, C. Wilson, and B. Wohlmuth, “Multiphysics simulations: Challenges and opportunities,” *The International Journal of High Performance Computing Applications*, vol. 27, no. 1, pp. 4–83, 2013.

- [69] A. N. Eraslan, “Von mises yield criterion and nonlinearly hardening variable thickness rotating annular disks with rigid inclusion,” *Mechanics Research Communications*, vol. 29, no. 5, pp. 339–350, 2002.
- [70] C.-K. Lin, T.-T. Chen, Y.-P. Chyou, and L.-K. Chiang, “Thermal stress analysis of a planar soft stack,” *Journal of Power Sources*, vol. 164, no. 1, pp. 238–251, 2007.
- [71] F. Shen, W. Hu, Q. Meng, and M. Zhang, “A new damage mechanics based approach to fatigue life prediction and its engineering application,” *Acta Mechanica Solida Sinica*, vol. 28, no. 5, pp. 510–520, 2015.
- [72] “Metallic materials properties development and standardization,” *Federal Aviation Administration*, 2010.
- [73] “Sae fatigue design handbook ae-22,” *SAE International*, p. 321, 09 1997.
- [74] Y. Maeda, S. Nishiwaki, K. Izui, M. Yoshimura, K. Matsui, and K. Terada, “Structural topology optimization of vibrating structures with specified eigenfrequencies and eigenmode shapes,” *International Journal for Numerical Methods in Engineering*, vol. 67, 2006.
- [75] X. Li, S. Huang, Q. Zhang, and Y. Dai, “Electromagnetic noise assessment for ev’s pm driving machines,” pp. 1552–1555, 2014.
- [76] X. Li, X. Tian, Y. Wang, R. Zhao, and W. He, “Analysis of vibration and noise of ipmsm for electric vehicles under inverter harmonic in a wide-speed range,” pp. 1–6, 2019.

- [77] X. Li, C. Liu, B. Mei, S. Wei, and N. Xia, “Vibration and noise sources analysis of ipmsm for electric vehicles in a wide-speed range,” *Proc. CSEE*, vol. 38, no. 17, pp. 5219–5227, 2018.
- [78] T. T. 4William and D. Marie Dillon, “Theory of vibration with applications,” *Prentice Hall*, vol. 5th ed, p. 273, 1998.
- [79] Goltens, “Crankshaft annealing,” *machining, service and maintainence*, 2018.
- [80] Metlab, “Nitriding,” *heat treatment*, 2012.
- [81] L. Yang, Y. Chu, and R. Mao, “Study on fatigue test for the direct drive motor of metro bogie,” pp. 825–828, 2020.